A Numerical and Analytic Investigation of Probability Distributions of the Stress Tensor in Conformal Field Theory

Bradley Lang

PhD

University of York
Mathematics

September 2022

Abstract

Repeated measurements of the smeared (averaged) stress-energy tensor of a quantum field in the vacuum state produce random values described by a probability distribution. This distribution is related non-trivially to the choice of smearing function. For unitary, positive-energy conformal field theories in 2-dimensions there are two methods available to determine the distribution. One of which uses conformal welding to determine the characteristic function while the other finds the moment generating function. The aim of the thesis is to numerically implement the conformal welding method and perform comparisons with these results to those generated by the method of moments. We employ the method of conformal welding to numerically analyse the effect of different smearing functions on the probability distribution in a 2-dimensional conformal quantum field theory. Several numerical methods were developed to ameliorate the difficulties posed by each method and improve the quality of the data generated. Both methods are compared to demonstrate their individual benefits and pitfalls when calculating probability distributions. An interesting test case is a smearing function given as the product of a Gaussian function and a Lorentzian function. This is analysed numerically by both the welding method and the method of moments. Furthermore some asymptotic results are obtained from the moments method. Importantly, the Gauss-Lorentz test function is the first known example of a positive test function in which the probability distribution does not belong to the family of shifted Gamma distributions. We also use the numerical welding method to analyse the

effect of varying parameters of a plateau test function on the associated probability distribution. This analysis gives numerical evidence that the probability distribution associated to a plateau test function averaging the stress-energy tensor depends on both the switch on parameters and the length of the plateau used.

Contents

List of Figures

Acknowledgments

I would like to thank the following people for their help during this project:
My supervisor Professor Chris Fewster, for his guidance, patience and insight.
My wife Franchesca, I could not have done this without you.
My family, thank you for supporting me during this period.

Author's declaration

I declare that the work presented in this thesis, except where otherwise stated, is based on my own research carried out at the University of York and has not been submitted previously for any degree at this or any other university. Sources are acknowledged by explicit references.

— 1 —

Introduction

The use of mathematics to provide a framework to describe reality is not new. First, human civilization used geometry to describe the position of celestial bodies. Then, with the help of calculus, it was able to predict their motion. Moreover, they were able to identify that this and other motions were governed by Newton's Laws. This was a remarkable discovery, as now physical problems could be posed in terms of ordinary differential equations. After some time, calculus was enhanced into vector calculus, which allowed us to describe physical objects known as fields. So, by the end of the 19th century, the so-called classical physics was a well-understood subject that allowed us to understand fields and objects at a mesoscopic scale in the language of ordinary and partial differential equations.

Quantum physics was born when classical physics broke down. Classical physics calculates that one finds that an ideal black body will emit an unbounded amount of energy while it is at thermal equilibrium provided that the wavelength is in the ultraviolet range. This prediction is incorrect and can be explained away by discretising light into "quanta". This discretisation and the subsequent study thereof formed quantum physics.

In physics, an observable is a measurable physical quantity. Observables are mathematically represented in classical physics by real-valued functions. When one transitions into quantum physics the states of a quantum theory

form a Hilbert space $\mathcal{H}$. These observables instead are given by self-adjoint operators on that space. In quantum field theory these observables in continuum are given by operator-valued distributions which yield operators upon being averaged by a test function.

We use smooth test functions in order to smear our observables and often denote these test functions on the real line by g. In this project we are interested in the behaviour of the stress energy tensor T and we express the smeared energy density $T(g)$ in a general d dimensional theory for $x \in \mathbb{R}^d$ as

$$T(g) = \int_{\mathbb{R}^d} T(x)g(x)d^d x. \tag{1.1}$$

In general we wish to calculate the probability distribution of the stress energy tensor acting on a vacuum state. The expectation value [40] of the stress energy density (when correctly renormalised) of a quantum field can be used to describe the gravitational effects of quantum fields. This semiclassical theory [42] has limitations when trying to describe mean value fluctuations [27] and yet remains a foundation of current day research topics [14, 25]. These calculations often amount [11] to calculation of the variance or the second moment of the probability distribution of the smeared stress-energy tensor.

Calculation of probability distributions in general is a challenging problem. It would be wonderful to perfectly understand these distributions for a d dimensional theory, or even be able to understand the effects in an $d = 4$ dimensional theory. Unfortunately at this stage we struggle even in the simplest cases and this project turns to Conformal Quantum Field theories in 1+1 dimension in an attempt to analyse existing models and further the understanding of the subject. Therefore this project we are not looking at the case of a d dimensional quantum field theory but instead study the impact of choosing a specific test function to smear against T on the probability distribution in a $1 + 1$ dimensional conformal quantum field theory (CFT). CFT in $1 + 1$ dimensions has a handful of analytic probability distributions known [2, 11, 12]. The probability distributions that could be calculated ana-

lytically were associated to a small group of infinite families of test functions.

In a $1+1$ CFT the stress energy tensor T splits up into left and right-moving components and the theory is partly characterised by a central charge that shows up in the commutation relations of these components. Familiar theories such as the free massless boson and the fermion in $1+1$ are CFTs of this type [18].

We choose the observable T due to its importance in general relativity through its entries dictating the behaviour of space time. In quantum field theory the possibility of observation from its potential to initiate large vacuum radiation pressure fluctuations [16] makes it of special interest. In [16] they discuss how radiation pressure fluctuations are "due to cross terms between vacuum and state dependent terms in a stress tensor operator product". These fluctuations, as was first analysed by Caves [6], impact the sensitivity of laser interferometer detectors of gravitational radiation.

In this project we wish to calculate the probability measure $dv_f(\lambda)$ for the smeared stress energy tensor $T(g)$ using the analytic prescriptions given in [11, 12]. We investigate the impact of using different test functions on the probability distribution.

In general one finds the relationship [12] between the operator $e^{iT(f)}$, $t \in \mathbb{R}$ and real valued f and the characteristic function of the vacuum probability distribution $dv_f(\lambda)$

$$\left\langle \Omega | e^{itT(f)} \Omega \right\rangle = \int e^{it\lambda} dv_f(\lambda). \tag{1.2}$$

The two known methods that one can use to calculate the probability distribution are called conformal welding[12, 31] and the method of moments[12, 11, 2]. These methods approach the problem quite differently and as a result they have different strengths and weaknesses. The method of welding lends itself to a more direct and general numerical implementation but generates the Fourier transform of the probability distribution which is often

problematic to invert. As well as this the method precludes much in the way of direct analytic calculation. Contrast this with the method of moments which does not offer a clear general method for numerical analysis but offers a more tractable analytic approach than the welding method.

The first analytically calculated probability distribution was given in [11]. In this they used a Gaussian test function $g(u) = \mathrm{e}^{-(u/\tau)^2}/(\tau\sqrt{\pi})$ to calculate that the vacuum probability distribution of the energy density was given by a shifted Gamma distribution

$$dv_f(\lambda) := \vartheta(\lambda+\sigma)\frac{\beta^\alpha(\lambda+\sigma)^{\alpha-1}}{\Gamma(\alpha)}\exp(-\beta(\lambda+\sigma))\mathrm{d}\lambda. \tag{1.3}$$

We denote the Heaviside function with ϑ and the Gamma function with Γ, the remaining terms are constants related to the probability distribution and found when calculating it.

The test function parameter τ and the central charge of the theory c dictate the behaviour of this distribution through their appearance in the constants $\alpha = c/24$, $\beta = \pi\tau^2$ and $\sigma = \alpha/\beta$. A shifted Gamma distribution was also found to be the probability distribution when one uses a Lorentzian test function

$$L(u) = \frac{k}{u^2+b^2} \tag{1.4}$$

to average T as seen in [2] for constants k and b. In this same work it was found that modified families of Gaussian and Lorentzian test functions also gave shifted Gamma probability distributions.

1.1 QUANTUM MECHANICS AND PROBABILITY

To glean an insight into the relationship between quantum mechanics and probability we consider for example, $\mathcal{H} = L^2(\mathbb{R})$ and the position operator X on $\mathcal{H}$ defined by

$$(X\psi)(x) = x\psi(x) \tag{1.5}$$

with $\psi \in L^2(\mathbb{R})$. Following [22] we have a spectral projection defined on any interval $I \subset \mathbb{R}$

$$(P(I)\psi)(x) = \chi_I(x)\psi(x) \tag{1.6}$$

with our indicator function χ_I of I

$$\chi_I(x) = \begin{cases} 1 & x \in I \\ 0 & x \notin I \end{cases} \tag{1.7}$$

and $P^2 = P = P^*$. The map $I \to P(I)$ extends to a projection-valued measure and to each square integrable ψ that is normalised, $I \to \langle\psi|P(I)\psi\rangle$ extends to a probability measure. So if one were interested in the probability of finding ψ in the range (a, b) the calculation would then be

$$\langle\psi|P([a,b])\psi\rangle = \int_{\mathbb{R}} \overline{\psi(x)}\chi_{[a,b]}(x)\psi(x)dx \tag{1.8}$$

which reduces to

$$\langle\psi|P([a,b])\psi\rangle = \int_a^b |\psi(x)|^2 dx. \tag{1.9}$$

To every self-adjoint operator A on bounded, complete and normed $\mathcal{H}$ there exists a unique projection valued measure P_A on the Borel σ-algebra in $\sigma(A)$, with values in projections on $\mathcal{H}$

$$\int_{\sigma(A)} \lambda dP_A(\lambda) = A. \tag{1.10}$$

$I \to P_A(I)$ and to each state $\psi \in \mathcal{H}$ that is normalised $||\psi|| = 1$, $I \to \langle\psi|P_A(I)\psi\rangle$ gives a probability measure. We can define

$$Prob(A \in I|\psi) = \langle\psi|P_A(I)\psi\rangle \tag{1.11}$$

and have the following result for some bounded and measurable function g

$$\langle\psi|g(A)\psi\rangle = \int g(\lambda)d\langle\psi|P_A(-\infty,\lambda)\psi\rangle \tag{1.12}$$

If one has a discrete spectrum of eigenvalues λ_n of A with basis $|e_n\rangle$ one can find the special case formula

$$\langle\psi|g(A)\psi\rangle = \sum_n g(\lambda_n)|\langle e_n|\psi\rangle|^2. \tag{1.13}$$

1.2 CONFORMAL FIELD THEORY

Conformal quantum field theory [38, 8, 4, 32] is defined to be a quantum field theory which obeys conformal invariance or has an invariance under transformations from the conformal group. Conformal transformations are those which preserve angles within the spacetime. The main interest for this project results in working on a $1+1$ Minkowski spacetime which means using only one spatial variable and one temporal variable on a flat spacetime. The stress-energy tensor $T^{\mu\nu}$ is assumed to be symmetric and conserved $\partial_\mu T^{\mu\nu} = 0$. These assumptions assure that the stress energy tensor is traceless and has only two independent components T^{00} and T^{01} which we can decompose into left and right moving chiral components

$$\begin{aligned} T^{00}(x^0, x^1) &= T_R(x^0 - x^1) + T_L(x^0 + x^1) \\ T^{01}(x^0, x^1) &= T_R(x^0 - x^1) - T_L(x^0 + x^1) \end{aligned} \tag{1.14}$$

and we are able then to roll these light rays into circles. The ability to map between these two representations of the line and the circle allows the use of a larger class of techniques within the theory as a whole. The numerical welding method used within this project is developed for the circle, but we are able to translate results between the two representations via the Cayley map which takes $u \in \mathbb{R}$ and maps it to the circle $\mathbb{S}$ via

$$u \mapsto C(u) = \frac{1+iu}{1-iu} \in \mathbb{S}\backslash\{-1\} \tag{1.15}$$

defining $C(\infty) = -1$ to create a bijection between the line and the circle. Using this map we are able to create an equivalence between the stress energy tensor on the line and circle and this allows for the translation of information between the two pictures.

This scale invariance property means [36, 7] that a conformal transformation is a local rescaling of the metric. Specifically, conformal field theories obey the same physics at every length scale. This often allows for simplification in calculation and CFTs can allow for exact calculations [15,

20] within quantum field theories which is incredibly valuable.

CFT is also used throughout String theory[35, 39] due to the description of the worldsheet of a string's excitations. Other uses of CFTs include statistical physics [5] and condensed matter [1].

1.2.1 Quantum energy inequalities

In classical relativity, if one focuses solely on Einstein's equations and doesn't impose restrictions on the matter then they can find surprising phenomena including traversable wormholes and superluminal "warp drive" spacetimes[29]. These exotic solutions often have never been observed and require an explanation. Commonly this explanation is that spacetimes require presence of matter fields with negative energy densities. Contextually, an important role is held by energy conditions which pose pointwise restrictions onto the stress-energy tensor. These energy conditions provide a key role in ensuring the stability of gravitational collapse [23] via singularity theorems.

Quantum field theory violates these energy conditions [9] but can obey weaker energy conditions [10]. In quantum field theories these energy conditions or quantum energy inequalities are state independent lower bounds on a smeared stress-energy tensor [13].

In [13] it is found that a sharp quantum energy inequality bound can be derived in a 2-dimensional unitary conformal quantum field theory with positive stress-energy tensor and Hamiltonian. The main result is given as a theorem which we state for reference later.

Theorem 1. *Consider a conformal field theory with a single component T of stress energy. For any nonnegative $G \in \mathcal{S}(\mathbb{R})$, the quantum energy inequality*

$$\int G(v) \langle T(v) \rangle_\psi \, dv \geq -\frac{c}{12\pi} \int \left(\frac{d}{dv} \sqrt{G(v)} \right)^2 dv \tag{1.16}$$

holds for all $\psi \in \mathcal{D}$.

Elucidating a few terms within that theorem, the differential of the square root vanishes for all values of $G(v) = 0$ to avoid singularities. The $\mathcal{S}(\mathbb{R})$ denotes a Schwarz class which is the class of functions that, along with their derivatives, vanish more rapidly than any inverse power at infinity. Lastly $\mathcal{D} \subset \mathcal{H}$ denotes a dense domain of the Hilbert space.

— 2 —

Conformal welding & probability

Within this chapter we shall discuss the theoretical background to the welding project. We begin with discussion of the Virasoro algebra and then discuss the introductory step to using the welding method for calculating probabilities. Following this, we end up with an elucidation of the welding problem and an example calculation using this method to generate the probability distribution. The Lüscher-Mack theorem [17, 30] asserts (provided the Wightman axioms are obeyed by the theory [41]) that if such a theory has a conserved, symmetric stress-energy tensor field $T^{\mu\nu}$ which obeys

$$\int T^{\mu 0}(x^0, x^1)dx^1 = P^\mu, \tag{2.1}$$

where x^0, x^1 are the spacetime coordinates in a $1+1$ dimensional theory and P^μ are the energy-momentum operators which generate spacetime translations then the stress-energy tensor is traceless and the independent components T^{00} and T^{01} can be expressed using left and right-moving chiral components.

2.1 VIRASORO ALGEBRA

The Virasoro algebra is a complex Lie algebra used in conformal field theory and string theory [35]. It is defined by relation

$$[L_n, L_m] = (n-m)\, L_{n+m} + \frac{\kappa}{12} n(n^2-1)\delta_{n,-m} \tag{2.2}$$

where the L_n are the generators of the algebra, $\kappa = cI$ where c is called the central charge of the algebra with $n, m \in \mathbb{Z}$.

From this algebra we define the stress tensor on the unit circle $\mathbb{S}$, identifying the points $z = e^{i\theta} \in \mathbb{C}$ and $\theta \in \mathbb{R}$. The stress tensor is an operator valued distribution on $\mathcal{H}$ defined in the sense of distributions by the series

$$T(z) = -\frac{1}{2\pi} \sum_{n=-\infty}^{\infty} L_n z^{-n-2}. \tag{2.3}$$

Decomposing our spacetime coordinates into left and right moving light rays as in (1.14) and denoting the right moving light ray coordinates by u (this choice was arbitrary). The energy density in the CFT of the right moving light ray shall be denoted by $T(u)$ and satisfies a relation as in [13]

$$\begin{gathered}[T(u_1), T(u_2)] = \\ i\left(-T'(u_2)\,\delta(u_1-u_2) + 2T(u_2)\,\delta'(u_1-u_2) - \frac{c}{24\pi}\delta'''(u_1-u_2)\,I\right)\end{gathered} \tag{2.4}$$

with c defined as before.

So far we have discussed the energy density T on the real line (which in this case is the right moving light ray u) and the circle. It is simple and convenient to relate the stress energy tensor on the line to the circle via the relation

$$T_{line}(u) \equiv \left(\frac{dC(u)}{du}\right)^2 T_{circle}(C(u)). \tag{2.5}$$

Here we have used the Cayley map as defined by (1.15) demonstrating the explicit relationship between the energy densities in the two pictures.

2.2 THE FLOW EQUATION

There are several steps in the process of calculating the probability distribution which are detailed in [12]. The first of which involves a flow equation which we are required to solve in order to progress to the next step of the welding method.

This flow solution needs to be inverted to be used in the next steps of the welding problem so instead we will also invert the flow equation itself

and produce a flow equation for the inverse of the flow solution. This inverse flow solution is used in the numerical implementation of this method and discussed for clarity.

We have the 1-parameter flow equation for diffeomorphisms generated by the test function $g \in C^\infty(\mathbb{R})$

$$\frac{\partial \rho_t(z)}{\partial t} = g(\rho_t(z)), \tag{2.6}$$

with $\rho_t \in \text{Diff}(\mathbb{S})$, $\rho_0 = id$. We wish to generate a formula for the inverse flow. In order to do this we integrate both sides with respect to the parameter t

$$\int_0^t \frac{1}{g(\rho_s(z))} \frac{\partial \rho_s(z)}{\partial s} ds = t. \tag{2.7}$$

To proceed, we perform a change of variables $y = \rho_s(z)$ transforming our limits and integrand

$$\int_{\rho_0(z)}^{\rho_t(z)} \frac{1}{g(y)} dy = t. \tag{2.8}$$

Using the fact that $\rho_0(z) = z$ we can simplify the lower limit. At this stage however, we aren't interested in the flow $\rho_t(z)$. We instead wish to find the inverse flow $\rho_t^{-1}(z)$ and will do so by inverting the coordinates

$$\int_{\rho_t^{-1}(z)}^{z} \frac{1}{g(y)} dy = t. \tag{2.9}$$

We define

$$G(x) = \int_0^x \frac{1}{g(y)} dy \tag{2.10}$$

and recognise that (2.9) can be written as

$$G(z) - G\left(\rho_t^{-1}(z)\right) = t. \tag{2.11}$$

Differentiating with respect to t gives

$$-\frac{\partial \rho_t^{-1}(z)}{\partial t} \frac{1}{g\left(\rho_t^{-1}(z)\right)} = 1, \tag{2.12}$$

rearranged gives the modified flow equation for the inverse flow as seen in [19]

$$\frac{\partial \rho_t^{-1}(z)}{\partial t} = -g\left(\rho_t^{-1}(z)\right). \tag{2.13}$$

Mapping this result to the unit circle using $\rho_t^{-1}\left(e^{i\theta}\right) = e^{i\chi_t^{-1}(\theta)}$ gives the final result of

$$\frac{\partial \chi_t^{-1}(\theta)}{\partial t} = ie^{-i\chi_t^{-1}(\theta)} f\left(e^{i\chi_t^{-1}(\theta)}\right). \tag{2.14}$$

The test function in this transformed equation will be mapped to the circle using the Cayley transform (1.15) once more

$$f(z) = C'\left(C^{-1}(z)\right) g\left(C^{-1}(z)\right). \tag{2.15}$$

2.3 THE WELDING METHOD

After mapping the test function g to the circle using the Cayley transform, a boundary is created between the mapped upper and lower half planes. This boundary (called a Jordan curve) is described by two univalent functions $w^{\pm} : \mathbb{D}^{\pm} \to \Delta^{\pm}$ from the interior/exterior of the unit disk (which we denote by $\mathbb{D}^{\pm}$) to the inside/outside of this Jordan curve C separating the domains which are denoted by $\Delta^{\pm}$. The welding condition can be expressed as

$$w^{+}(z) = \left(w^{-} \circ \rho\right)(z) \tag{2.16}$$

for boundary values on the circle $z \in \mathbb{S}$ [26]. There are several methods to calculate these functions [12, 21, 26], including solving the Beltrami equation $\partial_{\bar{z}} f(z) = \mu(z)\partial_z f(z)$ by defining

$$\mu(z) = \begin{cases} \partial_{\bar{z}}\rho(z)/\partial_z \rho(z) & z \in \mathbb{D}^{+} \\ 0 & z \notin \mathbb{D}^{+}. \end{cases}$$

Despite being a potential method to solve the welding problem, this method was not used due to the alternative providing a simpler numerical implementation.

An integral operator K on $L^2(0,2\pi) = L^2(\mathbb{S})$ is defined in the same way as in [12, 26]

$$KG(\theta) = \frac{i}{4\pi}\int_0^{2\pi}\left(\cot\left(\frac{\theta-\theta'}{2}\right) - \frac{\partial\chi^{-1}}{\partial\theta}\cot\left(\frac{\chi^{-1}(\theta)-\chi^{-1}(\theta')}{2}\right)\right)G(\theta')d\theta'. \tag{2.17}$$

The χ^{-1} is calculated by solving (2.14) and $G \in L^2(\mathbb{S})$ is an arbitrary function to be operated on by K. It is possible to show

$$(I+K)\,w^-(e^{i\theta}) = e^{i\theta}, \tag{2.18}$$

giving an explicit method to calculate the function w^-. This is necessary because the calculation of the characteristic function associated to the probability distribution of the smeared stress-energy density is directly found from its Schwarzian derivative and the test function f.

2.4 THE SCHWARZIAN DERIVATIVE AND CALCULATION OF THE PROBABILITY DISTRIBUTION

The Schwarzian derivative is used in many areas of mathematics. It is used in second order ordinary differential equations, geometry and most importantly to us conformal mapping [33, 24]. It is defined as follows

$$Sf(z) = \{f,z\} = \frac{f'''(z)}{f'(z)} - \frac{3}{2}\left(\frac{f''(z)}{f'(z)}\right)^2 \tag{2.19}$$

and has the remarkable property of being invariant under Möbius transforms. Specifically, if

$$g(z) = \frac{af(x)+b}{cf(x)+d} \tag{2.20}$$

for the constants a,b,c,d either real or complex such that $ad-bc \neq 0$ then $Sf = Sg$ [34].

We also have under composition a formula which we can use to change variables [34]

$$S(f\circ g) = S(f)\circ g + S(g). \tag{2.21}$$

Having established the necessary background, one is now able to determine the probability distribution for a specific test function on either the real line or the circle in a (1+1) CFT. The equation for the Fourier transform of the probability measure $dv_f(\lambda)$ is given by[12]

$$\int_{\mathbb{R}} e^{it\lambda} dv_f(\lambda) = \exp\left(-\frac{ic}{24\pi}\int_0^t \int_S f(z) Sw^-(t', z) dz dt'\right) \tag{2.22}$$

with t the same parameter used in (2.14). The characteristic function [3] of a probability measure μ on the line is defined for $t \in \mathbb{R}$ by

$$\varphi(t) = \int_{\mathbb{R}} e^{itx} \mu(dx). \tag{2.23}$$

The characteristic function is called the Fourier transform in nonprobabilistic contexts and is exactly what we are trying to calculate using (2.22). Due to this the terms Fourier transform of the probability and characteristic function will be used interchangeably.

2.5 AN ANALYTIC EXAMPLE

To test the accuracy of the numerical implementation it is useful to have some exact results to compare against. One explicit derivation of a probability distribution is given in [12] which we summarise here to give a demonstration of the welding method.

Using the infinite family of test functions f_n on $\mathbb{S}$ given by

$$f_n(z) = \frac{1}{2n}\left(z^{-n+1} - z^{n+1}\right) \tag{2.24}$$

with $n \in \mathbb{N}$. The flow equation (2.6) is solved with $\rho_t(z)$ given by

$$\rho_t(z) = e^{\frac{i\pi k}{n}} \left((-1)^k \frac{z^n \cosh\left(\frac{t}{2}\right) + \sinh\left(\frac{t}{2}\right)}{z^n \sinh\left(\frac{t}{2}\right) + \cosh\left(\frac{t}{2}\right)}\right)^{\frac{1}{n}} \tag{2.25}$$

with $k = 0, 1.., 2n-1$.

To solve the welding problem we find that the univalent holomorphic functions $w_n^+ : \mathbb{D}^+ \to \Delta^+$ and $w_n^- : \mathbb{D}^- \to \Delta^-$ are given by

$$w_n^+(z) = z\left(\cosh\left(\frac{t}{2}\right)\right)^{-\frac{2}{n}}\left[1 + z^n \tanh\left(\frac{t}{2}\right)\right]^{-\frac{1}{n}} \tag{2.26}$$

and

$$w_n^-(z) = z\left[1 - z^{-n}\tanh\left(\frac{t}{2}\right)\right]^{\frac{1}{n}} \tag{2.27}$$

for $z \in \mathbb{D}^+$ and $z \in \mathbb{D}^-$ respectively. These functions w^+ and w^- when calculated for $z = e^{i\theta}$ match and form the Jordan curve C [12] which is the limiting dividing region between w^+ and w^-. One can then directly calculate the Schwarzian derivative to be

$$Sw_n^-(z,t) = \frac{n^2-1}{2z^2}\left(-1 + \frac{1}{(1 - z^{-n}\tanh\frac{t}{2})^2}\right). \tag{2.28}$$

For $t \geq 0$ this has poles at $z = 0, e^{2i\pi k/n}(\tanh\frac{t}{2})^{1/n}$ for $k = 0, 1.., n-1$ inside the unit disk and likewise for $t \leq 0$. It is at this stage that the calculation supposes that $t \geq 0$ and makes use of the residue theorem to calculate

$$\frac{1}{2\pi i}\int_{\mathbb{S}} f_n(z) Sw_n^-(z,t)dz = -\frac{n^2-1}{2n}\tanh\frac{t}{2}. \tag{2.29}$$

This is then substituted into (2.22) demonstrating that the Fourier transform of the probability distribution dv_n for $T(f_n)$ in the vacuum state is given by

$$\int_{\mathbb{R}} e^{it\lambda} dv_n(\lambda) = \left(\operatorname{sech}\left(\frac{t}{2}\right)\right)^p, \tag{2.30}$$

for $n > 1$ and

$$p = \frac{c}{12}\left(n - \frac{1}{n}\right). \tag{2.31}$$

This Fourier transform can be inverted analytically and gives the probability distribution

$$dv_n(\lambda) = \frac{2^{p-1}}{\pi\Gamma(p)}\left|\Gamma\left(\frac{p}{2} - i\lambda\right)\right|^2 d\lambda. \tag{2.32}$$

We have investigated the method of conformal welding as a method to calculate the probability distribution associated to the averaged stress-energy tensor. We have given an example of using this method to analytically calculate the probability distribution and outlined the key ideas in order to be able to implement this numerically.

— 3 —

Moments & probability

Similar to the previous chapter we aim to provide the necessary mathematical basis to understand how to use the moments method to procure the probability distribution of $T(g)$. We look at the benefits and drawbacks of this method and provide a worked example for clarity.

Beginning with some real-valued test function g we have $\Theta(g)$ (denoting the stress energy density on the line), a self-adjoint operator with an associated projection valued measure which we denote with $P_g(d\lambda)$ existing on the real line.

In the following we require that we are working in a general unitary and positive energy CFT in $1+1$ dimensional Minkowski space. It has been shown that one use this method to determine the probability distribution in the vacuum, thermal and highest weight states [12]. The vacuum probability distribution of our smeared stress energy density $\Theta(g)$ is given by the measure

$$dv_g(\lambda) = \langle \Omega | P_g(d\lambda)\Omega \rangle \tag{3.1}$$

and can be generalised to any state by simply replacing Ω with the state one is interested in calculating. We are also able to calculate the n'th moment m_n of v_g and it is given by the integral

$$m_n = \int_{-\infty}^{\infty} \lambda^n dv_g(\lambda). \tag{3.2}$$

One is then able to use functional calculus to use our formula (3.1) in the calculation of the moment m_n and we can calculate

$$m_n = \int_{-\infty}^{\infty} \lambda^n \langle \Omega | P_g(d\lambda) \Omega \rangle = \langle \Omega | \Theta(g)^n \Omega \rangle. \tag{3.3}$$

It was shown in [11] how to connect the probability distribution to its moments using the stress-energy density on the line. The moment generating function

$$M[\mu g] = \sum_{n=0}^{\infty} \frac{\mu^n}{n!} \langle \Omega | \Theta(g)^n \Omega \rangle = \sum_{n=0}^{\infty} \frac{\mu^n}{n!} \mathcal{G}_n[g], \tag{3.4}$$

defined by the weighted sum of moments, (we relabel our moments from m_n to $\mathcal{G}_n[g]$ to match with the related literature [11, 13]) is related to the connected moment generating function W

$$M[\mu g] = e^{W[\mu g]}. \tag{3.5}$$

Calculation of the connected moment generating function is done by integrating the second moment $\mathcal{G}_2$ twice

$$W[\mu g] = \int_0^{\mu} d\lambda (\mu - \lambda) \langle \Omega | \Theta(g_\lambda)^2 \Omega \rangle. \tag{3.6}$$

We require that g_λ must solve the flow equation

$$\frac{dg_\lambda}{d\lambda} = g_\lambda * g_\lambda, \quad g_0 = g. \tag{3.7}$$

The $*$ operation is defined by the nonlinear integro-differential equation

$$(g * g)(u) = \int_{-\infty}^{\infty} \frac{g(w)g'(u) - g'(w)g(u)}{2\pi(w-u)} dw. \tag{3.8}$$

The only known closed form solutions of (3.7) require that the initial condition g_0 be a member of a small set of infinite families [11, 2] based on either Gaussian or Lorenztian test functions or modifications thereof.

The zeroth moment obeys $\mathcal{G}_0[g] = 1$ and the first moment obeys $\mathcal{G}_1[g] = 0$ for any function g. For higher moments we have non-trivial results. Most

importantly in these methods, the second moment in (3.6) is related to the moment generating function which can be related to the probability distribution of $\Theta(g)$ acting on the vacuum state.

In the particular case of the second moment, one can show [11] that $\mathcal{G}_2(g)$ is given by

$$\mathcal{G}_2(g) = \frac{c}{8\pi^2}\int_{\mathbb{R}^2}\frac{g(u)g(v)}{(v-u-i0)^4}dudv \tag{3.9}$$

which can be represented in Fourier space, often simplifying calculations.

To transform (3.9) one makes use of the identity

$$\frac{1}{(u-i\epsilon)^4} = \frac{1}{6}\int_0^\infty \omega^3 e^{-i\omega(u-i\epsilon)}d\omega \tag{3.10}$$

which itself is proved by recursive integration by parts. The factor of ϵ is required to ensure that contributions at ∞ vanish but is often represented simply by $i0$. Substituting a modified (3.10) into (3.9) we arrive at

$$\mathcal{G}_2(g) = \frac{c}{8\pi^2}\frac{1}{6}\int_{\mathbb{R}^2}\int_0^\infty g(u)g(v)\omega^3 e^{-i\omega(v-u-i\epsilon)}dudvd\omega \tag{3.11}$$

and then separate the exponential and integral terms

$$\mathcal{G}_2(g) = \frac{c}{48\pi^2}\int_0^\infty \omega^3 e^{-\epsilon\omega}\int_{\mathbb{R}} g(u)e^{i\omega u}du\int_{\mathbb{R}} g(v)e^{-i\omega v}dvd\omega. \tag{3.12}$$

In this form, one can safely take the limit $\epsilon \to 0^+$ and define the Fourier transform of the smearing function g with convention

$$\hat{g}(\omega) = \int_{-\infty}^\infty g(s)e^{-i\omega s}ds \tag{3.13}$$

and this allows substitution of the Fourier transform and its complex conjugate

$$\mathcal{G}_2(g) = \frac{c}{48\pi^2}\int_0^\infty \omega^3\overline{\hat{g}(\omega)}\hat{g}(\omega)d\omega. \tag{3.14}$$

This gives the second moment written in terms of the Fourier transform of the test function and is often represented by

$$\mathcal{G}_2(g) = \frac{c}{48\pi^2}\int_0^\infty \omega^3|\hat{g}(\omega)|^2d\omega. \tag{3.15}$$

Once the moment generating function corresponding to a specific test function has been found one can equate it [2] to the two-sided Laplace transform of the probability distribution

$$M[\mu g] = \int_{-\infty}^{\infty} P(t) e^{\mu t} dt. \tag{3.16}$$

This means that upon calculation of the moment generating function one is able to take an inverse Laplace transform to find the probability distribution corresponding to a particular test function smearing a particular observable, in this case the stress energy density.

Although unlikely, the Laplace inversion can be done via inspection. One example would be for the shifted Gamma distribution (1.3) which incurs a moment generating function

$$M(\mu) = \left(1 - \frac{\mu}{\beta}\right)^{-\alpha} e^{-\mu\sigma} \tag{3.17}$$

which has associated to it the connected moment generating function

$$W(\mu) = \alpha \log\left(\frac{\beta}{\beta - \mu}\right) - \mu\sigma. \tag{3.18}$$

The only way that the moment generating function and connected moment generating function can exist in this form is if the second moment is given by

$$\mathcal{G}_2[g_\lambda] = \frac{\alpha}{(\beta - \lambda)^2} \tag{3.19}$$

and the quantum inequality bound σ, also calculated from (1.16), is given by the ratio of constants α and β

$$\sigma = \frac{\alpha}{\beta}. \tag{3.20}$$

To elucidate this method we will demonstrate its use with a normalised Gaussian test function

$$f(u) = \frac{e^{-u^2}}{\sqrt{\pi}} \tag{3.21}$$

and recall that we require a one parameter family of functions f_λ to solve the flow equation

$$\frac{df_\lambda}{d\lambda} = f_\lambda \star f_\lambda, \quad f_0 = f. \tag{3.22}$$

We calculate the integrand of the flow equation

$$\frac{f'(u)f(w) - f'(w)f(u)}{2\pi(w-u)} = \frac{e^{-u^2-w^2}}{\pi^2} \tag{3.23}$$

and then integrate over the variable w on the real line

$$(f \star f)(u) = \int_{\mathbb{R}} \frac{e^{-u^2-w^2}}{\pi^2} dw = \frac{f(u)}{\pi}. \tag{3.24}$$

To proceed to solve the flow equation we make the ansatz

$$f_\lambda(u) = B(\lambda)f(u), \tag{3.25}$$

which reduces our flow equation to

$$\frac{dB(\lambda)}{d\lambda} = \frac{B(\lambda)^2}{\pi}, \quad B(0) = 1. \tag{3.26}$$

Solving this equation we find our λ dependent term is given by

$$B(\lambda) = \frac{\pi}{\pi - \lambda} \tag{3.27}$$

and we can now calculate the second moment $\mathcal{G}_2$ without needing to consider the λ dependence within the integral over ω

$$\mathcal{G}_2[f_\lambda] = \frac{cB(\lambda)^2}{48\pi^2} \int_{\mathbb{R}^+} \omega^3 |\tilde{f}(\omega)|^2 d\omega = \frac{c}{24\pi^2} \frac{\pi^2}{(\pi-\lambda)^2}. \tag{3.28}$$

Direct comparison between this and the second moment for the shifted Gamma distribution in the general sense with parameters α, β gives

$$\frac{\alpha}{(\beta-\lambda)^2} = \frac{c}{24} \frac{1}{(\pi-\lambda)^2}. \tag{3.29}$$

Clearly this has generated an equation of the form (3.19) which means that the probability distribution is given by a shifted Gamma distribution (1.3) with parameters

$$\begin{aligned} \alpha &= \frac{c}{24} \\ \beta &= \pi. \end{aligned} \tag{3.30}$$

This example demonstrates the potential power of the method of moments but this is very dependent on the test function used.

One should note that despite the reasonably simple theoretical connections between test function and associated probability distribution for the stress energy density, numerically this method is fraught with areas of difficulty.

Solving the integro-differential equation (3.7) numerically is challenging. In comparison, analytic methods often begin with a simple ansatz of separation of variables. To generalise the solution of (3.7) to a numerical method would require careful handling of (3.8) due to the potential of a singularity emerging from the denominator. This is not the only problem in constructing a general numerical method. The λ dependence introduced by (3.7) brings further potential challenge as well.

Another issue is in the final step of calculation as numerical stability in the process of inverting Laplace transforms is challenging and requires very well behaved input data. This will be discussed more in forthcoming sections but one should not be fooled by the comparative simplicity of the moments method compared to the welding method. They both have merit in specific scenarios.

Analytically the moments method is more tractable. The main challenge of the method is finding a flow solution g_λ which obeys (3.7). One can start with the initial condition test function g_0 and then find themselves unable to solve (3.7) for a general g_λ. This key difficulty is the reason that a general numerical method was not developed for this approach.

— 4 —

Implementation of the Welding method: Part 1

[1] The first part of this two part chapter will give the main ideas of numerical implementation of the welding method as well as highlight the vital improvements made to the method numerically. We discuss the need for these improvements and how previous methods were unsuitably accurate for our use. We also develop our own method of accurate high-precision calculation of the Schwarzian derivative which is a key bottleneck for accuracy within the numerical implementation.

As seen, the welding method appears to offer a way of calculating the probability density of the averaged energy density in a vacuum state. This probability density has been shown to be affected by the choice of the smearing function used to average the energy density. Numerical implementation of this method has several key steps that require careful data handling due to the unstable nature of the problem at each step. One begins by numerically solving the flow equation either on the line as in (2.6) or on the circle (2.14). This already can be problematic because of the differential solving routines used to generate the 1-parameter family of diffeomorphisms from the flow equations.

Attempts to solve (2.14) using the in-built partial differential equation solvers of Mathematica and Maple had issues with dealing with the large

[1] All codes created for this project are available upon request

derivatives incurred after the parameter t had evolved to a certain point. The value of t at which the solver will encounter problems depends entirely on the test function chosen. The underlying issue common to all tests performed was the occurrence of very large values being produced in the derivative terms after t had sufficiently evolved.

Throughout initial implementation to verify the methods used, the code was compared to the derivation of the probability density (2.32) given in [12] which details every relevant step of the calculation that one should wish to compare their numerical data to. This comparison made it evident that it would be beneficial to use the method of lines [37] to convert the partial differential flow equation to a finite set of ordinary differential equations.

The method of lines in this implementation solves the flow solution ordinary differential equations for successive values of the spatial parameter. The reason for choosing the spatial parameter over the parameter t is due to the fact that in each ODE the initial condition of the flow is given by the identity transforming the angular input into itself. Fig. 4.1 demonstrates the high level of agreement between the method of lines and the original method of flow solution. The method of lines solves the flow equation well but with the aim to push the value of t as high as possible while maintaining smooth and accurate data, further tests were performed.

For example, if one increases the value of t to 20, a value that would have caused large issues for the partial differential equation solver, and compare the flow solution to the analytic solution detailed in [12] one can see from Fig. 4.2 that the method of lines clearly has no issues in solving the flow equation despite the divergent spatial differential values in the flow solution as $t \to \infty$.

This crucial requirement, long term stability as we evolve t in the flow equation solver, meant that the method of lines seemed like the only reasonable choice to make. It goes without saying that if instead of large spatial derivatives, the solver encountered large t derivatives then it is reasonable

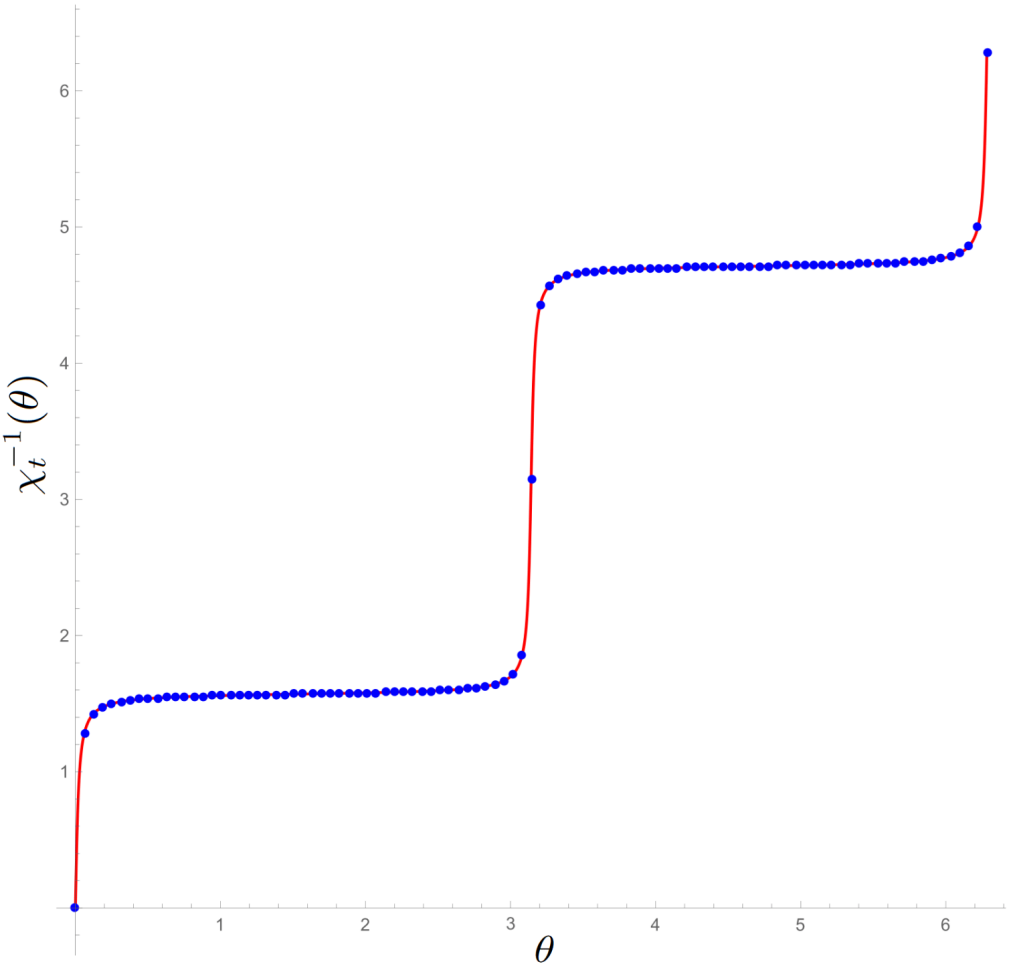

Figure 4.1: Plot comparing the flow solution methods of solving (2.14) for the test function (2.24). The inbuilt Mathematica PDE solver NDsolve (red) is compared to the method of lines which also uses NDsolve for the required ODEs (blue points).

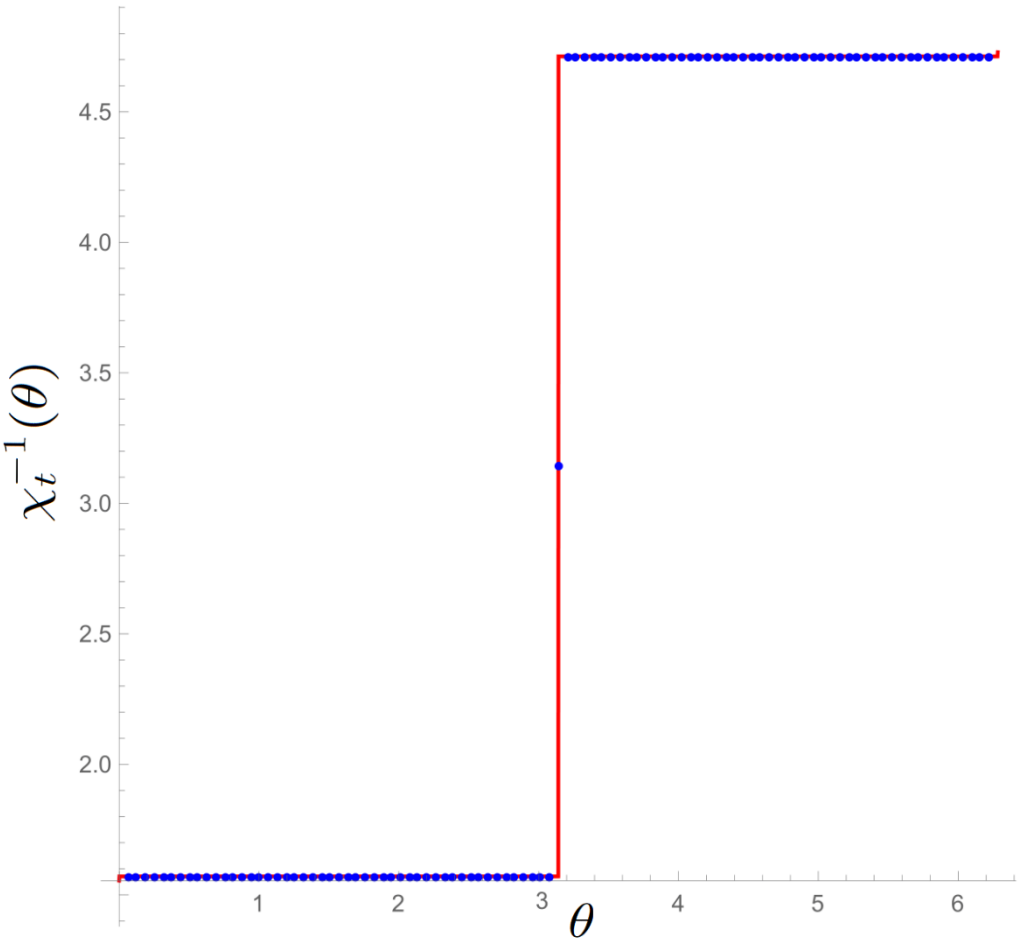

Figure 4.2: Plot comparing the analytic argument of the flow solution (2.25) (red) for the test function (2.24) against the method of lines in Mathematica using NDsolve to calculate the solution to the vector of ODEs at $t = 20$.

to assume that the flow solver could run into difficulty. Testing the method of lines against the inbuilt partial differential solvers of Mathematica and Maple to solve the flow equation, the method of lines performed better for not only (2.24) but also for a Gaussian test function. The method of lines also had the benefit that it solved the problem faster than the inbuilt partial differential solvers.

After the value $\chi^{-1}(\theta)$ has been calculated from (2.14) we are ready to try to solve the welding problem (2.18) which requires use of the integral operator K defined by (2.17). Within the integrand of K we notice the dependence on the inverse flow on the circle $\chi^{-1}(\theta)$ as well as the spatial derivative $\left(\chi^{-1}\right)'(\theta)$. We are able to calculate this derivative either using analytic formula or finite difference methods. Instead of using the integral definition of K we use a similar method as in [31] wherein the operator integrand is discretised to form a matrix with each entry corresponding to a different pair of angular points.

As is evident from the formula (2.17) one must take care with the point of coincidence of the cotangent terms. The diagonal entries of the discretised K integrand matrix K_{ab} correspond to the points of angular coincidence. These entries are calculated seperately to the bulk terms where the integrand formula can be used as written in (2.17). To calculate the coincidence formula we take the integrand and perturb one of the angular coordinates from the other and then take the coincidence limit when the formula is simplified. The near coincidence integrand K_I is given by

$$K_I(\theta+\epsilon,\theta) = \cot\left(\frac{\theta+\epsilon-\theta}{2}\right) - (\chi_t^{-1})'(\theta)\cot\left(\frac{\chi^{-1}(\theta+\epsilon)-\chi^{-1}(\theta)}{2}\right). \quad (4.1)$$

We expand the cotangent terms using the series expansion

$$\cot(\epsilon) = \frac{1}{\epsilon} - \frac{\epsilon}{3} + \mathcal{O}(\epsilon^3), \quad (4.2)$$

which is trivially substituted in the first term. The second term requires a

further Taylor expansion of the function χ_t^{-1} to give

$$K_I(\theta+\epsilon,\theta) = \frac{2}{\epsilon} - (\chi_t^{-1})'(\theta)\left(\frac{2}{(\chi_t^{-1})'(\theta)\epsilon} - \frac{(\chi_t^{-1})''(\theta)}{(\chi_t^{-1})'(\theta)^2}\right) + \mathcal{O}(\epsilon). \tag{4.3}$$

We have a clear cancellation of singularities at coincidence due to the cancellation of the derivative of the angular flow solution in the numerator and the denominator of the subtracted term. This leaves us with an exact value at coincidence which is

$$\lim_{\epsilon\to 0} K_I(\theta+\epsilon,\theta) = \frac{(\chi_t^{-1})''(\theta)}{(\chi_t^{-1})'(\theta)}. \tag{4.4}$$

For the remainder of the K matrix, one is able to populate the entries by using the formula as described by (2.17). This step in the code presented a large issue with the implementation. The density increase of angular mesh points N resulted in an $\mathcal{O}(N^2)$ increase in computation time from the dimension of the matrix. Balancing reasonable calculation times with accurate data output was a constant challenge with early calculations of the welding solution looking erroneous and jagged. This is best demonstrated when calculating for the welding solution using the test function given by (2.24), choosing the integer $n = 8$, shown in Fig. 4.3. This jaggedness was due to not being able to calculate a large value of angular points in a reasonable time frame. Due to the $\mathcal{O}(N^2)$ increase in data points of K_{ab}, memory is a necessary consideration. If one has enough free memory to increase the total number of angular points N then this will improve the data generated for all implemented versions of K_{ab}.

After calculation of the K matrix we are ready to solve the welding problem using (2.18). Numerically this was done using inbuilt linear algebra libraries to solve the vector equation for the unknown $w_b^-(\theta,t)$, the subscript b denoting the discretised value of w^-. After solving for w_b^- for the test function given by (2.24), one is then able to compare this to the analytic result given in [12]. This comparison can be seen in Fig. 4.4 which clearly demonstrates excellent agreement from the numerical data to the analytic function. One should also note that if we are generating a good agreement

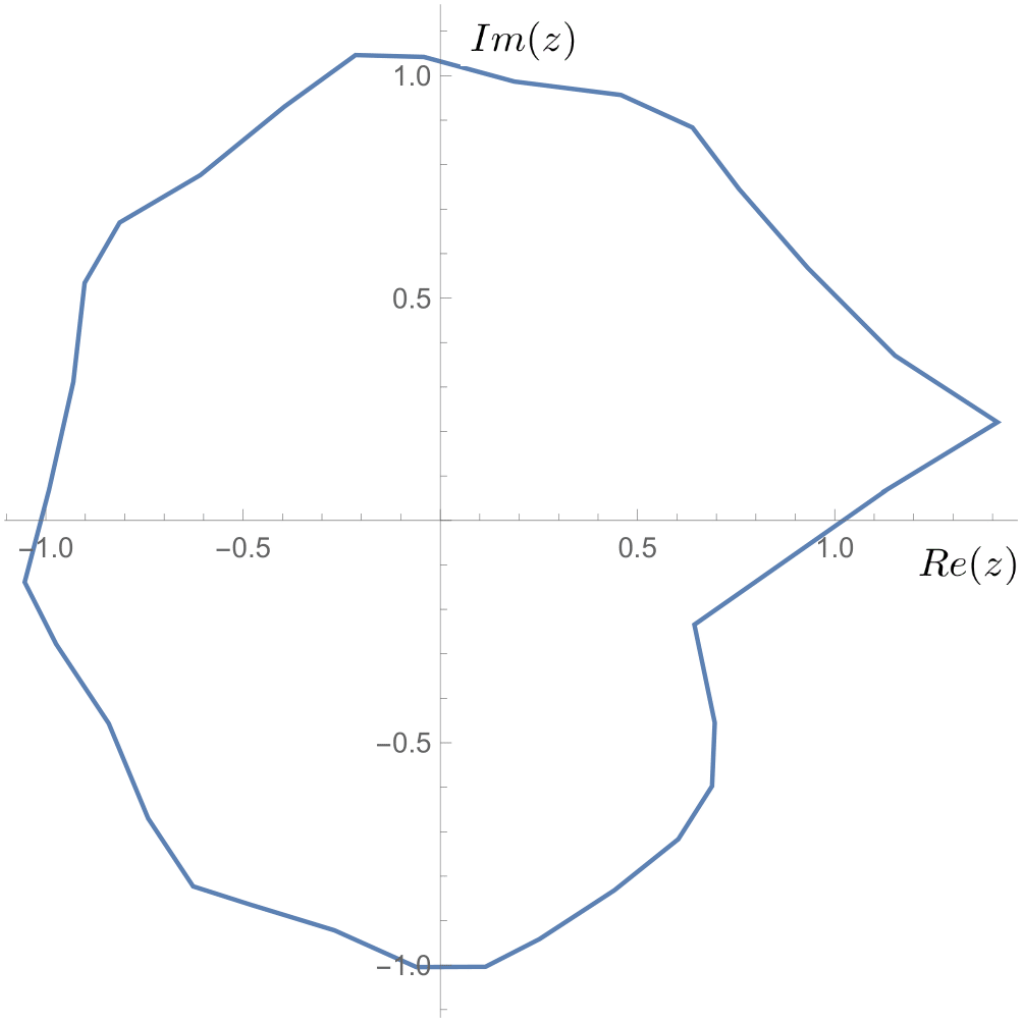

Figure 4.3: Interpolated complex plot of the numerically calculated (2.27) solving the welding problem for test function (2.24), choosing the integer valued constant, n, to be 8 in this case. This plot demonstrates the initial method used wherin the values at each stage of calculation were calculated via the relevant formulae instead of allocating figures into static arrays to expedite the calculation time.

between the Jordan curve at the highest possible parameter value t and the numerical output at this same value, then it is highly likely that all of the Jordan curves at each step in t below this will match well. The reason for this is at $t = 0$ the flow solution returns the identity and following this through the welding process, the Jordan curve at $t = 0$ returns a circle. As we increase t, the circle gradually deforms and evolves to create the Jordan curve specific to the test function used.

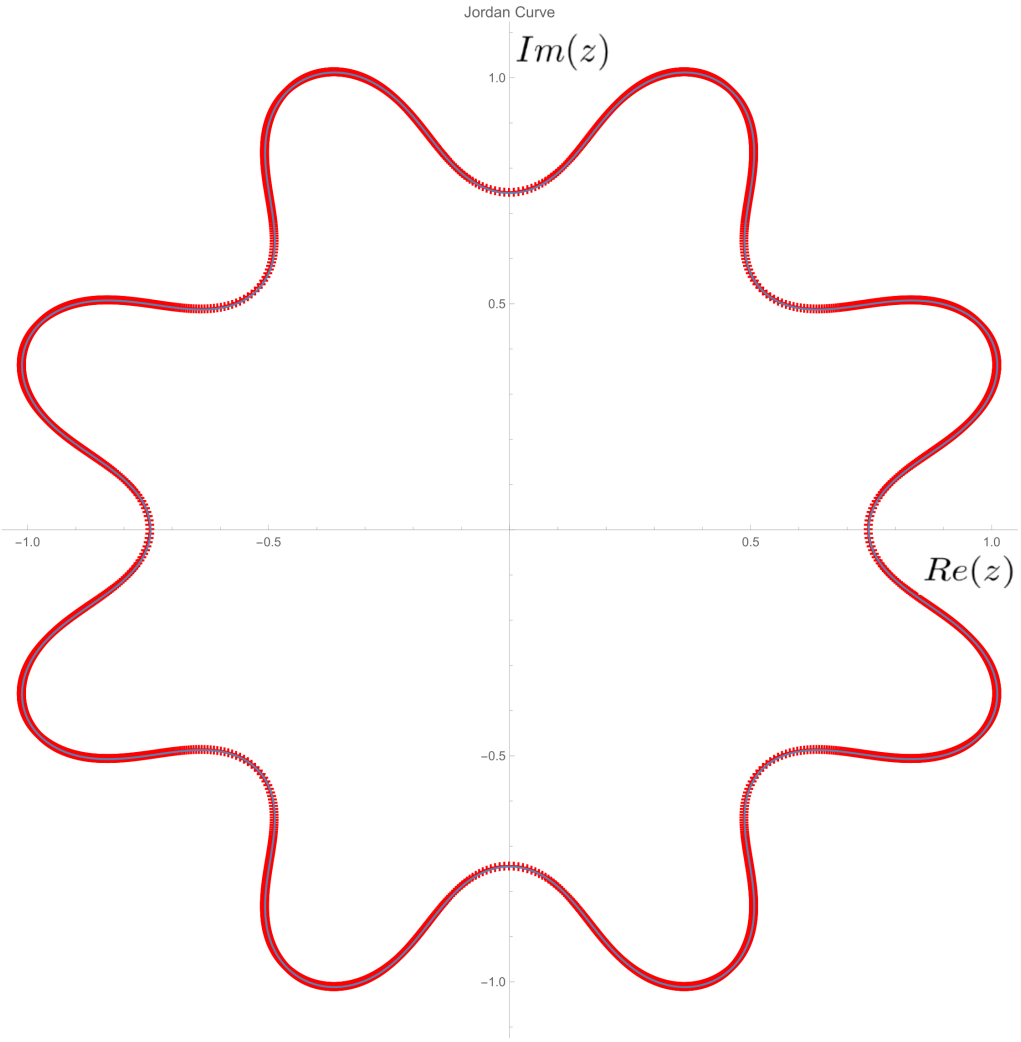

Figure 4.4: Jordan curve resulting from the test function (2.24) compared to numerically calculated data from the welding method code. We used 5000 angular points to generate this plot at $t = 3$ and set $n = 8$. The blue curve is the analytic value given by (2.27) and the red data points denote the numerically calculated values.

With the welding problem solved to an acceptable level of accuracy, the next step is the calculation of the Schwarzian derivative which requires 3 derivatives of the solution to the welding problem w^-. It is unsurprising that taking third derivatives of a numerically calculated quantity is prone to generating large errors. More specifically, these errors not only deviated from

the analytic comparison data but would often diverge leaving problematic data to be passed to the remainder of the calculation.

The first approach tried was simply to increase the mesh density to higher and higher order but this was problematic in its own right. We recall that an increase in angular mesh density corresponds to a linear increase in data points for the inverse solution to the flow equation $\chi_t^{-1}(\theta)$. However, as stated this increase corresponds to a quadratic increase in data points for K_{ab}. This quadratic increase in data points correspondingly slowed computation time and increased memory usage. Due to these issues associated to increasing mesh points, a higher priority was put to increasing the quality and smoothness of the data being sent to K_{ab}. The smoother the data that was being sent in to the calculation of K_{ab}, the smoother the data being generated from the calculation of the Schwarzian derivative.

This smoothness of data being used was always limited by the value of the parameter t. In every tested case there was a value of t at which the derivatives of $\chi_t^{-1}(\theta)$ would numerically overflow, meaning that the data being sent to the remainder of the code would be inaccurate and unusable. Methods to ameliorate this issue included higher order finite difference calculations of the derivatives of w_b^- but these did not fix the issue as much as was hoped. This problem in being unable to calculate the Schwarzian derivative to a large value of t meant that only a small region of the Fourier transform could be calculated via (2.22). This issue of calculating smooth data to a high value of t was an issue throughout the project and is the main issue facing numerical welding methods.

With the higher order finite differencing methods, the code was able to generate good bulk agreement of the Schwarzian derivative to the analytic comparison but the end points of the curves were problematic in the sense they would have a propensity to return very large values and in some cases these would numerically overflow. We can see one such plot of the failure of the edge points in even the best case in Fig. 4.5 where

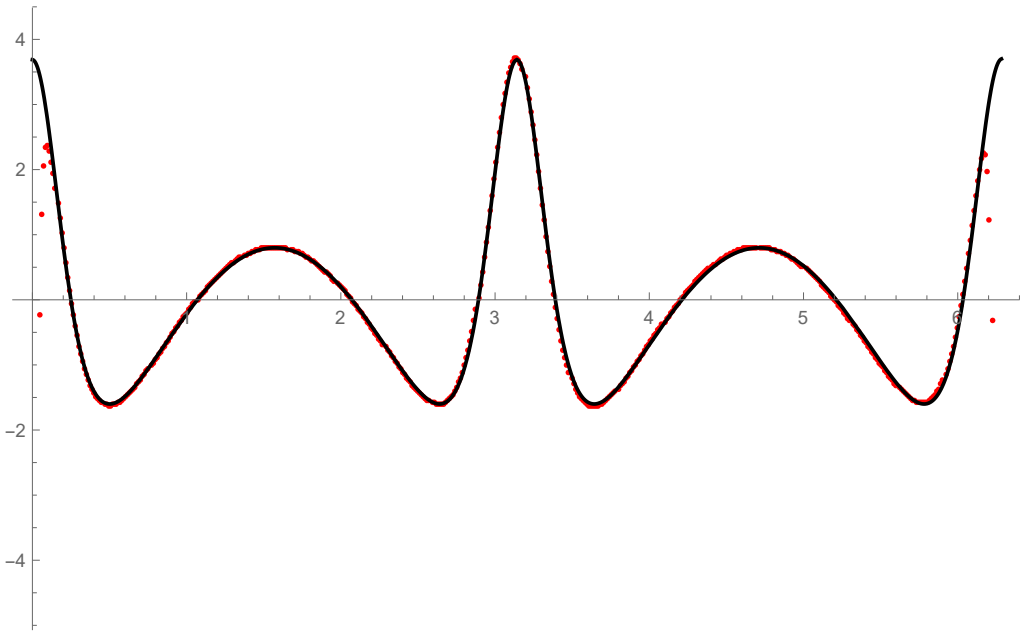

Figure 4.5: Plot of the real part of the analytic Schwarzian derivative (2.28) (black) against the numerically generated data from the method of lines flow solution for (2.24). This plot uses 500 angular data points and is calculated for $t = 1$ and $n = 2$.

the plot has been scaled to ignore the largest negative end point values to demonstrate the good agreement in the bulk calculation and the points at which the numerical derivative begins to fall away from the analytic values.

A major challenge in the project was to improve the stability and quality of the data being calculated by the Schwarzian derivative. This is unsurprising as the calculation of the Schwarzian derivative is one of the final steps after several numerically challenging steps. Even if the data from the welding solution created a smooth Jordan curve it would often not look smooth in the context of the Schwarzian plots. This highlighted that there were still several systematic errors remaining in the code that would have to be improved.

When the calculation of the Schwarzian derivative was done, the only

remaining part of the welding method to be implemented was the integral (2.22). This does not include the step of inverting the Fourier transform (2.22) to generate an explicit probability density. To numerically resolve the two integrals in (2.22) we split them up into the angular integral and then integrate this over t.

The angular integral $\Theta(\theta, t')$ given by

$$\Theta(\theta, t') = \int_S f(z) S w^-(t', z) dz, \tag{4.5}$$

is not quite the form that the code calculates. Instead of calculating for some z on the circle, the code calculates the value in θ. This means we need to use the change of variable relationship for the Schwarzian derivative (2.21), transforming our integral over the circle to

$$\Theta(\theta, t') = \int_S f\left(e^{i\theta}\right)\left(\frac{1}{2} - SF(\theta, t')\right) e^{-2i\theta} i e^{i\theta} d\theta. \tag{4.6}$$

The function F is the t dependent analogue of w^- ($F(t, \theta) = w^-(t, \exp(i\theta))$) calculated by the code which is given in terms of angular dependency. Note that the simplicity of this change of variables is due to $S(\exp(i\theta)) = 1/2$. Calculating the angular contribution is best done simply using the Euler method of integration

$$\Theta(\theta, t') \approx \sum_{j=1}^{N} f\left(e^{i\theta_j}\right)\left(\frac{1}{2} - SF(\theta_j, t')\right) e^{-2i\theta_j} i e^{i\theta_j} h. \tag{4.7}$$

The parameter $h = 2\pi/N$ replaces the metric and the value N is the number of angular points we have calculated. Due to the periodicity of the integrand we do not wish to alter the first and last contributions from the angular array as one would with perhaps Simpson's or Trapezium rules. Hence we use the method of Euler. This is because of the fact that the Euler method has a rotationally invariant set of integration weights.

This integral formula can be simplified when included with the integral over t, $\mathcal{T}$ with the constant pre-factors included to give

$$\mathcal{T}(t) = \frac{c}{24\pi} \int_0^t \int_S \frac{f\left(e^{i\theta}\right)(1 - 2SF(\theta, t'))\, e^{-i\theta}}{2} d\theta. \tag{4.8}$$

Calculation of the integral over t is set by definition to give 0 when the integral is calculating the first point. After this we use Simpson's rule to reduce the error to $\mathcal{O}(h^4)$ compared to the $\mathcal{O}(h^2)$ from the trapezoidal method. This reduction in error is vital due to often only having a small number of steps in t (relative to angular discretisation).

Following the exponentiation of $\mathcal{T}$, one has successfully used the welding method to calculate the Fourier transform of the probability distribution of the stress energy tensor corresponding to the smearing function f on the circle given by (2.22).

As discussed previously, the calculation of the welding method is troublesome for large values of t due to compounding numerical errors at many stages of the calculation. We mitigate this issue by using the method of lines to solve for the flow solution ρ_t. The bottleneck of accurate Schwarzian calculation requires very smooth data generated from both solving the flow equation and solving the welding problem via the integral operator K. With this in mind, if one simply runs the code with the large value of t that they wish to achieve then the data collected from the Fourier transform of the probability distribution is inevitably fraught with error.

To avoid this issue one is forced to run the code to very low values of t, often as low as $t = 5$, which means that very little of the transformed probability distribution is represented by the code and nullifies any possibility of accurately inverting the Fourier transform in future calculations.

This requirement of running the calculation to low t does not mean that one is unable to generate data which includes more of the transformed distribution. By increasing the central charge of the Virasoro algebra c in (2.22), one changes the representation of the distribution in Fourier space by increasing the weights of the integral contributions in the exponent (2.22). This change affects the Fourier distribution in an unsurprising manner. The values of the Fourier distribution begin at 1 (by definition) and then

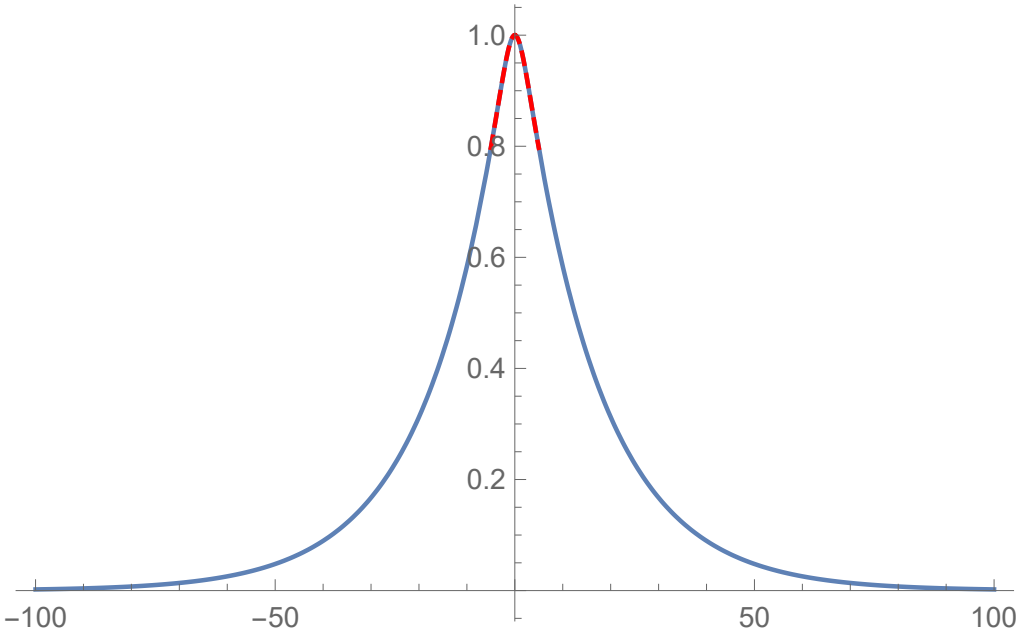

Figure 4.6: Numerically calculated and then interpolated Fourier distribution (interpolation computed by inbuilt Mathematica program) of the probability distribution (red) plotted against the analytic curve given in [12](blue) using a central charge of 1 as well as 5000 angular points and t running up to 10

monotonically decrease in magnitude below this value as the parameter t increases. Larger negative values in this exponent from increasing the value of c will cause the decay to occur faster than if c were untouched. This means that the code is able to calculate more of the support of the Fourier distribution.

To clarify this point we can once more use the toy model used throughout the generation of the welding code from [12] and observe just how much increasing the central charge can improve the data. In Fig. 4.6, only by using a large number of angular points ($N = 5000$) was the code able to run to $t \to 10$ and even then the data near $t = 10$ was beginning to incur progressively larger errors.

If one increases the central charge for the same distribution then far more

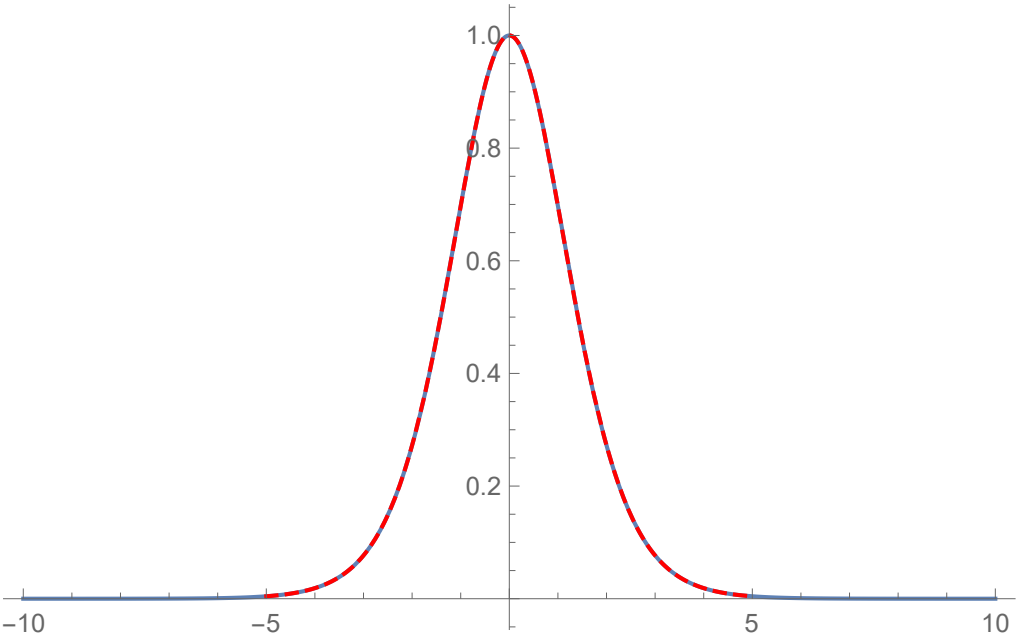

Figure 4.7: Numerically calculated and interpolated Fourier distribution (interpolation computed by inbuilt Mathematica program) of the probability distribution (red) plotted against the analytic curve given in [12] (blue) using a central charge of 24 as well as 5000 angular points and t with a maximal value of 5

of the support of the distribution can be observed, as evidenced by Fig. 4.7. Almost the full support of the transformed distribution is represented by the code despite calculating the Fourier distribution to only $t = 5$ in contrast to the calculation done to generate Fig. 4.6. After calculating the Fourier transform of the probability distribution (2.22), one would hope to invert back to real space. This is seen in the welding example where after inverting the Fourier transform one is able to calculate the probability distribution (2.32).

If we use a Gaussian test function and run the welding code and then invert our characteristic function to real space, then one can identify the failure of the welding method by the inability to agree with the singular part of the probability distribution. This is demonstrated in Fig. 4.8 and this

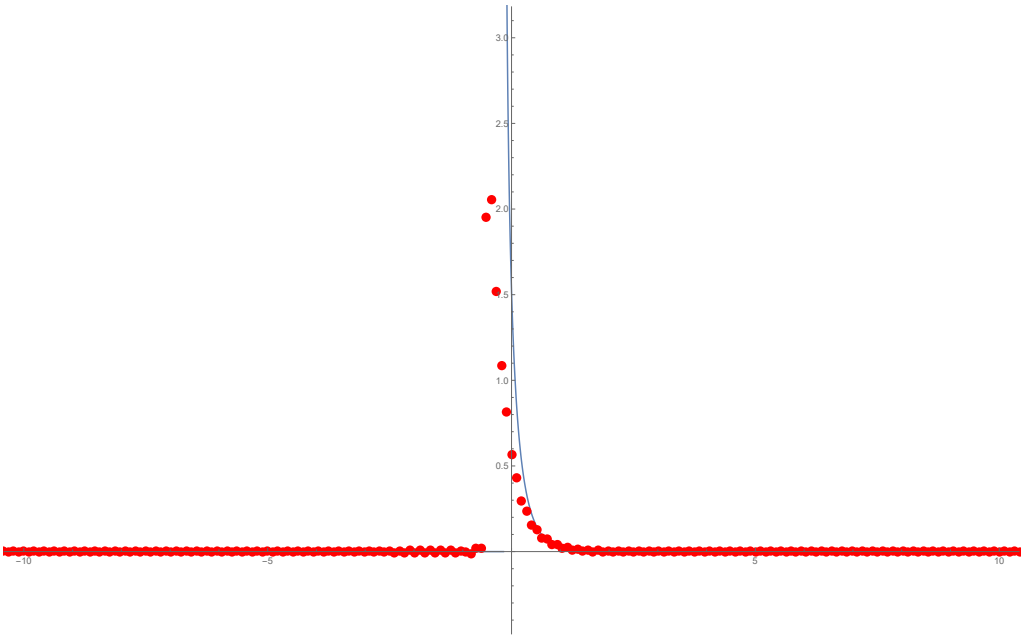

Figure 4.8: Comparison between analytic probability distribution incurred by a Gaussian test function (1.3) (blue) and the numerically Fourier transformed welding solution (red). The central charge was set as $c = 12$, we used 2000 angular points. 100 steps in t to an upper value of $t = 30$.

deviation as the code approaches the singularity is explained by not controlling enough of the behaviour near the tail of the distribution in Fourier space.

To calculate more of the detail in the tails of the Fourier transformed probability distributions, one would need to run the welding code to much higher values of t which is a limiting factor of the numerical welding method done in this way. The issue of simply increasing the central charge to cover more of the dominant behaviour of the transformed probability is that the singular behaviour disappears as the α parameter increases past 1. This can be seen in the context of (1.3) where the $\beta + \sigma$ factor in the numerator is raised to the power of $\alpha - 1$. Clearly for all $\alpha < 1$, $\lambda \to -\sigma$ this induces singular behaviour in the probability distribution which is erased as $\alpha > 1$.

Calculation of the Fourier inversion in the case of Fig. 4.8 is not done

using fast Fourier transform methods but instead we use the analytic Fourier inversion formula and calculate the result numerically. This method of using analytic results but computed partially by using numerical methods will referenced as a "quasi-analytic" approach. By integrating the generated values from (2.22) against the exponential factor in the inverse Fourier transform for a set of calculated values, one is able to generate a continuous function in real space from specific values in the Fourier domain.

Fast Fourier transform methods were not used due to the fact that there were too few data points in the t parameter domain. It was also the case that we were unable to run the code to a high enough value of t for accurate data. It was due to these facts that the alternative method of quasi-analytic inversion was used.

4.1 NUMERICAL CALCULATION OF THE SCHWARZIAN DERIVATIVE

Numerically calculating the third derivative of w^- is problematic for producing smooth data. Finite differencing methods for calculation of derivatives is sensitive in even the first and second order cases. To ensure smooth data from the calculation of the Schwarzian derivative after several initial numerical steps in the welding method, a different approach was needed. There are geometric methods [26] which can ameliorate this issue in some cases but it was unsuccessful for this project due to the proximity of the angular points which generated denominators that approached 0. These methods are based on calculating the Schwarzian derivative of $F(t,\theta) = w^-(t,\theta)$ by computing the cross ratio

$$\frac{(F(x+2h)-F(x))(F(x+h)-F(x-h))}{(F(x+h)-F(x+2h))(F(x-h)-F(x))}, \tag{4.9}$$

choosing an angular point separation h.

One is able to reduce the number of angular steps to improve this problem of singular denominators but then the calculation of the K matrix would not generate smooth data for high enough diffeomorphism parameters. To

assist the code in generating accurate data that was sensitive to reasonable perturbations in the data we made use of the welding problem itself.

4.2 FUNCTIONAL ANALYTIC CALCULATION

We wish to use the welding relation (2.18) to improve the stability and accuracy of the numerical Schwarzian derivative calculation. To do this we successively apply differential operators D to each side of (2.18) until we have calculated up to the third derivative $DDDw^-$.

Applying the third derivative operator and understanding the impact of it onto the welding problem (2.18) means that we have generated all of the necessary derivative components needed to calculate the Schwarzian derivative (2.19). By doing this, using the method we describe below, we completely remove the necessity for finite differencing methods or any explicit numerical differentiation. Instead we aim to generate far more stable and accurate data. This will mean that numerically, for each differential operator order, we transform the problem once more into a linear algebra problem exactly as we did in calculating (2.18).

We begin with recasting the welding problem (2.18), using $e_n = e^{in\theta}$ and F in place of w^-

$$e_1 = (I + K)F. \tag{4.10}$$

The integral operator K can be re-written as

$$K = \frac{\Sigma - U_\rho \Sigma U_\rho^{-1}}{2}, \tag{4.11}$$

defining Σ and U_ρ as in [[31],[12]]

$$\begin{aligned} U_\rho F(z) &= F(\rho^{-1}(z)), \\ \Sigma F &= -F + 2e_1. \end{aligned} \tag{4.12}$$

Applying a differential operator D to both sides of (4.10) gives

$$ie_1 = D(I + K)F \tag{4.13}$$

where D interacts trivially with the identity. This leaves us to understand how the differential operator interacts with K. We find that $[D, \Sigma] = 0$ and via the chain rule we can find

$$\left(DU_\rho F\right)(\theta) = \left(\chi^{-1}\right)'(\theta) F'\left(\chi^{-1}(\theta)\right). \tag{4.14}$$

This interaction can be written

$$DU_\rho = M_{(\chi^{-1})'} U_\rho D, \tag{4.15}$$

defining M_ϕ as the operation of multiplication by ϕ. We find a comparable result can be found for the inverse U_ρ^{-1}

$$DU_\rho^{-1} = U_\rho^{-1} M^{-1}_{(\chi^{-1})'} D. \tag{4.16}$$

We are now able to calculate the full effect of the differential operator on K

$$DK = \frac{\Sigma D - M_{(\chi^{-1})'} U_\rho \Sigma U_\rho M^{-1}_{(\chi^{-1})'} D}{2} = \tilde{K} D, \tag{4.17}$$

where $\tilde{K}$ is the transformed operator after being affected by the differential operator. This means we have found a welding relationship for the first order derivative of F

$$ie_1 = (I + \tilde{K}) DF. \tag{4.18}$$

This formula (4.18) means that we will numerically implement $\tilde{K}$ and solve this transformed welding problem for DF which we will use in calculation of the Schwarzian derivative.

We wish to continue this analysis to higher order but to do so we need to understand the behaviour of applying D onto our multiplication operators. We look at the general case $DM_{(\chi^{-1})'}$

$$DM^n_{(\chi^{-1})'} = nM_{(\chi^{-1})''} M^{n-1}_{(\chi^{-1})'} + M^n_{(\chi^{-1})'} D \tag{4.19}$$

and now use this to calculate the second derivative of the welding solution. In the forthcoming calculations the analysis will concentrate on the non-trivial part of $\left(\Sigma - U_\rho \Sigma U_\rho^{-1}\right)/2$, ignoring in both remaining cases the isolated Σ

term due to its commutivity with the differential operator D. We have now to calculate

$$-e_1 = DD(I+K)F = D(I+\tilde{K})DF \tag{4.20}$$

to find the formula in terms of DDF in order to calculate the second order derivative. We now need to apply the differential operator to the identity and our new integral operator $\tilde{K}$. Once again we ignore the contribution of Σ and only look at $DM_{(\chi^{-1})'}U_\rho\Sigma U_\rho M^{-1}_{(\chi^{-1})'}$

$$DM_{(\chi^{-1})'}U_\rho\Sigma U_\rho M^{-1}_{(\chi^{-1})'} = \left(M_{(\chi^{-1})''} + M_{(\chi^{-1})'}D\right)U_\rho\Sigma U_\rho^{-1}M^{-1}_{(\chi^{-1})'}. \tag{4.21}$$

We will now separate this equation into its two parts, using the chain rule we find

$$\begin{gathered} M_{(\chi^{-1})''}U_\rho\Sigma U_\rho^{-1}M^{-1}_{(\chi^{-1})'} + \\ M^2_{(\chi^{-1})'}U_\rho\Sigma U_\rho^{-1}M^{-1}_{(\chi^{-1})'}\left(-M_{(\chi^{-1})''}M^{-2}_{(\chi^{-1})'} + M^{-1}_{(\chi^{-1})'}D\right) \\ = M_{(\chi^{-1})''}U_\rho\Sigma U_\rho^{-1}M^{-1}_{(\chi^{-1})'} - \\ M^2_{(\chi^{-1})'}U_\rho\Sigma U_\rho^{-1}M_{(\chi^{-1})''}M^{-3}_{(\chi^{-1})'} + M^2_{(\chi^{-1})'}U_\rho\Sigma U_\rho^{-1}M^{-2}_{(\chi^{-1})'}D. \end{gathered} \tag{4.22}$$

Our equation has therefore become

$$\begin{aligned} -e_1 = &\left(I + \frac{1}{2}\left(\Sigma - M^2_{(\chi^{-1})'}U_\rho\Sigma U_\rho^{-1}M^{-2}_{(\chi^{-1})'}\right)\right)DDF + \\ &\frac{1}{2}\left(M^2_{(\chi^{-1})'}U_\rho\Sigma U_\rho^{-1}M_{(\chi^{-1})''}M^{-3}_{(\chi^{-1})'} - M_{(\chi^{-1})''}U_\rho\Sigma U_\rho^{-1}M^{-1}_{(\chi^{-1})'}\right)DF \end{aligned} \tag{4.23}$$

where we condense terms for brevity and find

$$-e_1 = (I+K_2)\,DDF + K_1 DF. \tag{4.24}$$

Once more we have found a welding problem to be solved which will allow us to calculate DDF without needing to differentiate it numerically. This means by using (4.18) and (4.24) we have found results which allow us to calculate the first and second order derivatives of F without needing to resort to numerical methods of differentiation.

4.3 INTEGRAL OPERATOR REALISATION AND VALIDATION OF CONTINUITY

From the calculations in the previous section we have generated expressions which gives us the first and second derivatives of the conformal welding solution. We will use this to improve the accuracy in the Schwarzian derivative. Following the implementation of the techniques for the second derivative, we will extend this idea to try to generate a continuous integral operator that will give us access to the third derivative of our welding solution. We can write KF as an integral equation and then write an analogous formula for calculation of $DDKF$

$$\begin{aligned} KF(\theta) = \frac{i}{4\pi}\int_0^{2\pi}\left[\cot\left(\frac{\theta-\theta'}{2}\right) - \right. \\ \left.\left(\chi^{-1}\right)'(\theta')\cot\left(\frac{\chi^{-1}(\theta)-\chi^{-1}(\theta')}{2}\right)\right]F(\theta')\,d\theta'. \end{aligned} \tag{4.25}$$

We will now group like terms to isolate potential singularities in our integral kernels looking first at

$$\begin{aligned} K_2DDF(\theta) = \frac{i}{4\pi}\int_0^{2\pi}\left[\cot\left(\frac{\theta-\theta'}{2}\right) - \right. \\ \left.\frac{\left(\chi^{-1}\right)'(\theta)^2}{\left(\chi^{-1}\right)'(\theta')}\cot\left(\frac{\chi^{-1}(\theta)-\chi^{-1}(\theta')}{2}\right)\right]DDF(\theta')\,d\theta', \end{aligned} \tag{4.26}$$

with K_1, K_2 as in (4.24)

$$\begin{aligned} K_1DF(\theta) = \frac{i}{4\pi}\int_0^{2\pi}\left[\frac{\left(\chi^{-1}\right)'(\theta)^2\left(\chi^{-1}\right)''(\theta')}{\left(\chi^{-1}\right)'(\theta')^2} - \right. \\ \left.\left(\chi^{-1}\right)''(\theta)\right]\cot\left(\frac{\chi^{-1}(\theta)-\chi^{-1}(\theta')}{2}\right)DF(\theta')\,d\theta'. \end{aligned} \tag{4.27}$$

We have generated these integral kernels for K_1 and K_2 by using the same logic as in [12, 31].

Using expansions around coincidence one can show that both K_1 and K_2 are continuous including the point at coincidence. Substituting $\theta = \theta' + \varepsilon$

we first check K_2. Recall the series expansion

$$\cot\left(\frac{f(\theta'+\varepsilon)-f(\theta')}{2}\right)=\frac{2}{f'(\theta)}\varepsilon^{-1}-\frac{f''(\theta)}{f'(\theta)^2}+O(\varepsilon). \tag{4.28}$$

Using this we can calculate the coincidence value of the kernel of K_2 which we denote $\mathcal{K}_2(\theta,\theta')$ and find

$$\mathcal{K}_2(\theta,\theta)=-\frac{3i\left(\chi^{-1}\right)''(\theta)}{4\left(\chi^{-1}\right)'(\theta)\pi}. \tag{4.29}$$

Now with careful substitution into the kernel of K_1 (denoted $\mathcal{K}_1(\theta,\theta')$) we generate the coincidence expression

$$\mathcal{K}_1(\theta,\theta)=i\frac{\left(\chi^{-1}\right)''(\theta)^2}{\left(\chi^{-1}\right)'(\theta)^2\pi}-i\frac{\left(\chi^{-1}\right)'''(\theta)}{2\pi\left(\chi^{-1}\right)'(\theta)}. \tag{4.30}$$

4.4 NUMERICAL IMPLEMENTATION OF THE SECOND DERIVATIVE METHOD.

We have shown that our integral kernels are continuous. We now discuss the numerical implementation for this to be of use. Previously we have converted (4.10) into a matrix problem with special consideration at coincidence. This method for our new results will be similar. We rearrange (4.24) to the following

$$(I+K_2)\,DDF=-e_1-K_1DF, \tag{4.31}$$

and will then solve the equation by discretising K_1 and K_2 as we did for K to K_{ab}. This will then allow us to use inbuilt linear algebra methods in Maple after calculating DF by solving (4.18).

The plot in Fig. 4.9 shows the comparison between the two methods of DDF calculation, one using our new method and the other using central differencing methods for low values of t. Although the overlayed graphs are visually indistinguishable, the average percentage deviation is 0.0088% with a maximum value of 0.1348%.

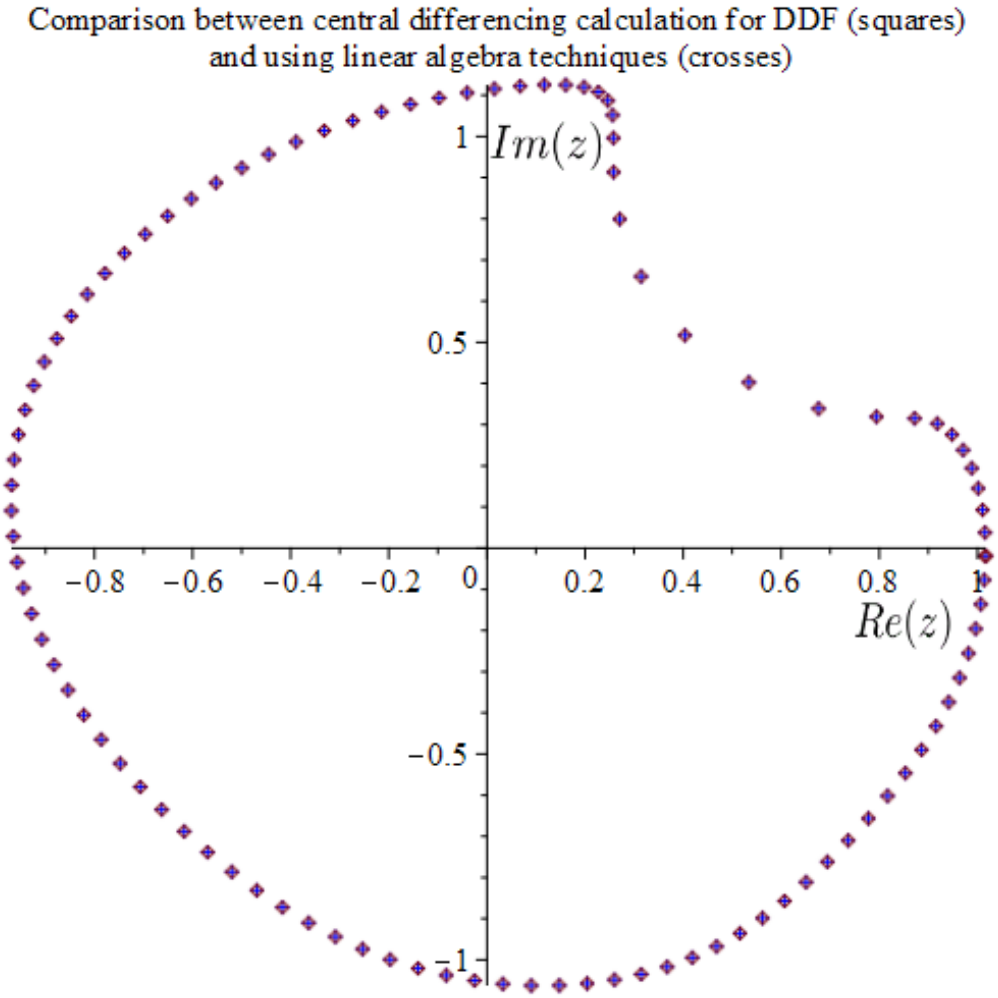

Figure 4.9: Plot demonstrating previous methods of central differencing calculating the second derivative of F for low t (ensuring stable calculation values) compared to the methods detailed using the welding method to generate direct methods of calculating DDF as in (4.31). This demonstrates the efficacy of the new method in that it agrees with our previous methods and can maintain stable solutions for higher values of t.

The new method for DDF should be more accurate because it avoids numerical differentiation. Although the errors in the old method relative to the new one are small, they would be amplified when fed into further stages of numerical differentiation (as was done using the original method) which was a large source of issues before.

We need to apply one further differential operator D to (4.24) to generate an expression for $DDDF$. This is the last calculation of this type needed because we only require an understanding of 3 derivatives to calculate the Schwarzian derivative. We will also verify smoothness of this last calculation.

4.5 THE THIRD DERIVATIVE OF THE CONFORMAL WELDING SOLUTION

We now wish to calculate $DDDF$ by applying 3 differential operators D to (4.23). The left hand side is given by $-ie_1$ but the right hand side requires more explicit calculation. Once more we will ignore the identity term in our total integral operator as well as the initial Σ term due to commutivity. The calculation will be broken down into 3 stages and then like terms will be grouped. We begin with the second order derivative term in (4.23) due to this giving us the third order differential of F and therefore need to understand

$$-D\left(M^2_{(\chi^{-1})'}U_\rho\Sigma U_\rho^{-1}M^{-2}_{(\chi^{-1})'}DDF\right). \tag{4.32}$$

This derivative first affects our multiplicative operator and generates the expression

$$\begin{aligned} &-D\left(M^2_{(\chi^{-1})'}U_\rho\Sigma U_\rho^{-1}M^{-2}_{(\chi^{-1})'}DDF\right) \\ =&-\left(2M_{(\chi^{-1})''}M_{(\chi^{-1})'}+M^2_{(\chi^{-1})'}D\right)U_\rho\Sigma U_\rho^{-1}M^{-2}_{(\chi^{-1})'}DDF, \end{aligned} \tag{4.33}$$

with the derivative operator passing through our U_ρ and associated inverse in the standard way to give us

$$\begin{aligned} &-D\left(M^2_{(\chi^{-1})'}U_\rho\Sigma U_\rho^{-1}M^{-2}_{(\chi^{-1})'}DDF\right) \\ =&-\left[2M_{(\chi^{-1})''}M_{(\chi^{-1})'}U_\rho\Sigma U_\rho^{-1}M^{-2}_{(\chi^{-1})'}DDF+\right. \\ &\left.M^3_{(\chi^{-1})'}U_\rho\Sigma U_\rho^{-1}M^{-1}_{(\chi^{-1})'}DM^{-2}_{(\chi^{-1})'}DDF\right]. \end{aligned} \tag{4.34}$$

This is resolved to give

$$\begin{aligned} &-D\left(M^2_{(\chi^{-1})'}U_\rho\Sigma U_\rho^{-1}M^{-2}_{(\chi^{-1})'}DDF\right)\\ &=-\Big[2M_{(\chi^{-1})''}M_{(\chi^{-1})'}U_\rho\Sigma U_\rho^{-1}M^{-2}_{(\chi^{-1})'}DDF+\\ &M^3_{(\chi^{-1})'}U_\rho\Sigma U_\rho^{-1}M^{-1}_{(\chi^{-1})'}\left(-2M_{(\chi^{-1})''}M^{-3}_{(\chi^{-1})'}+M^{-2}_{(\chi^{-1})'}D\right)DDF\Big]. \end{aligned} \tag{4.35}$$

This expression can be tidied up and ordered by descending derivative order to give one of our 3 calculated derivatives as

$$\begin{aligned} &-D\left(M^2_{(\chi^{-1})'}U_\rho\Sigma U_\rho^{-1}M^{-2}_{(\chi^{-1})'}DDF\right)\\ &=-M^3_{(\chi^{-1})'}U_\rho\Sigma U_\rho^{-1}M^{-3}_{(\chi^{-1})'}D^3F+\\ &2\left(M^3_{(\chi^{-1})'}U_\rho\Sigma U_\rho^{-1}M_{(\chi^{-1})''}M^{-4}_{(\chi^{-1})'}-\right.\\ &\left.M_{(\chi^{-1})''}M_{(\chi^{-1})'}U_\rho\Sigma U_\rho^{-1}M^{-2}_{(\chi^{-1})'}\right)D^2F. \end{aligned} \tag{4.36}$$

We now move to the calculation of the the positive first order derivative term of (4.23)

$$D\left(M^2_{(\chi^{-1})'}U_\rho\Sigma U_\rho^{-1}M_{(\chi^{-1})''}M^{-3}_{(\chi^{-1})'}\right)DF. \tag{4.37}$$

We begin by noticing the derivative is operating on the same multiplicative factor as for the previous term and find

$$\begin{aligned} &D\left(M^2_{(\chi^{-1})'}U_\rho\Sigma U_\rho^{-1}M_{(\chi^{-1})''}M^{-3}_{(\chi^{-1})'}\right)DF\\ &=2M_{(\chi^{-1})''}M_{(\chi^{-1})'}U_\rho\Sigma U_\rho^{-1}M_{(\chi^{-1})''}M^{-3}_{(\chi^{-1})'}DF+\\ &M^3_{(\chi^{-1})'}U_\rho\Sigma U_\rho^{-1}M^{-1}_{(\chi^{-1})'}DM_{(\chi^{-1})''}M^{-3}_{(\chi^{-1})'}DF. \end{aligned} \tag{4.38}$$

Resolving the differential of both multiplication operators gives the final result for this second calculation to be

$$\begin{aligned} &D\left(M^2_{(\chi^{-1})'}U_\rho\Sigma U_\rho^{-1}M_{(\chi^{-1})''}M^{-3}_{(\chi^{-1})'}\right)DF\\ &=M^3_{(\chi^{-1})'}U_\rho\Sigma U_\rho^{-1}M_{(\chi^{-1})''}M^{-4}_{(\chi^{-1})'}D^2F+\\ &\Big(2M_{(\chi^{-1})''}M_{(\chi^{-1})'}U_\rho\Sigma U_\rho^{-1}M_{(\chi^{-1})''}M^{-3}_{(\chi^{-1})'}+\\ &+M^3_{(\chi^{-1})'}U_\rho\Sigma U_\rho^{-1}M_{(\chi^{-1})'''}M^{-4}_{(\chi^{-1})'}-\\ &3M^3_{(\chi^{-1})'}U_\rho\Sigma U_\rho^{-1}M^2_{(\chi^{-1})''}M^{-5}_{(\chi^{-1})'}\Big)DF. \end{aligned} \tag{4.39}$$

Lastly we need to compute

$$-D\left(M_{(\chi^{-1})''}U_\rho\Sigma U_\rho^{-1}M_{(\chi^{-1})'}^{-1}\right)DF \tag{4.40}$$

and find

$$\begin{aligned}&-D\left(M_{(\chi^{-1})''}U_\rho\Sigma U_\rho^{-1}M_{(\chi^{-1})'}^{-1}\right)DF\\ =&-\Big[M_{(\chi^{-1})''}M_{(\chi^{-1})'}U_\rho\Sigma U_\rho^{-1}M_{(\chi^{-1})'}^{-2}D^2F+\\ &+\left(M_{(\chi^{-1})'''}U_\rho\Sigma U_\rho^{-1}M_{(\chi^{-1})'}^{-1}-\right.\\ &\left.M_{(\chi^{-1})''}M_{(\chi^{-1})'}U_\rho\Sigma U_\rho^{-1}M_{(\chi^{-1})''}M_{(\chi^{-1})'}^{-3}\right)DF\Big].\end{aligned} \tag{4.41}$$

At this stage we are able to break this set of equations into respective parts to find the integral operators for each order of differentiation on our conformal welding solution F. We list the grouped terms for each order and assign to them a shorthand before checking smoothness of the constituent parts. We begin with the highest order differential operator and descend

$$-P_3D^3F=-M_{(\chi^{-1})'}^3U_\rho\Sigma U_\rho^{-1}M_{(\chi^{-1})'}^{-3}D^3F, \tag{4.42}$$

$$\begin{aligned}P_2D^2F=3\Big(&M_{(\chi^{-1})'}^3U_\rho\Sigma U_\rho^{-1}M_{(\chi^{-1})''}M_{(\chi^{-1})'}^{-4}-\\ &M_{(\chi^{-1})''}M_{(\chi^{-1})'}U_\rho\Sigma U_\rho^{-1}M_{(\chi^{-1})'}^{-2}\Big)D^2F\end{aligned} \tag{4.43}$$

and lastly

$$\begin{aligned}&P_1DF\\ =&\Big[M_{(\chi^{-1})'}^3U_\rho\Sigma U_\rho^{-1}M_{(\chi^{-1})'''}M_{(\chi^{-1})'}^{-4}-M_{(\chi^{-1})'''}U_\rho\Sigma U_\rho^{-1}M_{(\chi^{-1})'}^{-1}+\\ &+3\left(M_{(\chi^{-1})''}M_{(\chi^{-1})'}U_\rho\Sigma U_\rho^{-1}M_{(\chi^{-1})''}M_{(\chi^{-1})'}^{-3}-\right.\\ &\left.M_{(\chi^{-1})'}^3U_\rho\Sigma U_\rho^{-1}M_{(\chi^{-1})''}^2M_{(\chi^{-1})'}^{-5}\right)\Big]DF.\end{aligned} \tag{4.44}$$

With these components we have found the welding equation that can be solved for $DDDF=D^3F$ is

$$-ie_1=\left(I+\frac{\Sigma-P_3}{2}\right)D^3F+P_2D^2F+P_1DF. \tag{4.45}$$

Once more we verify the smoothness of these individual terms before progressing to identification of the coincidence behaviour for numerical implementation.

4.6 VERIFICATION OF SMOOTH BEHAVIOUR OF THE THIRD DERIVATIVE INTEGRAL OPERATOR

We begin the analysis with (4.43) to understand the less obvious calculations first

$$P_2 D^2 F(\theta) = \frac{i}{4\pi}\int_0^{2\pi} 3\left[\frac{\left(\chi^{-1}\right)'(\theta)^3\left(\chi^{-1}\right)''(\theta')}{\left(\chi^{-1}\right)'(\theta')^3} - \frac{\left(\chi^{-1}\right)''(\theta)\left(\chi^{-1}\right)'(\theta)}{\left(\chi^{-1}\right)'(\theta')}\right]\cot\left(\frac{\chi^{-1}(\theta)-\chi^{-1}(\theta')}{2}\right) D^2F(\theta')\,d\theta'. \tag{4.46}$$

We perform the analysis around coincidence with the substitution $\theta = \theta' + \varepsilon$, denote the integrand $\mathcal{P}_2(\theta,\theta')$ and find that we are left with the smooth result around coincidence of

$$\mathcal{P}_2(\theta,\theta) = \frac{3i}{2\pi\left(\chi^{-1}\right)'(\theta)^2}\left[2\left(\chi^{-1}\right)''(\theta)^2 - \left(\chi^{-1}\right)'''(\theta)\left(\chi^{-1}\right)'(\theta)\right]. \tag{4.47}$$

The next case to analyse will be $P_1 DF(\theta)$. We will resolve (4.44) in two parts to break down the calculation into terms which more clearly cancel upon performing the coincidence analysis.

The resolution of (4.44) will amount to looking at the terms with third derivatives of χ^{-1} and the terms with the factor of 3 in front. First the terms with third derivatives produce the integral

$$\frac{i}{4\pi}\int_0^{2\pi}\left[\frac{\left(\chi^{-1}\right)'(\theta)^3\left(\chi^{-1}\right)'''(\theta')}{\left(\chi^{-1}\right)'(\theta')^3} - \left(\chi^{-1}\right)'''(\theta)\right]\cot\left(\frac{\chi^{-1}(\theta)-\chi^{-1}(\theta')}{2}\right) DF(\theta')\,d\theta' \tag{4.48}$$

which produces the value at coincidence to be

$$\frac{i}{2\pi\left(\chi^{-1}\right)'(\theta)^2}\left[3\left(\chi^{-1}\right)''(\theta)\left(\chi^{-1}\right)'''(\theta) - \left(\chi^{-1}\right)''''(\theta)\right]. \tag{4.49}$$

The remaining terms in (4.44) produce the integral expression

$$\frac{3i}{4\pi}\int_0^{2\pi}\left[\frac{\left(\chi^{-1}\right)''(\theta')\left(\chi^{-1}\right)'(\theta)\left(\chi^{-1}\right)''(\theta)}{\left(\chi^{-1}\right)'(\theta')^2} - \frac{\left(\chi^{-1}\right)'(\theta)^3\left(\chi^{-1}\right)''(\theta')^2}{\left(\chi^{-1}\right)'(\theta')^4}\right]\cot\left(\frac{\chi^{-1}(\theta)-\chi^{-1}(\theta')}{2}\right) DF(\theta')\,d\theta' \tag{4.50}$$

which upon expansion around coincidence gives the expression

$$\frac{3i\left(\chi^{-1}\right)''(\theta)}{2\pi\left(\chi^{-1}\right)'(\theta)^3}\left[\left(\chi^{-1}\right)'''(\theta)\left(\chi^{-1}\right)'(\theta)-2\left(\chi^{-1}\right)''(\theta)^2\right]. \tag{4.51}$$

This results in the total combined coincidence value of the integrand of the first order differential operator P_1DF as

$$\begin{aligned}\mathcal{P}_1(\theta,\theta)=&\frac{3i\left(\chi^{-1}\right)''(\theta)}{2\pi\left(\chi^{-1}\right)'(\theta)^3}\left[\left(\chi^{-1}\right)'''(\theta)\left(\chi^{-1}\right)'(\theta)-2\left(\chi^{-1}\right)''(\theta)^2\right]+\\&\frac{i}{2\pi\left(\chi^{-1}\right)'(\theta)^2}\left[3\left(\chi^{-1}\right)''(\theta)\left(\chi^{-1}\right)'''(\theta)-\left(\chi^{-1}\right)''''(\theta)\right],\end{aligned} \tag{4.52}$$

using $\mathcal{P}_1(\theta,\theta)$ to denote the integrand coincidence value.

We have reached the final stage of the verification of smoothness. We have to include the neglected Σ term because this will operate on D^3F as well. This gives us $(\Sigma - P_3)\,D^3F/2$ which is represented by

$$\begin{aligned}(\Sigma-P_3)\,D^3F/2=&\frac{i}{4\pi}\int_0^{2\pi}\left[\cot\left(\frac{\theta-\theta'}{2}\right)-\right.\\&\left.\frac{\left(\chi^{-1}\right)'(\theta)^3}{\left(\chi^{-1}\right)'(\theta')^2}\cot\left(\frac{\chi^{-1}(\theta)-\chi^{-1}(\theta')}{2}\right)\right]D^3F(\theta')\,d\theta'.\end{aligned} \tag{4.53}$$

We use the same kernel expansion technique and find that the value at coincidence for the third derivative integrand $\mathcal{P}_3(\theta,\theta')$ of our welding solution is given by

$$\mathcal{P}_3(\theta,\theta)=-5\frac{\left(\chi^{-1}\right)''(\theta)}{\left(\chi^{-1}\right)'(\theta)}. \tag{4.54}$$

We have now verified that all factors of this third order derivative give smooth integral kernels and is appropriate to be used within the numerical techniques of the welding method. The numerical implementation of D^3F is similar to the methods for the D^2F and the discretisation of K to K_{ab}. The obvious limiting factor to this method is in the quality of the derivatives of χ^{-1}. If one is able to generate analytic derivatives of χ^{-1} up to fourth order which are smooth throughout the range, then this should allow for sensible data to be produced.

We have demonstrated the key ideas required for numerical implementation of the extended welding method as well as the analytic techniques used to further assist the code. At this stage one is able to use the welding method to improve the calculation of the Schwarzian derivative in accuracy and stability.

— 5 —

Implementation of the welding method: Part 2

Following the last chapter, a further method of analytic assistance is demonstrated to aid the numerical welding method. As discussed, the Schwarzian derivative is prone to instability due to the requirement for third order derivatives of the welding solution in order to calculate it. We have used the welding problem to generate analytic derivative values to ameliorate this issue but we also can aid the data going into the Schwarzian calculation step. We wish to develop a method, which we call "pre-processing", that allows us to maintain good numerical stability for larger values of t by appropriately adjusting the data as it enters the numerical solvers.

5.1 PRE-PROCESSING TO FACILITATE LONGER TERM NUMERICAL STABILITY

Recall that in the welding problem, given some $\rho \in \text{Diff}^+(\mathbb{S})$ we wish to find $w^{\pm}$ such that

$$w^+(z) = w^- \circ \rho(z) \quad z \in \mathbb{S}, \tag{5.1}$$

with w^+ holomorphic in $\Delta^+ = \{z \in \mathbb{C} || z| < 1\}$ and w^- holomorphic in $\Delta^- = \{z \in \mathbb{C} || z| > 1\}$, just as before.

Consider a modified family of diffeomorphisms

$$\tilde{\rho} = \mu \circ \rho, \tag{5.2}$$

for Moebius transforms $\mu \in \mathrm{Diff}(\mathbb{S})$. Suppose also that we have that $\tilde{w}^{\pm}$ solves the welding problem for $\tilde{\rho}$ then

$$\tilde{w}^{+} = \tilde{w}^{-} \circ \tilde{\rho} = \tilde{w}^{-} \circ \mu \circ \rho. \tag{5.3}$$

This means that

$$w^{+} = \tilde{w}^{+} \tag{5.4}$$

and

$$w^{-} = \tilde{w}^{-} \circ \mu \tag{5.5}$$

solve the welding problem for ρ.

The Schwarzian chain rule gives

$$(Sw^{-})(z) = S\left(\tilde{w}^{-}(\mu(z))\right) = \mu'(z)^2 \left(S\tilde{w}^{-}\right)(\mu(z)) \tag{5.6}$$

allowing us to modify the integrand in (2.22) to correct for the pre-processing and generate the Fourier transform of the probability distribution as if we had not performed this change. We begin with the integrand as before

$$\int_S f(z) Sw^{-}(z) dz = \int_S f(z)\mu'(z)^2 \left(S\tilde{w}^{-}\right)(\mu(z)) dz \tag{5.7}$$

and use the coordinate change $\omega = \mu(z)$

$$\int_S f(z) Sw^{-}(z) dz = \int f(\mu^{-1}(\omega))\mu'(\mu^{-1}(\omega)) \left(S\tilde{w}^{-}\right)(\omega) d\omega. \tag{5.8}$$

Using the identity $\mu'(\mu^{-1}(\omega)) = 1/(\mu^{-1})'(\omega)$ we reach the formula

$$\int_S f(z) Sw^{-}(z) dz = \int_S \frac{f(\mu^{-1}(\omega))}{(\mu^{-1})'(\omega)} \left(S\tilde{w}^{-}\right)(\omega) d\omega. \tag{5.9}$$

Generally when using the numerical solver we begin by solving the flow on the line and then transform to the circle in order to benefit from the methods detailed in [12]. The equivalent problem on $\mathbb{R}$ is given via $\Theta(g) \to T(f)$, $g \in C^{\infty}(\mathbb{R})$ and $f \in C^{\infty}(\mathbb{T})$ where the test functions are related using the transformation rule

$$f(z) = C'\left(C^{-1}(z)\right) g\left(C^{-1}(z)\right), \tag{5.10}$$

C and its inverse denoting Cayley transforms (1.15). We can then relate the flow ψ_t on the line to the flow ρ_t on the circle

$$\psi_t = C^{-1} \circ \rho_t \circ C \tag{5.11}$$

and ψ_t obeys conditions equivalent to the rules for the flow on the circle

$$\partial_t \psi_t(u) = g(\psi_t(u)), \quad \psi_0(u) = u. \tag{5.12}$$

Using these properties we can determine ρ_t from the smearing function on the line by solving (5.12) and inverting (5.11)

$$\rho_t(z) = \left(C \circ \psi_t \circ C^{-1}\right)(z). \tag{5.13}$$

Expressed in terms of θ we have

$$\rho_t\left(e^{i\theta}\right) = e^{i\chi_t(\theta)}, \tag{5.14}$$

which can therefore be related to the flow on the line

$$e^{i\chi_t(\theta)} = C\left(\psi_t\left(C^{-1}\left(e^{i\theta}\right)\right)\right). \tag{5.15}$$

We can use the definition $C^{-1}(e^{i\theta}) = \tan(\theta/2)$ to rewrite this expression in terms of the angular flow $\chi_t(\theta) = 2\tan^{-1}(\psi_t(\tan(\theta/2)))$. The solution to the welding problem requires knowledge of the inverse of the angular flow χ_t^{-1} and the derivative of the angular flow $\left(\chi_t^{-1}\right)'$. We can simply find the inverse of the angular flow as

$$\chi_t^{-1}(\theta) = 2\tan^{-1}\left(\psi_t^{-1}\left(\tan\left(\frac{\theta}{2}\right)\right)\right). \tag{5.16}$$

One should note that the inverse of the flow in either case is given by replacing the parameter t by $-t$. The same can not be said in generality for pre-processed flows. Calculation of the derivatives of the flows $(\psi_t)'$ can be done by recasting (5.12) as in (2.11)

$$G(u) - G(\psi_{-t}(u)) = -t. \tag{5.17}$$

From this point we take a spatial derivative and we can rearrange to find

$$(\psi_{-t})'(u) = \frac{g(\psi_{-t}(u))}{g(u)}, \tag{5.18}$$

which can be used in

$$(\chi_{-t})'(\theta) = \frac{(\psi_{-t})'\left(\tan\left(\frac{\theta}{2}\right)\right)}{\cos\left(\frac{\theta}{2}\right)^2\left(1+\psi_{-t}(\tan\left(\frac{\theta}{2}\right))^2\right)}, \tag{5.19}$$

following from (5.16), to give the general result

$$(\chi_{-t})'(\theta) = \frac{g\left(\psi_{-t}\left(\tan\left(\frac{\theta}{2}\right)\right)\right)}{g(\tan\left(\frac{\theta}{2}\right))}\frac{1}{\cos\left(\frac{\theta}{2}\right)^2\left(1+\psi_{-t}(\tan\left(\frac{\theta}{2}\right))^2\right)}. \tag{5.20}$$

This shows that provided we have the test function g, the flow ψ_t and derivative g' we don't require numerical derivatives of the flow on the circle χ_{-t}.

5.1.1 Pre-processing for the Gauss, Lorentz and Gauss-Lorentz test functions

With the general framework constructed we can calculate the specific impact of choosing one such pre-processing to aid in the calculation of the Fourier transform of the probability distribution incurred through using a Gaussian, Lorentzian or combination test function. Let ψ_t be the flow on the line as before induced by a test function g related via the flow equation (5.12). We define a modified flow $\tilde{\psi}_t$ via

$$\tilde{\psi}_t(u) = \psi_t(u) - \psi_t(0). \tag{5.21}$$

This modified flow has the property $\tilde{\psi}_t(0) = 0$ because we wish to keep the peak centred at 0. The issue without this pre-processing is that after enough evolution of the parameter t the peak moves outside of the numerical grid. We have the relationship (5.13) from which we will extend and define

$$\tilde{\rho}_t(z) = \left(C \circ \tilde{\psi}_t \circ C^{-1}\right)(z) = C\left(C^{-1}(\rho_t(z)) - \psi_t(0)\right) = (\mu_t \circ \rho_t)(z), \tag{5.22}$$

with $\mu_t(\omega) = C\left(C^{-1}(\omega) - \psi_t(0)\right)$ a Möbius transform and inverse $\mu_t^{-1}(\omega) = C\left(C^{-1}(\omega) + \psi_t(0)\right)$. We are able to relate the test function g to the test function f using this specific pre-processing and substituting in (5.10) to find

$$f(\mu_t^{-1}(z)) = C'\left(C^{-1}(\mu_t^{-1}(z))\right) g(\psi_t(0) + C^{-1}(z)), \tag{5.23}$$

specifying also the derivative of the inverse of the pre-processing

$$\left(\mu_t^{-1}\right)'(z) = C'\left(C^{-1}\left(\mu_t^{-1}(z)\right)\right)\left(C^{-1}\right)'(z). \tag{5.24}$$

Using these formulae we can re-write (5.9) as well as changing coordinates ($z = e^{i\theta}$) to find

$$\int_S f(z) S w^-(z) dz = i \int_{-\pi}^{\pi} \frac{g(\psi_t(0) + \tan\left(\frac{\theta}{2}\right))}{\left(C^{-1}\right)'(e^{i\theta})} (S\tilde{w}^-)(e^{i\theta}) e^{i\theta} d\theta \tag{5.25}$$

which upon substitution of the denominator and the Schwarzian chain rule (2.21) for $F(\theta) = \tilde{w}^-(e^{i\theta})$

$$(S\tilde{w}^-)(e^{i\theta}) = \left(\frac{1}{2} - SF(\theta)\right) e^{-2i\theta}. \tag{5.26}$$

We simplify (5.25) to

$$\int_S f(z) S w^-(z) dz = -\int_{-\pi}^{\pi} g(\psi_t(0) + \tan\left(\frac{\theta}{2}\right))(1 - 2SF(\theta)) e^{-i\theta} \cos\left(\frac{\theta}{2}\right)^2 d\theta. \tag{5.27}$$

The pre-processed flow on the circle in angular coordinates is given by

$$\tilde{\chi}_t^{-1}(\theta) = 2\tan^{-1}\left(\psi_{-t}\left(\psi_t(0) + \tan\left(\frac{\theta}{2}\right)\right)\right), \tag{5.28}$$

from which we can obtain

$$\left(\tilde{\chi}_t^{-1}\right)'(\theta) = \frac{\cos\left(\frac{\tilde{\chi}_t^{-1}(\theta)}{2}\right)^2}{\cos\left(\frac{\theta}{2}\right)^2} \frac{g(\tan\left(\frac{\tilde{\chi}_t^{-1}(\theta)}{2}\right))}{g(\psi_t(0) + \tan\left(\frac{\theta}{2}\right))}. \tag{5.29}$$

To take full advantage of this analytic assistance to the numerical method we take two more derivatives of this function to be used in the code. The second order derivative is given by

$$\left(\tilde{\chi}_t^{-1}\right)''(\theta) = \left(\tilde{\chi}_t^{-1}\right)'(\theta)^2 \left(\frac{L\left(g\left(\tan\left(\frac{\tilde{\chi}_t^{-1}(\theta)}{2}\right)\right)\right)}{2\cos\left(\frac{\tilde{\chi}_t^{-1}(\theta)}{2}\right)^2} - \tan\left(\frac{\tilde{\chi}_t^{-1}(\theta)}{2}\right) \right) - (\tilde{\chi}_t^{-1})'(\theta) \left(\frac{L\left(g\left(\tan\left(\frac{\theta}{2}\right)\right)\right)}{2\cos\left(\frac{\theta}{2}\right)^2} - \tan\left(\frac{\theta}{2}\right) \right), \quad (5.30)$$

using L to denote (in a slight abuse of notation)

$$L(f(x)) = \frac{f'(x)}{f(x)}. \quad (5.31)$$

With terms in (5.30) grouped for simplification we are able to take one further derivative to arrive at the third derivative of the inverse of the pre-processed flow solution on the circle. This is a lengthier calculation and as such is broken up into constituent parts before final reassembly. First we simply take the angular derivative

$$\begin{aligned}\left(\tilde{\chi}_t^{-1}\right)'''(\theta) = {} & 2\left(\tilde{\chi}_t^{-1}\right)''(\theta)\left(\tilde{\chi}_t^{-1}\right)'(\theta) \left(\frac{L\left(g\left(\tan\left(\frac{\tilde{\chi}_t^{-1}(\theta)}{2}\right)\right)\right)}{2\cos\left(\frac{\tilde{\chi}_t^{-1}(\theta)}{2}\right)^2} - \tan\left(\frac{\tilde{\chi}_t^{-1}(\theta)}{2}\right) \right) + \\ & + \left(\tilde{\chi}_t^{-1}\right)'(\theta)^2 \left(\frac{L\left(g\left(\tan\left(\frac{\tilde{\chi}_t^{-1}(\theta)}{2}\right)\right)\right)}{2\cos\left(\frac{\tilde{\chi}_t^{-1}(\theta)}{2}\right)^2} - \tan\left(\frac{\tilde{\chi}_t^{-1}(\theta)}{2}\right) \right)' - \\ & - \left(\tilde{\chi}_t^{-1}\right)''(\theta) \left(\frac{L\left(g\left(\psi_t(0) + \tan\left(\frac{\theta}{2}\right)\right)\right)}{2\cos\left(\frac{\theta}{2}\right)^2} - \tan\left(\frac{\theta}{2}\right) \right) - \\ & - \left(\tilde{\chi}_t^{-1}\right)'(\theta) \left(\frac{L\left(g\left(\psi_t(0) + \tan\left(\frac{\theta}{2}\right)\right)\right)}{2\cos\left(\frac{\theta}{2}\right)^2} - \tan\left(\frac{\theta}{2}\right) \right)'. \end{aligned} \quad (5.32)$$

Looking at the second term we find

$$\left(\frac{L\left(g\left(\tan\left(\frac{\tilde{\chi}_t^{-1}(\theta)}{2}\right)\right)\right)}{2\cos\left(\frac{\tilde{\chi}_t^{-1}(\theta)}{2}\right)^2}-\tan\left(\frac{\tilde{\chi}_t^{-1}(\theta)}{2}\right)\right)'=\frac{g''\left(\tan\left(\frac{\tilde{\chi}_t^{-1}(\theta)}{2}\right)\right)\left(\tilde{\chi}_t^{-1}\right)'(\theta)}{4g\left(\tan\left(\frac{\tilde{\chi}_t^{-1}(\theta)}{2}\right)\right)\cos\left(\frac{\tilde{\chi}_t^{-1}(\theta)}{2}\right)^4}-$$
$$-\frac{L^2\left(g\left(\tan\left(\frac{\tilde{\chi}_t^{-1}(\theta)}{2}\right)\right)\right)\left(\tilde{\chi}_t^{-1}\right)'(\theta)}{4\cos\left(\frac{\tilde{\chi}_t^{-1}(\theta)}{2}\right)^4}+$$
$$+\frac{L\left(g\left(\tan\left(\frac{\tilde{\chi}_t^{-1}(\theta)}{2}\right)\right)\right)\tan\left(\frac{\tilde{\chi}_t^{-1}(\theta)}{2}\right)\left(\tilde{\chi}_t^{-1}\right)'(\theta)}{2\cos\left(\frac{\tilde{\chi}_t^{-1}(\theta)}{2}\right)^2}-$$
$$-\frac{\left(\tilde{\chi}_t^{-1}\right)'(\theta)}{2\cos\left(\frac{\tilde{\chi}_t^{-1}(\theta)}{2}\right)^2},\tag{5.33}$$

the fourth term is similar and gives us

$$\left(\frac{L\left(g\left(\psi_t(0)+\tan\left(\frac{\theta}{2}\right)\right)\right)}{2\cos\left(\frac{\theta}{2}\right)^2}-\tan\left(\frac{\theta}{2}\right)\right)'=\frac{\tan\left(\frac{\theta}{2}\right)L\left(g\left(\psi_t(0)+\tan\left(\frac{\theta}{2}\right)\right)\right)}{2\cos\left(\frac{\theta}{2}\right)^2}+$$
$$+\frac{g''\left(\psi_t(0)+\tan\left(\frac{\theta}{2}\right)\right)}{4g\left(\psi_t(0)+\tan\left(\frac{\theta}{2}\right)\right)\cos\left(\frac{\theta}{2}\right)^4}-$$
$$-\frac{L\left(g\left(\psi_t(0)+\tan\left(\frac{\theta}{2}\right)\right)\right)^2}{4\cos\left(\frac{\theta}{2}\right)^4}-$$
$$-\frac{1}{2\cos\left(\frac{\theta}{2}\right)^2}.\tag{5.34}$$

Putting the parts together we find the lengthy expression for our third derivative to be

$$\left(\tilde{\chi}_t^{-1}\right)'''(\theta) =$$

$$2\left(\tilde{\chi}_t^{-1}\right)''(\theta)\left(\tilde{\chi}_t^{-1}\right)'(\theta)\left(\tilde{\chi}_t^{-1}\right)'(\theta)\left(\frac{L\left(g\left(\tan\left(\frac{\tilde{\chi}_t^{-1}(\theta)}{2}\right)\right)\right)}{2\cos\left(\frac{\tilde{\chi}_t^{-1}(\theta)}{2}\right)^2}-\tan\left(\frac{\tilde{\chi}_t^{-1}(\theta)}{2}\right)\right)+$$

$$\left(\tilde{\chi}_t^{-1}\right)'(\theta)^2\left(\frac{g''\left(\tan\left(\frac{\tilde{\chi}_t^{-1}(\theta)}{2}\right)\right)\left(\tilde{\chi}_t^{-1}\right)'(\theta)}{4g\left(\tan\left(\frac{\tilde{\chi}_t^{-1}(\theta)}{2}\right)\right)\cos\left(\frac{\tilde{\chi}_t^{-1}(\theta)}{2}\right)^4}-\right.$$

$$\frac{L^2\left(g\left(\tan\left(\frac{\tilde{\chi}_t^{-1}(\theta)}{2}\right)\right)\right)\left(\tilde{\chi}_t^{-1}\right)'(\theta)}{4\cos\left(\frac{\tilde{\chi}_t^{-1}(\theta)}{2}\right)^4}+$$

$$\frac{L\left(g\left(\tan\left(\frac{\tilde{\chi}_t^{-1}(\theta)}{2}\right)\right)\right)\tan\left(\frac{\tilde{\chi}_t^{-1}(\theta)}{2}\right)\left(\tilde{\chi}_t^{-1}\right)'(\theta)}{2\cos\left(\frac{\tilde{\chi}_t^{-1}(\theta)}{2}\right)^2}-$$

$$\left.\frac{\left(\tilde{\chi}_t^{-1}\right)'(\theta)}{2\cos\left(\frac{\tilde{\chi}_t^{-1}(\theta)}{2}\right)^2}\right)-$$

$$\left(\tilde{\chi}_t^{-1}\right)''(\theta)\left(\frac{L\left(g\left(\psi_t(0)+\tan\left(\frac{\theta}{2}\right)\right)\right)}{2\cos\left(\frac{\theta}{2}\right)^2}-\tan\left(\frac{\theta}{2}\right)\right)-$$

$$-\left(\tilde{\chi}_t^{-1}\right)'(\theta)\left(\frac{\tan\left(\frac{\theta}{2}\right)L\left(g\left(\psi_t(0)+\tan\left(\frac{\theta}{2}\right)\right)\right)}{2\cos\left(\frac{\theta}{2}\right)^2}+\frac{g''\left(\psi_t(0)+\tan\left(\frac{\theta}{2}\right)\right)}{4g\left(\psi_t(0)+\tan\left(\frac{\theta}{2}\right)\right)\cos\left(\frac{\theta}{2}\right)^4}-\right.$$

$$\left.-\frac{L\left(g\left(\psi_t(0)+\tan\left(\frac{\theta}{2}\right)\right)\right)^2}{4\cos\left(\frac{\theta}{2}\right)^4}-\frac{1}{2\cos\left(\frac{\theta}{2}\right)^2}\right). \tag{5.35}$$

Using (5.30) we can further manipulate (5.35) to find our third derivative

$$\begin{aligned}
\left(\tilde{\chi}_t^{-1}\right)'''(\theta) = \left(\tilde{\chi}_t^{-1}\right)''(\theta)\left(\tilde{\chi}_t^{-1}\right)'(\theta)\left(\frac{L\left(g\left(\tan\left(\frac{\tilde{\chi}_t^{-1}(\theta)}{2}\right)\right)\right)}{2\cos\left(\frac{\tilde{\chi}_t^{-1}(\theta)}{2}\right)^2} - \tan\left(\frac{\tilde{\chi}_t^{-1}(\theta)}{2}\right)\right) \\
+\frac{\left(\tilde{\chi}_t^{-1}\right)''(\theta)^2}{\left(\tilde{\chi}_t^{-1}\right)'(\theta)} + \\
+\left(\tilde{\chi}_t^{-1}\right)'(\theta)^2\frac{\sec\left(\frac{\tilde{\chi}_t^{-1}(\theta)}{2}\right)^2}{2}\left(\tan\left(\frac{\tilde{\chi}_t^{-1}(\theta)}{2}\right)L\left(g\left(\tan\left(\frac{\tilde{\chi}_t^{-1}(\theta)}{2}\right)\right)\right)\left(\tilde{\chi}_t^{-1}\right)'(\theta) - \\
\left(\tilde{\chi}_t^{-1}\right)'(\theta) + \\
\frac{\sec\left(\frac{\tilde{\chi}_t^{-1}(\theta)}{2}\right)^2}{2}\left(\tilde{\chi}_t^{-1}\right)'(\theta)\frac{g''\left(\tan\left(\frac{\tilde{\chi}_t^{-1}(\theta)}{2}\right)\right)}{g\left(\tan\left(\frac{\tilde{\chi}_t^{-1}(\theta)}{2}\right)\right)} - \\
\frac{\sec\left(\frac{\tilde{\chi}_t^{-1}(\theta)}{2}\right)^2}{2}L^2\left(g\left(\tan\left(\frac{\tilde{\chi}_t^{-1}(\theta)}{2}\right)\right)\right)\left(\tilde{\chi}_t^{-1}\right)'(\theta) \\
-\left(\tilde{\chi}_t^{-1}\right)'(\theta)\frac{\sec\left(\frac{\theta}{2}\right)^2}{2}\left(\tan\left(\frac{\theta}{2}\right)L\left(g\left(\psi_t(0)+\tan\left(\frac{\theta}{2}\right)\right)\right) + \right. \\
\frac{\sec\left(\frac{\theta}{2}\right)^2}{2}\frac{g''\left(\psi_t(0)+\tan\left(\frac{\theta}{2}\right)\right)}{g\left(\psi_t(0)+\tan\left(\frac{\theta}{2}\right)\right)} - \\
\left.\frac{\sec\left(\frac{\theta}{2}\right)^2}{2}L^2\left(g\left(\psi_t(0)+\tan\left(\frac{\theta}{2}\right)\right)\right) - 1\right).
\end{aligned} \tag{5.36}$$

5.1.2 Pre-processing for the plateau test function

One pre-processing method will not suit all test functions, they have to be tailored specifically for the properties of the test function itself. We wish to test the effects of varying plateau length and switch on length of the averaging function on the probability distribution. As a basis we choose the

switch on function

$$S(x) = \frac{1}{\beta(4,4)}\left(-\frac{1}{7}x^7 + \frac{1}{2}x^6 - \frac{3}{5}x^5 + \frac{1}{4}x^4\right), \tag{5.37}$$

using β to denote the Beta function which we define in terms of Γ functions

$$\beta(x,y) = \frac{\Gamma(x)\Gamma(y)}{\Gamma(x+y)}. \tag{5.38}$$

This switch on function is used as well as a shifted and mirrored equivalent which forms the switch off function and these are connected by a constant plateau. Using the β function ensures that the switch on and switch off functions peak at 1 and then are connected by a constant value of 1 until the switch off portion occurs. Numerically this is implemented using Heaviside functions and the test function is given by

$$\begin{aligned} g(x) = &\left(\vartheta\left(x\right) - \vartheta\left(x-s\right)\right) S\left(\frac{x}{s}\right) \\ &+\vartheta\left(x-s\right) - \vartheta\left(x-\tau-s\right) \\ &+\left(\vartheta\left(x-\tau-s\right) - \vartheta\left(x-\tau-2\,s\right)\right) S\left(-\frac{x-\tau-2\,s}{s}\right) \end{aligned} \tag{5.39}$$

defining s as the switch on length, τ as the plateau length and using ϑ to denote the Heaviside function. We plot (5.39) centered around the origin in Fig. 5.1. We choose the pre-processing for the plateau case to be

$$\tilde{\psi}_t(u) = (1+t)\psi_t(u), \quad \tilde{\psi}_0(u) = \psi_0(u) = u. \tag{5.40}$$

Following a similar pattern of analysis as in the Gauss-Lorentz case we identify comparable formulae to calculate the transformed probability distribution. We define our pre-processing

$$\mu_t(\omega) = C\left((1+t)C^{-1}(\omega)\right) \tag{5.41}$$

and its inverse

$$\mu_t^{-1}(\omega) = C\left(\frac{C^{-1}(\omega)}{1+t}\right). \tag{5.42}$$

Once more calculating the derivative of this pre-processing to use in the transformed integral

$$\left(\mu_t^{-1}\right)'(z) = C'\left(C^{-1}\left(\mu_t^{-1}(z)\right)\right)\left(\frac{C^{-1}(z)}{1+t}\right)' \tag{5.43}$$

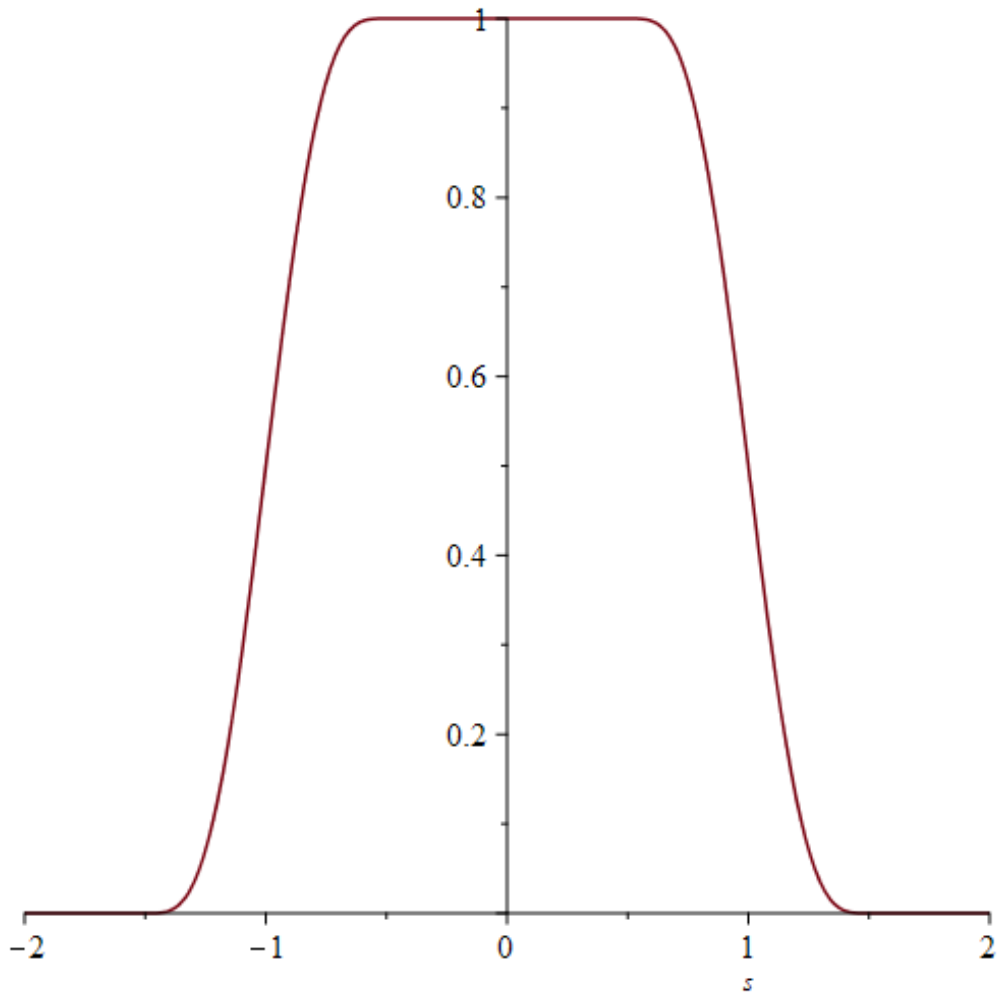

Figure 5.1: Plot of (5.39) with a switch on length of 1, a plateau length of 1 and switch off length equal to 1 as well.

and the test function relationship can be derived in this case once more using (5.10)

$$f(\mu_t^{-1}(z)) = C'\left(C^{-1}\left(\mu_t^{-1}(z)\right)\right) g\left(\frac{C^{-1}(z)}{1+t}\right). \tag{5.44}$$

With these formulae we are now able to calculate the specific method of correcting for the use of pre-processing in our integrand. We use the same change of coordinates as before giving

$$\int_S f(z)Sw^-(z)dz = -\int_{-\pi}^{\pi}(1+t)g\left(\frac{\tan\left(\frac{\theta}{2}\right)}{1+t}\right)(1-2SF(\theta))e^{-i\theta}\cos\left(\frac{\theta}{2}\right)^2 d\theta. \tag{5.45}$$

The inverse angular flow can be found in a similar way as before as well

$$\tilde{\chi}_t^{-1}(\theta) = 2\tan^{-1}\left(\psi_{-t}\left(\frac{\tan\left(\frac{\theta}{2}\right)}{1+t}\right)\right) \tag{5.46}$$

which we differentiate

$$\left(\tilde{\chi}_t^{-1}\right)'(\theta) = \frac{(\psi_{-t})'\left(\frac{\tan\left(\frac{\theta}{2}\right)}{1+t}\right)\left(1+\tan\left(\frac{\theta}{2}\right)^2\right)}{(1+t)(1+\psi_{-t}\left(\frac{\tan\left(\frac{\theta}{2}\right)}{1+t}\right)^2)} \tag{5.47}$$

and simplify using (5.18) to find

$$\left(\tilde{\chi}_t^{-1}\right)'(\theta) = \frac{g(\psi_{-t}\left(\frac{\tan\left(\frac{\theta}{2}\right)}{1+t}\right)}{g\left(\frac{\tan\left(\frac{\theta}{2}\right)}{1+t}\right)}\frac{1}{(1+t)\cos\left(\frac{\theta}{2}\right)^2\left(1+\psi_{-t}\left(\frac{\tan\left(\frac{\theta}{2}\right)}{1+t}\right)^2\right)}. \tag{5.48}$$

We calculate one further derivative to fully take advantage of the values that the code is able to calculate analytically. Differentiating (5.48) and substituting $\phi = \theta/2$ and $\xi = \tan(\phi)/(1+t)$ gives

$$\begin{gathered}\left(\tilde{\chi}_t^{-1}\right)''(\theta) = \frac{g'(\psi(\xi))(\psi_{-t})'(\xi)}{(1+t)^2 g(\xi)\cos(\phi)^4(1+\psi_{-t}(\phi)^2)} - \\ \frac{g(\psi_{-t}(\xi))g'(\xi)}{g(\xi)^2(1+t)^2\cos(\phi)^4(1+\psi_{-t}(\xi)^2)} + \frac{g(\psi_{-t}(\xi))\sin(\phi)}{g(\xi)(1+t)\cos(\phi)(1+\psi_{-t}(\xi)^2)} - \\ \frac{2g(\psi_{-t}(\xi))\psi_{-t}(\xi)(\psi_{-t})'(\xi)}{g(\xi)(1+t)^2\cos(\phi)^4(1+\psi_{-t}(\xi)^2)^2}\end{gathered} \tag{5.49}$$

which we will simplify to remove the derivatives of the flow solution on the line and factorise using the same simplifying substitutions as before to find

$$\left(\tilde{\chi}_t^{-1}\right)''(\theta) = \frac{g'(\psi_{-t}(\xi))}{g(\xi)} \frac{1}{(1+t)^2\cos(\phi)^4(1+\psi_{-t}(\xi)^2)} \left(\frac{g(\psi_{-t}(\xi))}{g(\xi)} - \frac{g'(\xi)}{g(\xi)} + \sin(\phi)\cos(\phi)(1+t) - \frac{2g(\psi_{-t}(\xi))\psi_{-t}(\xi)}{g(\xi)(1+\psi_{-t}(\xi)^2)}\right). \tag{5.50}$$

We can in fact simplify this once more by using the definition (5.48) as our pre-factor to our enclosed terms

$$\left(\tilde{\chi}_t^{-1}\right)''(\theta) = \frac{\left(\tilde{\chi}_t^{-1}\right)'(\theta)}{\cos(\phi)^2} \left(\frac{g(\psi_{-t}(\xi))}{g(\xi)} - \frac{g'(\xi)}{g(\xi)} + \sin(\phi)\cos(\phi)(1+t) - \frac{2g(\psi_{-t}(\xi))\psi_{-t}(\xi)}{g(\xi)(1+\psi_{-t}(\xi)^2)}\right). \tag{5.51}$$

These derivative equations in the pre-processed methods allow us to vastly reduce the required amount of numerically calculated derivatives which have been fraught with potential issues of large numerical error.

The calculation of the analytic formulas for $\left(\chi_t^{-1}\right)'$ and $\left(\chi_t^{-1}\right)''$ will improve the accuracy of the code but we still require the code to calculate ψ_{-t} numerically to be able to generate the modified inverse flow on the circle $\tilde{\chi}_t^{-1}$. If the data from the flow solver is poorly behaved this inaccuracy will obviously continue to be used throughout the code. One such area of difficulty is when Maple is looking outside of the support of the test function. Maple has difficulty identifying that (5.48) does not diverge due to the fact that the division of the test function g is at a point outside of its support. Analytically, $\left(\chi_t^{-1}\right)'$ and $\left(\chi_t^{-1}\right)''$ are well behaved over the whole range of the test function. In the areas of numerical difficulty these terms either tend to a constant or vanish completely. This means that the code requires extra logic to handle these regions sensibly and correctly.

The issues in using the analytic values are outweighed by the benefits. To rely only on numerical derivatives incurs problems in any case of rapid (perhaps erroneous) rates of change of the data. These problematic areas

need specific numerical assistance so moving to the analytic formulas for $\left(\chi_t^{-1}\right)'$ and $\left(\chi_t^{-1}\right)''$ where guidance is still needed is no problem. In the latter case of moving to analytic formulae however the erroneous points are minimised and one only needs to concern themselves with divergence.

In this chapter we have seen how pre-processing offers a method to improve the behaviour of the flow solutions being used to calculate the remainder of the welding problem. The pre-processing requires the user to choose the method of pre-processing to change the behaviour as is needed. We demonstrated how one would calculate derivatives of χ_t^{-1} analytically to help the numerical handing of the data. It was also discussed that these analytic formulae can incur issues when blindly used in numerical calculations. In most cases, these issues can be fixed by simply understanding why the numerical approach is failing and then substituting the correct limiting value instead.

— 6 —

Numerical verification of the completed welding code

We have developed a numerical method of welding which we have tested against analytic results given in [12]. Following this, we generated methods to improve the numerical implementation and in this chapter we use the welding method for two known analytic results which we can compare against in each case. We will then use the welding method for test functions which we have no data for.

We will first test the code against two test functions, a normalised Gaussian

$$g(u) = \frac{e^{-u^2}}{\sqrt{\pi}} \tag{6.1}$$

and Lorenztian (1.4) (setting $b = 1$ and $k = 1/\pi$ to normalise) to demonstrate the accuracy of the code.

The Gaussian test function will mean that the probability distribution is given by the shifted Gamma distribution (1.3) with parameters

- $\alpha = c/24$
- $\beta = \pi$
- $\sigma = \alpha/\beta$

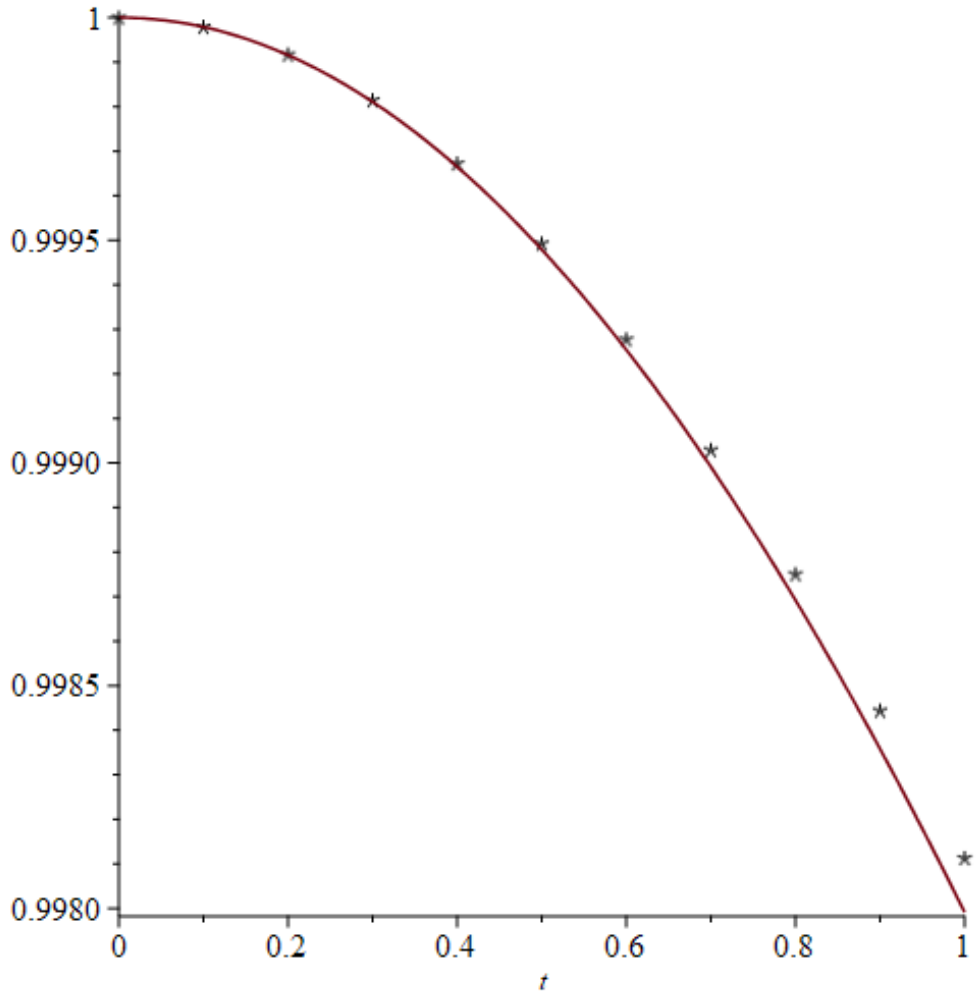

Figure 6.1: Comparison of the real part of the numerically computed welding data (points) and the shifted Gamma distribution (solid curve) (1.3) for a Gaussian test function. 750 angular points were used, 10 steps in t and $c = 1$.

and is compared to the numerically computed data from the welding code in Fig. 6.1.

For a more quantative comparison between the welding code and the analytic form, we have a plot of the percentage difference between the data points at concurrent steps in parameter t in Fig. 6.2 which highlights the

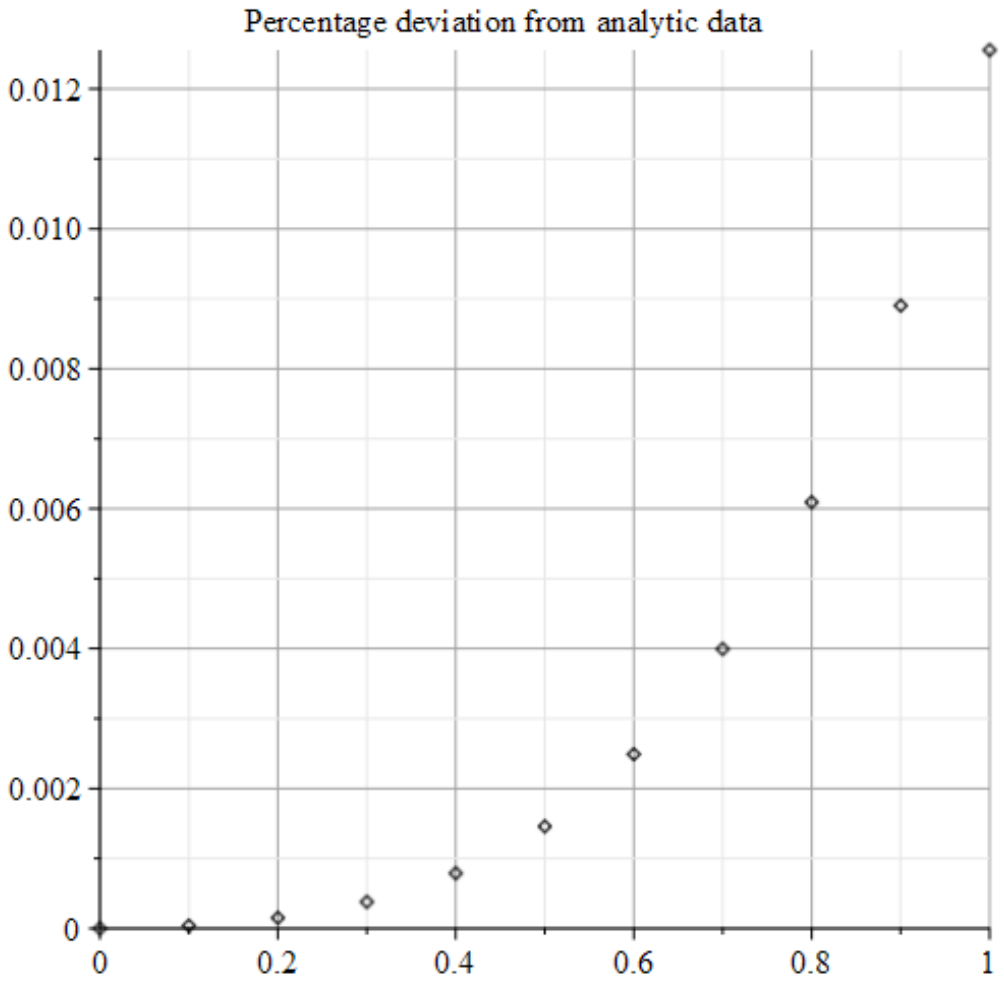

Figure 6.2: Plot demonstrating the percentage difference between the analytic and numerically calculated points in Fig. 6.1

prevailing features of the numerical welding method. The first of which is that it is possible to get excellent agreement with analytic data. The largest value of percentage deviation is equal to approximately 0.01316%. This agreement has been achieved using 750 angular grid points and 10 steps in the parameter t.

The other key feature demonstrated by Figs. 6.1, 6.2 is that the error increases rapidly as a function of t. This increase in error, as far as this

project has found, is unavoidable past a certain value of t. This value of t depends on the test function and ameliorating methods used within the code.

Looking now at the Lorentzian test function (1.4), we have the parameters

- $\alpha = c/72$
- $\beta = 4\pi/3$
- $\sigma = \alpha/\beta$

for use in the shifted Gamma distribution (1.3). Once more we use the welding code to compare against the analytic probability distribution and plot them against each other in Fig. 6.3 as another verification of the welding method.

Once more we see a deviation from the analytic values and produce another percentage deviation plot given in Fig. 6.4 to more quantitatively discuss them.

A comparison of the two plots given in Figures [6.2,6.4] demonstrates the consistent features of the numerical welding method. In both cases we observe good agreement between the analytic values and the numerically calculated data. More importantly the rate of increase of error highlights the fundamental problem of the welding method. This issue is that it can only be used and trusted to a certain value of the parameter t.

6.1 ANALYSIS OF THE GAUSSIAN AND LORENTZIAN TEST FUNCTION VIA THE WELDING METHOD

After completion of the generation of the welding code one item of great interest is the fact that all known test functions produced a shifted Gamma distribution for the probability distribution.

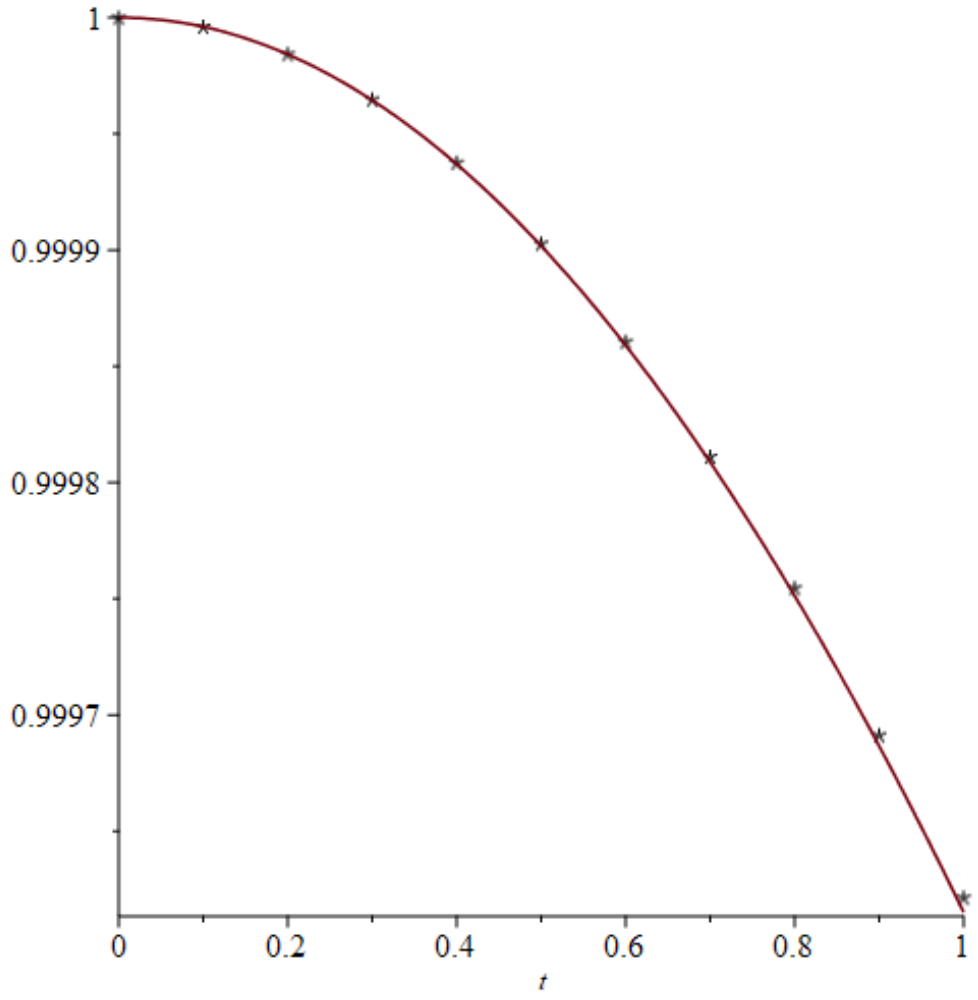

Figure 6.3: Comparison of the real part of the numerically computed welding data (points) and the shifted Gamma distribution (solid curve) (1.3) for a Lorentzian test function. 750 angular points were used, 10 steps in t and $c = 1$.

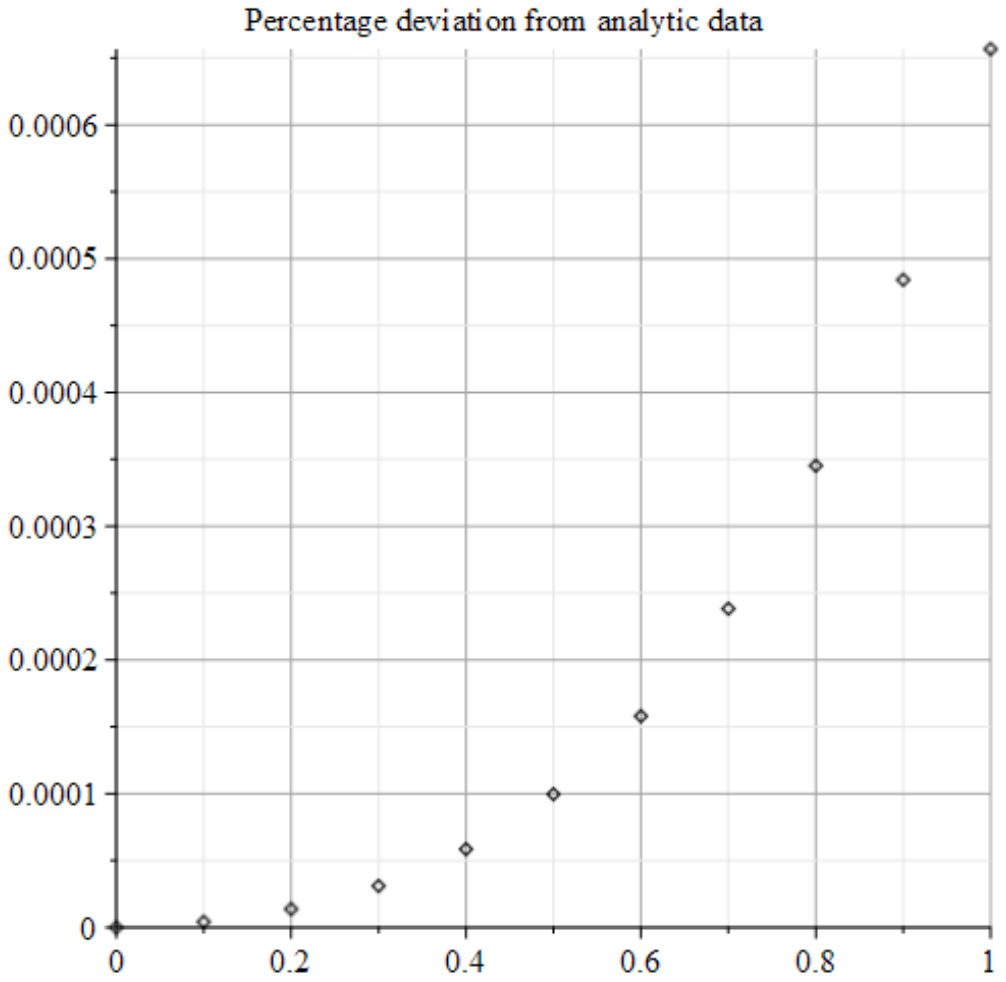

Figure 6.4: Plot demonstrating the percentage difference between the analytic and numerically calculated points in Fig. 6.3

Granted there were only a handful of infinite families of test functions that could, in closed-form, produce a solution to either the welding method or the moments method but the fact remained that the probability distribution for all known cases of positive test functions was described by a shifted Gamma distribution. We are interested in the behaviour of the probability distribution associated with using a test function which multiplies a Gaussian and Lorentzian function

$$f(u) = N\frac{e^{-u^2}}{1+u^2} \tag{6.2}$$

which we call the Gauss-Lorentz test function. We define N to ensure that $f(u)$ is normalised when integrated along the real line. The welding code was used to calculate the Fourier transform of the probability distribution associated with the Gauss-Lorentz test function. This calculation can be represented in the form of the complex plot given by Figure 6.5 and one can see the close agreement between the Fourier transform of the shifted Gamma distribution given by

$$\mathcal{F}(P)(\omega) = \left(1 - \frac{i\omega}{\beta}\right)^{-\alpha} e^{-i\omega\sigma} \tag{6.3}$$

closely related to (3.17).

The parameters α, β and σ are all related to the test function used. We are able to calculate σ due to it being the upper bound for the quantum energy inequality (1.16). The formula for calculating this quantum energy inequality bound is given by

$$\sigma = \frac{c}{12\pi}\int_{-\infty}^{\infty}\left(\frac{d}{du}\sqrt{f(u)}\right)^2 du, \tag{6.4}$$

with the differential of the square root of the test function defined as

$$\frac{d}{du}\sqrt{f(u)} = \begin{cases} f'(u)/2\sqrt{f(u)} & \text{if } f(u) \neq 0 \\ 0 & \text{if } f(u) = 0 \end{cases}. \tag{6.5}$$

We also choose $\alpha = c/24$ and β being given as the ratio of α and σ

$$\beta = \frac{\alpha}{\sigma}. \tag{6.6}$$

We can obtain α from c and β can be obtained from c and f. If we have chosen our test function we are able to use the quantum energy inequality bound (6.4) to at least numerically calculate σ to arbitrary precision.

Using these parameters we are able to compare the plots of the Fourier transformed probability distribution against the numerically calculated equivalent from the welding method to generate Fig. 6.5.

Clearly there is a good agreement between the curves which tells us that at least in a large part the Gauss-Lorentz test function obeys a shifted Gamma distribution. However, once more due to the fact that the distribution can only be numerically computed to an upper value of the parameter $t = 10$ it leaves the question as to whether we are in a regime of t to be able to identify the potential deviation of the Fourier transformed probability distribution from the shifted Gamma distribution with the expected parameters.

As t begins at 0 the plot begins at 1, corresponding to the total integral of the probability distribution being equal to 1. As t increases the spiral tends towards 0 which indicates a decaying transform. As the plot progresses the analytic shifted Gamma distribution deviates from the centre of the data points to the edge of the point markers. This means that the true curve is likely governed by something that looks a lot like the shifted Gamma it is plotted against but with another influence which we wish to better understand. If we were able to run the welding code to a higher value of t we would potentially be able to get a better understanding of how the probability distribution behaves when plotted against the shifted Gamma.

With the welding code as it is, one would not likely be able to generate data to a high enough value of t to fully understand the Fourier distribution generated by the Gauss-Lorentz test function. It is at this stage that we will proceed to analyse the Gauss-Lorentz test function using the method of moments. This analysis will enlighten us as to how the probability distribution behaves for both large and small t.

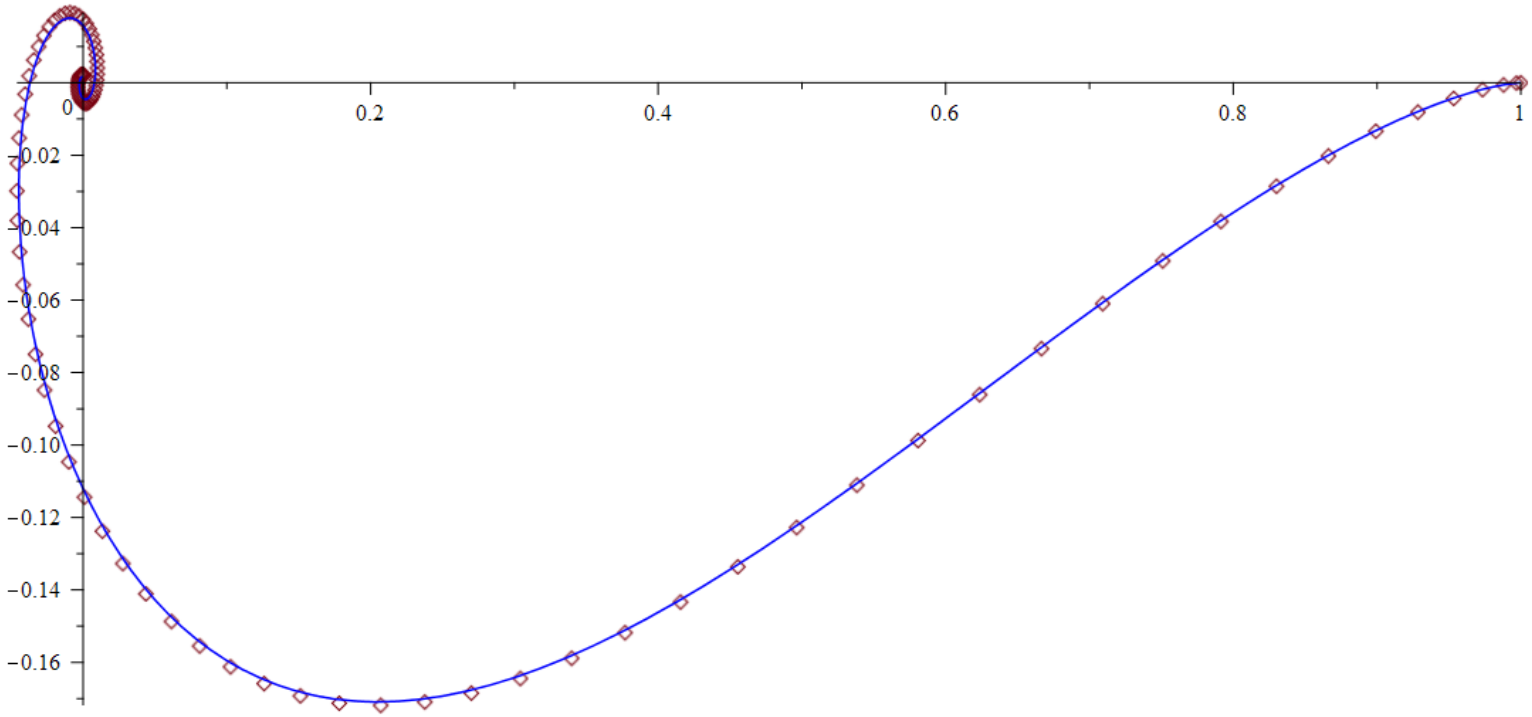

Figure 6.5: Complex plot comparing the probability distribution calculated from using a Gauss-Lorentz test function (6.2) via the welding method against the shifted Gamma distribution associated with a Gaussian test function. 1250 angular steps, 100 steps in t to a maximum of $t_{max} = 10$ and set $c = 120$.

6.2 USING THE WELDING CODE TO UNDERSTAND THE EFFECT OF A PLATEAU ON THE PROBABILITY DISTRIBUTION

Using the test function (5.39) we wish to understand the effect of varying switch on lengths and plateau lengths of the test function on the associated probability distribution. It is reasonable to ask whether the effect of changing the plateau length will have any effect on the probability distribution.

In the first instance this computation was performed using the pre-processing outlined in subsection 5.1.2. It was found however that due to the specific pre-processing used in this case that the plateau lengths needed to be of large values to avoid singular terms appearing in the calculations of $\left(\chi_t^{-1}\right)'$ and subsequent derivatives. Due to this, two plateau lengths were chosen, $\tau = 2000$ and $\tau = 200000$ which produced smooth and sensible data as can be seen in the complex plot comparison given by Fig. 6.6.

The extent of the match was at first encouraging, but it was found that due to the very large plateau lengths when the test function is mapped to the circle the two mapped plateaus would require a much higher mesh density to be able to differentiate between them. This means that the pre-processing used in this case did not turn out to be the correct one to use to improve the quality of data.

This was surprising following the success of the pre-processing method in the calculation of the Gauss-Lorentz case but we opted instead to remove the pre-processing portion of the code. The other improvements to the code were more than enough to return smooth data and a range of tests were conducted varying both plateau lengths and plateau switch on.

Immediately the improvement of the code was apparent. The code did not require large plateaus in order to produce smooth data and allowed us to analyse for small plateau values. This is demonstrated in Fig. 6.7 where the switch on time was held constant for 3 cases and only the plateau value

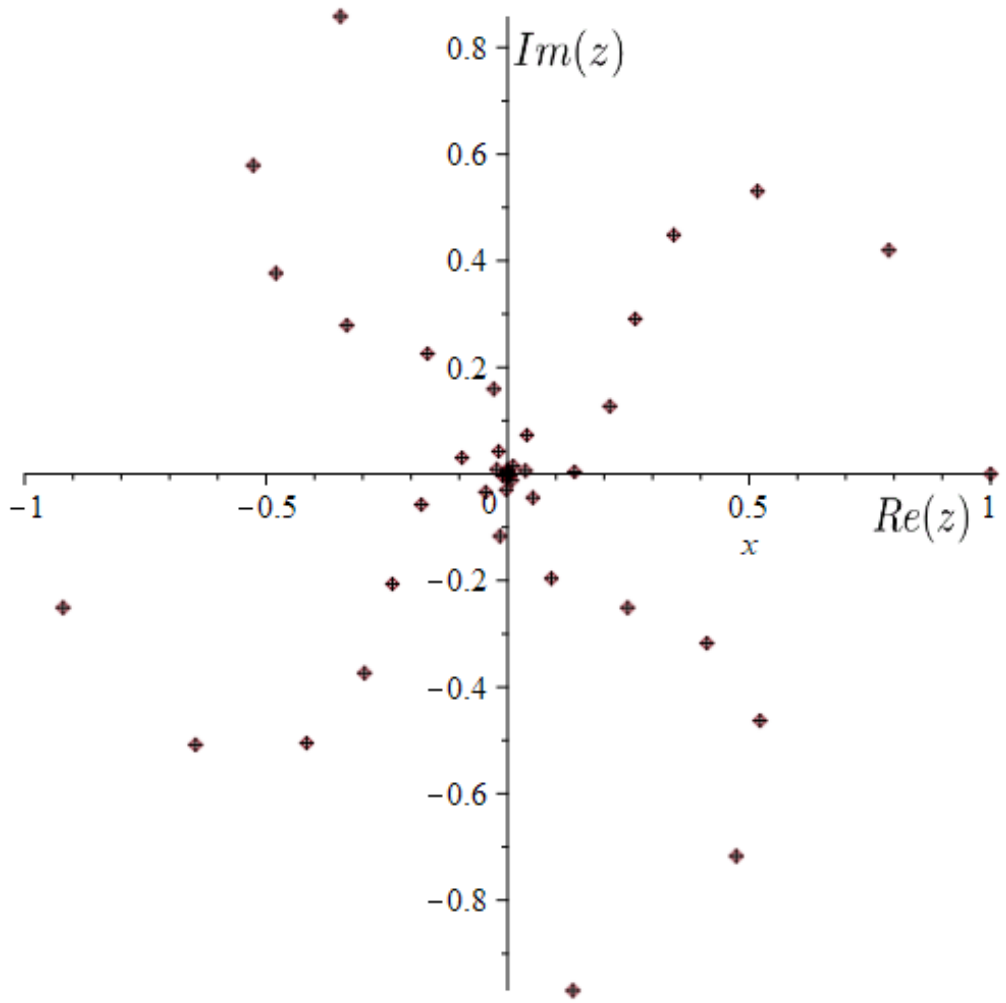

Figure 6.6: Complex plot comparing the Fourier transform of the probability distributions generated by using the test function (5.39) and the welding method to generate two Fourier transformed probability distributions one for a plateau length of 2000 (red) and one for a plateau length of 200000 (black). Both data sets used the pre-processing method for a central charge $c = 1$, 1250 angular steps and 100 steps in the diffeomorphism parameter t up to a maximum $t_{max} = 1$. The plot demonstrates both Fourier transforms begin at 1 and then decay, note that despite the plateau differences the match in position for the two sets of data.

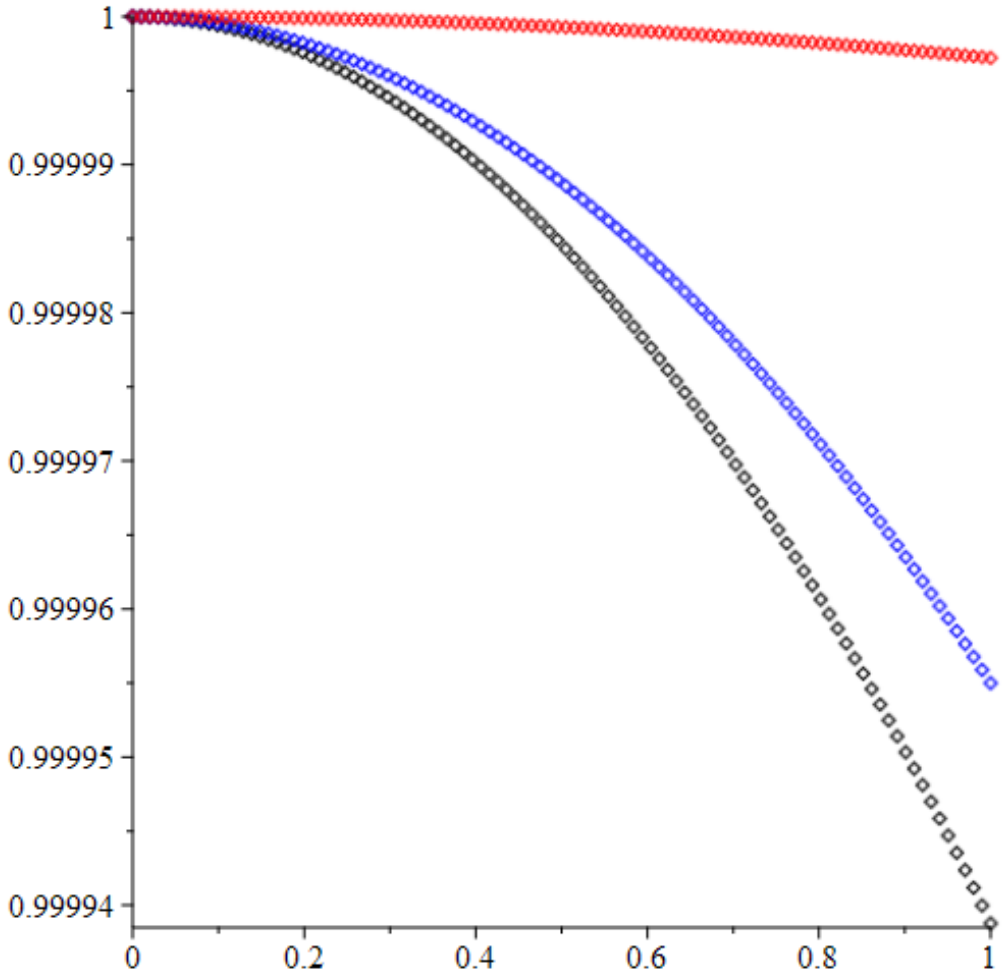

Figure 6.7: Plot of the real part of the Fourier transforms of the probability distributions calculated by the method of welding for plateau test functions of varying plateau lengths. Plateau length 1 is the black plot, 2 is the blue and 20 is the red. In each calculation, 1250 angular steps were used as well as 100 steps in t to $t_{max} = 1$ and $c = 1$

was changed. It demonstrates a clear dependence of the Fourier transform of the probability distribution to the plateau which implies that a shorter plateau creates a more spread out probability distribution when inverted back from Fourier space. It can also be seen that the larger the plateau the slower the decay in Fourier space which corresponds to a much more precise peak location when transformed into the probability.

An identical analysis was performed for the case of a variable switch on time and is shown in Fig. 6.8. Once more we can see a clear dependence of the Fourier distribution to the length of switch on time of the test function. The shorter the switch on time incurs a faster decay in Fourier space which corresponds to a wider peak in the probability distribution. The longer switch on times clearly decay far slower which means that the probability distribution is going to be have a more localised peak.

These novel results demonstrate that the variance in parameters in a plateau test function do affect the probability distribution of the energy density they are smeared against. It was unfortunate that in this case the pre-processing did not improve the data. This is not an admonishment of the method as it made a large difference in the case of the Gauss-Lorentz calculation. It highlights the vital importance in the specific choice of pre-processing.

We have seen how the welding code accurately matches the existing analytic results in the comparisons of the Gaussian and Lorentzian data sets. We understand that the welding code fundamentally cannot produce data to an arbitrary t.

Pre-processing as a method has demonstrated its strengths in calculating the probability distribution associated to a Gauss-Lorentz test function. Using it produced clear, well behaved data throughout the range and introduced the possibility of deviation from a shifted Gamma distribution.

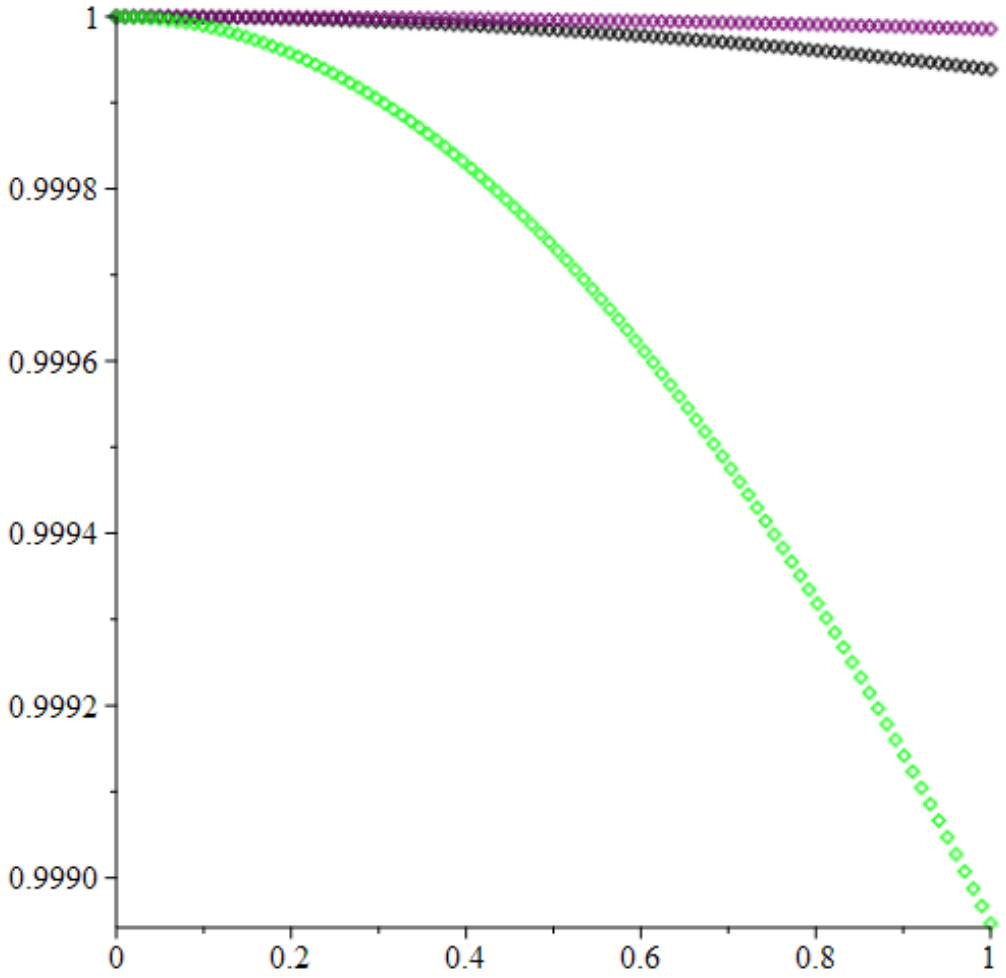

Figure 6.8: Plot of the real part of the Fourier transforms of the probability distributions calculated by the method of welding for plateau test functions of varying switch on and switch off lengths. The switch on lengths are 1 for the green curve, 2 for the black and 5 is the purple curve. In each calculation, 1250 angular steps were used as well as 100 steps in t to $t_{max} = 1$ and $c = 1$

It was also highlighted that the importance of choosing the correct method of pre-processing can severely limit the welding method as seen in the first calculation of the plateau associated probability distributions.

Lastly the other existing analytic aids to the numerical method of welding are sufficient on their own depending on the test function used. This was clearly seen in the comparisons of the plateau data after removal of pre-processing.

— 7 —

Analysis of the Gauss-Lorentz probability distribution using the method of moments

Using the method of moments we can glean information regarding the probability distribution resulting from a product of Gaussian and Lorentzian test functions. Following the potential deviation from shifted Gamma distribution which arose in the previous chapter, we wish to see if we can corroborate this using the method of moments.

The test function which acts as initial data for (3.7) is given by

$$f(u) = N\frac{e^{-u^2}}{1+u^2}, \tag{7.1}$$

normalised by N. We need to find the generalised test function to use with this method in terms of λ. In unpublished work by my supervisor (C. Fewster), this is done by making an ansatz $g_\lambda = f_{a(\lambda)}$ in (3.7). From this we are able to construct two simultaneous equations which we are able to use to generate an a dependent coefficient, denoted by $B(a)$, and a relationship between a and λ. By using computer algebra to extract equations for $B(a)$ and $a(\lambda)$, subject to $B(1) = \exp(-1/2)$ and $a(0) = 1$, it was found that these equations can be solved to obtain for the test function

$$f_a(u) = B(a)\frac{e^{-\frac{u^2}{2}}}{a^2+u^2} \tag{7.2}$$

where $B(a)$ is given by

$$B(a) = \frac{\sqrt{2}}{2}\left(ae^{-\frac{a^2}{2}}\sqrt{2} + \sqrt{\pi}\,(a-1)\,(a+1)\left(\mathrm{erf}\left(\frac{a\sqrt{2}}{2}\right) - 1\right)\right). \quad (7.3)$$

Taking the limit $a \to 1$ returns $B(1) = e^{-\frac{1}{2}}$ and reduces (7.2) to its simplest form. Notice that we have intentionally chosen a different subscript to (3.7). Understanding the coordinate relationship $\lambda \to a$ comes from one of the two simultaneous equations discussed in the context of calculating (7.3). We can draw a relationship between the two coordinates by understanding the effect of coordinate changing the differential equation (3.22). This gives a differential equation which allows us to infer the coordinate relationship given by

$$\lambda(a) = \frac{(-2\,a^2 + 2)\,\sqrt{\pi}}{\left(ae^{-\frac{a^2}{2}}\sqrt{2} + \sqrt{\pi}\,(a-1)\,(a+1)\left(\mathrm{erf}\left(\frac{a\sqrt{2}}{2}\right) - 1\right)\right)}, \quad (7.4)$$

and clearly, taking the limit $a \to 1$ returns $\lambda \to 0$ giving $g_0 = g$ as is needed to solve the flow equation for the method of moments. This coordinate relation is plotted in Fig 7.1 and demonstrates the key regions and behaviours important in this analysis. At $a \to 0^+$ we find $\lambda \to 2$ smoothly, as we increase a to approach the axis intersection at $a = 1$ we have $\lambda = 0$ which is the initial position we require to solve the flow equation (3.7). As a increases we see that $\lambda(a) \to -\infty$ rapidly in a.

This behaviour of (7.4) is most obviously seen if one takes series expansions about the points $a = 0$ and $a \to \infty$. In the case of $a = 0$, one finds the expansion

$$\lambda(a) \sim (2 - \frac{4\,\sqrt{2}}{3\,\sqrt{\pi}}a^3 - \frac{6\,\sqrt{2}}{5\,\sqrt{\pi}}a^5 + O\left(a^6\right)), \quad (7.5)$$

clearly demonstrating the smooth approach to $\lambda(a) \to 2$. If one does a similar analysis for the case $a \to \infty$ one has

$$\lambda(a) \sim \left(-\frac{\sqrt{\pi}\sqrt{2}a^3}{2} - \frac{\sqrt{\pi}\sqrt{2}a}{2} + O\left(a^{-1}\right)\right)\sqrt{e^{a^2}} \quad (7.6)$$

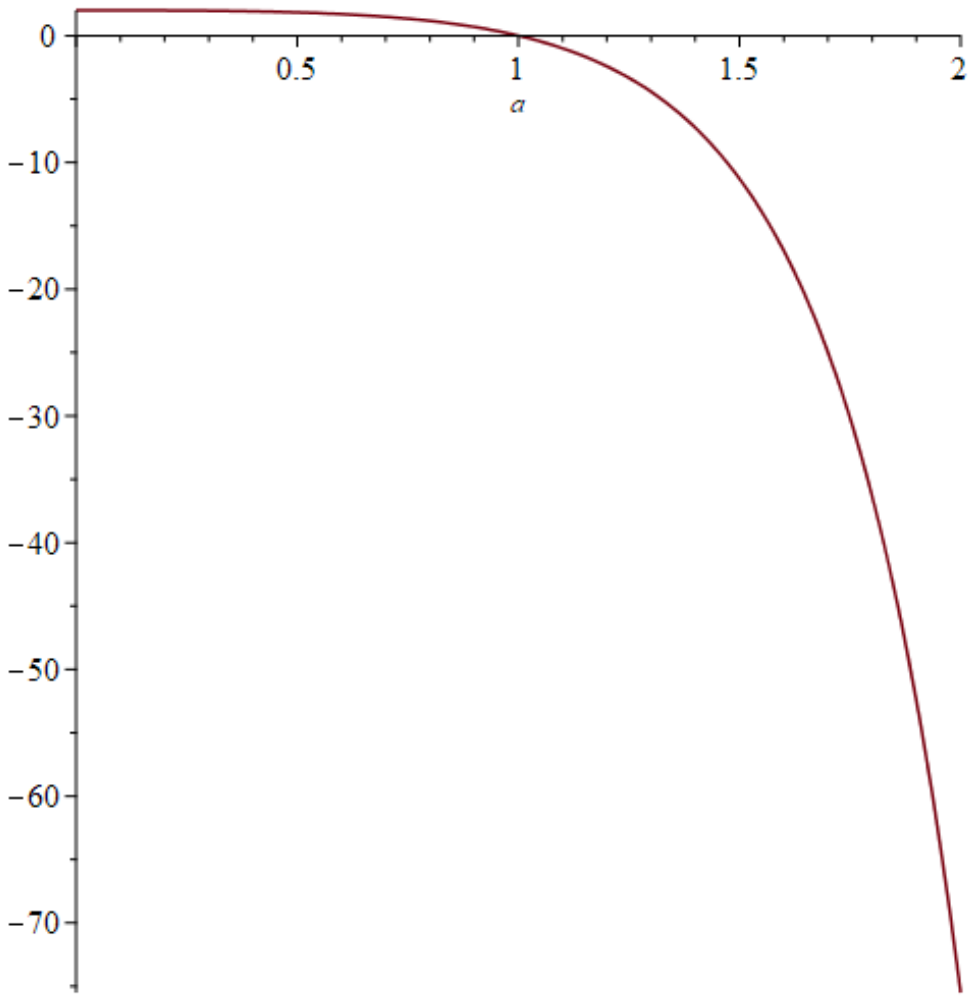

Figure 7.1: Plot of (7.4) for $a \in [0, 2]$.

which explains how the function grows in the large a limit.

Having found the correct general test function we can progress using the moments method (detailed in the example at the end of chapter 3) by calculating the Fourier transform of f_a to calculate the second moment (3.15) which we will denote by $\mathcal{G}_2(a)$.

Due to (7.2) being even in the Fourier transform variable we can instead calculate twice the cosine transform which via computer algebra gives us the following expression in k

$$\mathcal{G}_2(a) = \mathcal{Y}(a) \int_0^\infty k^3 \left(e^{ak} \operatorname{erfc}\left(\frac{a+k}{\sqrt{2}} \right) + e^{-ak} \operatorname{erfc}\left(\frac{a-k}{\sqrt{2}} \right) \right)^2 dk, \quad (7.7)$$

where the function $\mathcal{Y}$ is given by

$$\mathcal{Y}(a) = \frac{\left(a e^{-\frac{a^2}{2}} \sqrt{2} + \sqrt{\pi} \, (a-1) \, (a+1) \left(\operatorname{erf}\left(\frac{a\sqrt{2}}{2} \right) - 1 \right) \right)^2 e^{a^2}}{384 a^2}. \quad (7.8)$$

We wish to understand as much of the probability distribution analytically as possible, but we are unable to evaluate $\mathcal{G}_2(a)$ in closed form and follow the prescription to generate an analytic probability across the support of the distribution. Instead, we calculate asymptotic contributions of (7.7) for both $a \to 0$ and $a \to \infty$ which will correspond in λ to values near 2 and $\lambda \to -\infty$ as seen in Fig 7.1. The remainder of the range will be understood numerically which we will compare against asymptotic formulae describing these key regions in an attempt to corroborate the findings. Before proceeding we re-define our second moment into two formulae via

$$\mathcal{G}_2(a) = \mathcal{Y}(a) \mathcal{K}(a), \quad (7.9)$$

having grouped the integral term into $\mathcal{K}(a)$. We will use this formula to calculate separate asymptotic formulae for $\mathcal{Y}$ and $\mathcal{K}$ in the two regimes $a \to 0$ and $a \to \infty$. Before conducting the asymptotic analysis we will describe the numerical methods used to calculate the bulk contribution to the probability distribution.

7.1 NUMERICALLY IMPLEMENTING THE MOMENTS METHOD

Numerically implementing the moments method is rather simple in this case. Comparing it to the more general method of welding implementation is unfair. This is because we are only looking to understand the moments method in the case of the Gauss-Lorentz test function (7.2). The challenge of the moments method is finding a λ-dependent test function which solves (3.7). In the case of Gauss-Lorentz this has been done and $\mathcal{G}_2$ has been found as a function of a given by (7.7).

From (7.7) we wish to generate $\mathcal{G}_2(a(\lambda))$ which will require us to invert the coordinate relation (7.4). This is done numerically using the Python library "pynverse".

After calculating a numerically coordinate changed $\mathcal{G}_2(\lambda)$, we are able to then calculate W by numerically integrating $\mathcal{G}_2(\lambda)$ as described in (3.6). This integration is done using the inbuilt quadrature method of the "mpmath" Python library.

At this stage we can calculate M via (3.5) which returns the moment generating function. While performing this numerical implementation we noticed that near the singularity or for large negative values of λ the numerics were very poorly behaved. This demonstrates the importance of the asymptotic methods that we are going to develop.

From calculating M we need to invert the Laplace transform (3.16) to calculate the probability distribution and once more this is done numerically. We employ the "mpmath" inbuilt numerical Laplace transform opting to use the Gaver-Stehfest algorithm.

The Gaver-Stehfest algorithm [28] aims to approximate the Laplace

inversion f of the function F by a sequence of functions

$$f_n(x) = \log(2)x^{-1} \sum_{k=1}^{2n} a_k(n) F(k \log(2) x^{-1}), \tag{7.10}$$

requiring $n \geq 1$ and $x > 0$ and the coefficients $a(k)$ are given by

$$a_k(n) = \frac{(-1)^{n+k}}{n!} \sum_{j=(k+1)/2}^{\min(k,n)} j^{n+1} \binom{n}{j} \binom{2j}{j} \binom{j}{k-j}, \tag{7.11}$$

enforcing $1 \leq k \leq 2n$. The method requires high precision to avoid the coefficients growing too large and not being able to accurately control the approximation. After calculating the numerical Laplace inverse of M we have generated the approximation to the bulk values of the probability distribution. These values are used to compare against the asymptotics calculated in later subsections and generate a measure of the accuracy of the asymptotic series.

7.2 ASYMPTOTIC ANALYSIS OF THE SECOND MOMENT $a \to 0$ LIMIT

The calculation of the asymptotic series near zero or approaching infinity is simple in the case of $\mathcal{Y}$ and we are able to generate as many terms in the series as we would need. Using Maple this is given by

$$\mathcal{Y}(a) \sim \frac{\pi}{384a^2} - \frac{\pi}{384} + \frac{\sqrt{2\pi}}{288}a - \frac{\pi}{768}a^2 - \frac{\sqrt{2\pi}}{2880}a^3 + \mathcal{O}\left(a^4\right) \tag{7.12}$$

which clearly possesses a singularity as we approach $a \to 0$. Calculation of $\mathcal{K}$ is done as follows. We begin by splitting the function into $\mathcal{K}(a) = \mathcal{K}_1(a) + \mathcal{K}_2(a) + \mathcal{K}_3(a)$, where

- $\mathcal{K}_1(a) = \int_0^\infty k^3 e^{2ak} \operatorname{erfc}\left(\frac{a+k}{\sqrt{2}}\right)^2 dk$
- $\mathcal{K}_2(a) = \int_0^\infty k^3 e^{-2ak} \operatorname{erfc}\left(\frac{a-k}{\sqrt{2}}\right)^2 dk$
- $\mathcal{K}_3(a) = \int_0^\infty 2k^3 \operatorname{erfc}\left(\frac{a+k}{\sqrt{2}}\right) \operatorname{erfc}\left(\frac{a-k}{\sqrt{2}}\right) dk.$

We can perform a numerical analysis on these terms to determine which is going to contribute most to the singularity in $\mathcal{K}(a)$ near $a \to 0$. To

differentiate between asymptotic cases we introduce the notation $\mathcal{K}_0(a)$ to discuss $\mathcal{K}(a)$ in the small a limit and $\mathcal{K}_\infty(a)$ for large a. We find that $\mathcal{K}_{1,0}$ and $\mathcal{K}_{3,0}$ are both of order 1 but $\mathcal{K}_{2,0}$ diverges. With this foresight we begin our analysis of $\mathcal{K}_0$ by looking at $\mathcal{K}_{2,0}$ first using the identity $\operatorname{erfc}(x) = 2 - \operatorname{erfc}(-x)$

$$\int_0^\infty k^3 e^{-2ak} \operatorname{erfc}\left(\frac{a-k}{\sqrt{2}}\right)^2 dk = \int_0^\infty k^3 e^{-2ak} \left(2 - \operatorname{erfc}\left(\frac{k-a}{\sqrt{2}}\right)\right)^2 dk \quad (7.13)$$

and upon expanding the square and then separating terms we find

$$\begin{aligned} \mathcal{K}_{2,0}(a) = \int_0^\infty k^3 e^{-2ak} \operatorname{erfc}\left(\frac{a-k}{\sqrt{2}}\right)^2 dk = \int_0^\infty 4k^3 e^{-2ak} dk - \\ \int_0^\infty 4k^3 e^{-2ak} \operatorname{erfc}\left(\frac{k-a}{\sqrt{2}}\right) dk + \int_0^\infty k^3 e^{-2ak} \operatorname{erfc}\left(\frac{k-a}{\sqrt{2}}\right)^2 dk. \end{aligned} \quad (7.14)$$

The first and second terms can be integrated in closed form, but we keep the second represented as an integral for brevity, giving

$$\begin{aligned} \mathcal{K}_{2,0}(a) = \frac{3}{2a^4} - \int_0^\infty 4k^3 e^{-2ak} \operatorname{erfc}\left(\frac{k-a}{\sqrt{2}}\right) + \\ \int_0^\infty k^3 e^{-2ak} \operatorname{erfc}\left(\frac{k-a}{\sqrt{2}}\right)^2 dk. \end{aligned} \quad (7.15)$$

This shows a clear singularity at $a \to 0$ from the first term whereas the second and third term are both continuous as $a \to 0$. At this point we will regroup our $\mathcal{K}$, subtract off the singular term and then take the limit $a \to 0$ to find

$$\begin{aligned} \lim_{a\to 0^+} \left(\mathcal{K}_0(a) - \frac{3}{2a^4}\right) = \int_0^\infty k^3 \operatorname{erfc}\left(\frac{k}{\sqrt{2}}\right)^2 dk + \lim_{a\to 0^+} \left(\mathcal{K}_{2,0}(a) - \frac{3}{2a^4}\right) + \\ \int_0^\infty 2k^3 \operatorname{erfc}\left(\frac{k}{\sqrt{2}}\right) \operatorname{erfc}\left(\frac{-k}{\sqrt{2}}\right) dk. \end{aligned} \quad (7.16)$$

Upon substitution of $\mathcal{K}_2(a)$ and the use of the identity $\operatorname{erfc}(-x) = 2 - \operatorname{erfc}(x)$ once more we find

$$\begin{aligned}\lim_{a\to 0^+}\left(\mathcal{K}_0(a) - \frac{3}{2a^4}\right) = \int_0^\infty k^3 \operatorname{erfc}\left(\frac{k}{\sqrt{2}}\right)^2 dk - \int_0^\infty 4k^3 \operatorname{erfc}\left(\frac{k}{\sqrt{2}}\right) + \\ + \int_0^\infty k^3 \operatorname{erfc}\left(\frac{k}{\sqrt{2}}\right)^2 dk + \int_0^\infty 4k^3 \operatorname{erfc}\left(\frac{k}{\sqrt{2}}\right) dk \\ - \int_0^\infty 2k^3 \operatorname{erfc}\left(\frac{k}{\sqrt{2}}\right)^2 dk = 0.\end{aligned} \tag{7.17}$$

This demonstrates that we have removed all of the singular parts in $\mathcal{K}_0(a)$ and that there is no constant term. Now we proceed by differentiating under the integral and take another limit to calculate the subdominant contributions. This is the same as taking a Taylor series under the integral.

If we calculate this differential and take the appropriate limit using computer algebra in Maple we find

$$\left[\frac{d}{da}\left(\mathcal{K}_0(a) - \frac{3}{2a^4}\right)\right]\Bigg|_{a=0} = -\frac{16\sqrt{2}}{5\sqrt{\pi}} \tag{7.18}$$

and performing the same analysis at the second order gives

$$\left[\frac{d^2}{da^2}\left(\mathcal{K}_0(a) - \frac{3}{2a^4}\right)\right]\Bigg|_{a=0} = \frac{40}{3\pi} - 8, \tag{7.19}$$

allowing us to calculate

$$\mathcal{K}_0(a) \sim \frac{3}{2a^4} - \frac{16\sqrt{2}}{5\sqrt{\pi}}a + \frac{1}{2}\left(\frac{40}{3\pi} - 8\right)a^2 + \mathcal{O}(a^3). \tag{7.20}$$

This expansion combined with (7.12) generates

$$\begin{aligned}\mathcal{G}_{2,0}(a) \sim \frac{\pi}{256\,a^6} - \frac{\pi}{256\,a^4} + \frac{\sqrt{2}\sqrt{\pi}}{192\,a^3} - \\ \frac{\pi}{512\,a^2} - \frac{17\sqrt{2}\sqrt{\pi}}{1920\,a} - \frac{31\,\pi}{1536} + \frac{11}{288} + \mathcal{O}(a).\end{aligned} \tag{7.21}$$

7.2.1 Asymptotic analysis of the second moment in the $a \to \infty$ limit

Once more we begin with $\mathcal{Y}(a)$ (this time we denote with a subscript ∞) because Maple can generate as many terms in this expansion as we need. We find

$$\mathcal{Y}_\infty(a) \sim \frac{1}{48\,a^4} - \frac{1}{12\,a^6} + \frac{11}{24a^8} + O\left(a^{-10}\right) \tag{7.22}$$

clearly converging as a grows. We now look at $\mathcal{K}_\infty(a)$ for large a. First we will expand out the square

$$\mathcal{K}_\infty(a) = \int_0^\infty k^3 \left(e^{2ak}\,\mathrm{erfc}\left(\frac{a+k}{\sqrt{2}}\right)^2 + 2\,\mathrm{erfc}\left(\frac{a+k}{\sqrt{2}}\right)\mathrm{erfc}\left(\frac{a-k}{\sqrt{2}}\right) + \right.$$
$$\left. + e^{-2ak}\,\mathrm{erfc}\left(\frac{a-k}{\sqrt{2}}\right)^2 \right) dk \tag{7.23}$$

and remind ourselves of the asymptotic expansion of the complementary error function for large x

$$\mathrm{erfc}\,(x) \sim \frac{1}{e^{x^2}} \left(\frac{1}{\sqrt{\pi}x} - \frac{1}{2\sqrt{\pi}x^3} + \frac{3}{4\sqrt{\pi}x^5} - \frac{15}{8\sqrt{\pi}x^7} + O\left(x^{-9}\right) \right). \tag{7.24}$$

We consider the first four terms of this and using computer algebra we substitute this directly into (7.23). Upon substitution we perform another asymptotic expansion for large a and calculate the integrand $\mathcal{K}_{integrand}(a)$ of (7.23) to be

$$\mathcal{K}_{integrand}(a) \sim \frac{1}{e^{a^2}} \left(8\,\frac{e^{-k^2}k^3}{\pi\,a^2} + 8\,\frac{(2\,k^2-2)\,k^3e^{-k^2}}{\pi\,a^4} \right.$$
$$+8\,\frac{(3\,k^4-14\,k^2+7)\,k^3e^{-k^2}}{\pi\,a^6} \tag{7.25}$$
$$\left. +8\,\frac{(4\,k^6-44\,k^4+108\,k^2-36)\,k^3e^{-k^2}}{\pi\,a^8} + O\left(a^{-10}\right) \right).$$

We integrate (7.25) to calculate (7.23) using computer algebra and find

$$\mathcal{K}_\infty(a) \sim \frac{1}{e^{a^2}} \left(4\,\frac{1}{\pi\,a^2} + 8\,\frac{1}{\pi\,a^4} - 12\,\frac{1}{\pi\,a^6} + 48\,\frac{1}{\pi\,a^8} \right) + \mathcal{O}(e^{-a^2}/a^{10}). \tag{7.26}$$

We then combine (7.22) and (7.26) to find

$$\mathcal{G}_{2,\infty}(a) \sim \left(\frac{1}{12a^6} - \frac{1}{6a^8} + \frac{11}{12\pi a^{10}}\right) e^{-a^2} + \mathcal{O}\left(\frac{e^{-a^2}}{a^{12}}\right). \tag{7.27}$$

We test this formula against the numerically calculated equivalent in Fig. 7.2 and can see that the asymptotics quickly approach high levels of agreement as we increase a. We require (7.27) to be accurate as $a \to \infty$ and as is demonstrated in Fig. 7.2 this condition is fulfilled to a good degree for values of a of order 10 and larger.

7.2.2 Asymptotic calculation of the coordinate inverted second moments

7.2.2.1 CALCULATION IN THE $\lambda \to 2$ LIMIT We have $\mathcal{G}_2(a)$ as a function of a in both asymptotic regimes. In this section we will transform our second moment into the related coordinate λ and then calculate the connected moment generating function from this. When we have the connected moment generating function W as in (3.18), we can then attempt to perform a Laplace inversion to generate an asymptotic approximation of the probability density function in the large t regime.

The coordinate relationship between a and λ is given by

$$\lambda(a) = \frac{(-2\,a^2 + 2)\,\sqrt{\pi}}{\left(ae^{-\frac{a^2}{2}}\sqrt{2} + \sqrt{\pi}\,(a-1)\,(a+1)\left(\operatorname{erf}\left(\frac{a\sqrt{2}}{2}\right) - 1\right)\right)} \tag{7.28}$$

and from this formula one can predict that asymptotic inversion of this coordinate relationship is non-trivial. Due to this fact generating an inverse relationship between λ and a must be done in their specific asymptotic regimes.

7.3 THE SECOND MOMENT IN A SMALL a REGIME

Calculation of the small a asymptotics of our second moment gives the following series

$$\mathcal{G}_2(a) \sim \frac{\pi}{256\,a^6} - \frac{\pi}{256\,a^4} + \frac{\sqrt{2\pi}}{192\,a^3} - \frac{\pi}{512\,a^2} + \mathcal{O}(a^{-1}). \tag{7.29}$$

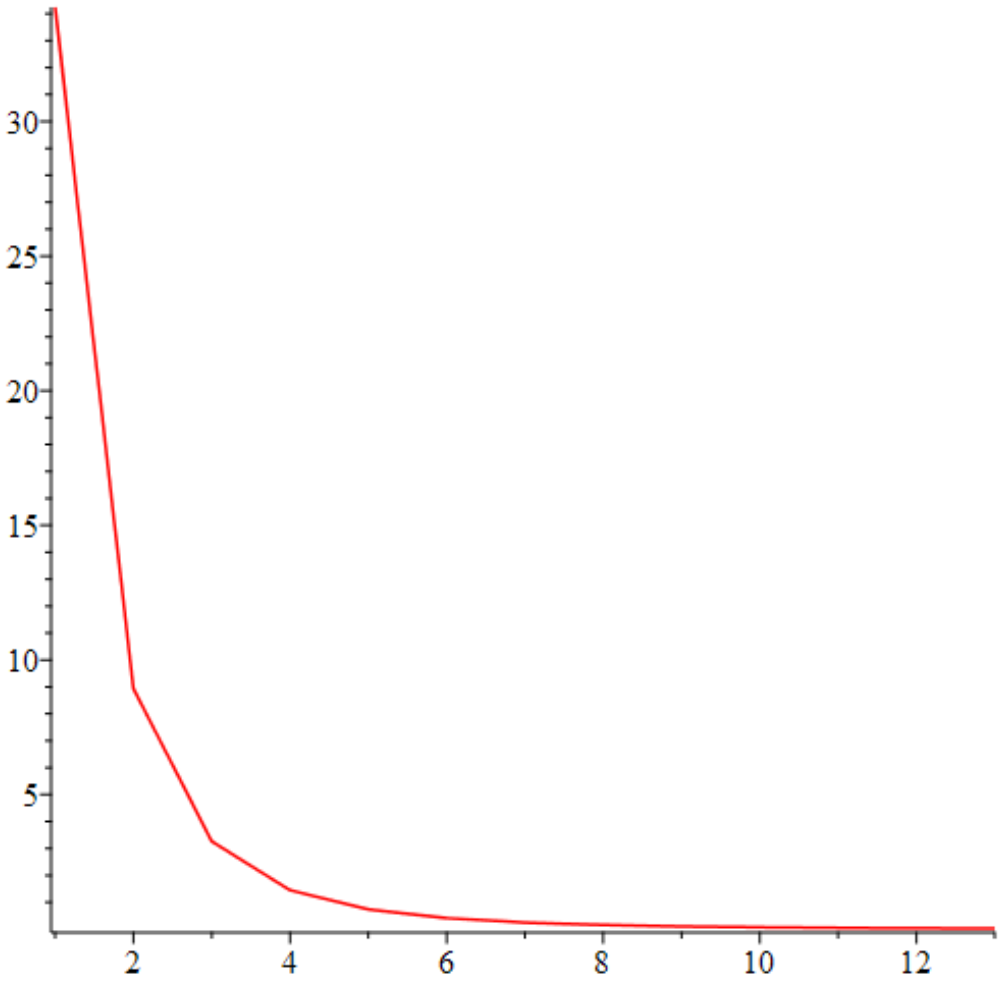

Figure 7.2: Percentage difference between the second moment asymptotics (7.27) and the numerical data in a for $a \in (1, 13)$

The first approach of calculating $\mathcal{G}_2(a(\lambda))$ was using successive asymptotic approximations in the relevant regime for a. This was cumbersome, so instead we opt for a method which matches the constants associated with the power series in a.

If one makes the educated guess that the dominant singular term in $\mathcal{G}_2(a(\lambda))$ is proportional to $1/(2-\lambda)^2$, we then take the series as a approaches 0 to check how well the expansion matches (7.29) and find

$$\frac{1}{72(2-\lambda(a))^2} \sim \frac{\pi}{256\,a^6} - \frac{9\,\pi}{1280\,a^4} + \frac{\sqrt{\pi}\sqrt{2}}{192\,a^3} + \frac{213\,\pi}{89600\,a^2} + \mathcal{O}(a^{-1}). \quad (7.30)$$

Clearly this is the correct leading term in our expansion but we wish to correct the subleading terms as well and so using the correction of $1/(2-\lambda)^{\frac{4}{3}}$ with appropriate constants we find

$$\frac{1}{72\,(2-\lambda\,(a))^2} + \frac{\sqrt[3]{18\pi}}{360\,(2-\lambda\,(a))^{\frac{4}{3}}} \sim \frac{\pi}{256\,a^6} - \frac{\pi}{256\,a^4} + \frac{\sqrt{2\pi}}{192\,a^3} - \frac{123\,\pi}{89600\,a^2} + \mathcal{O}(a^{-1}), \quad (7.31)$$

giving agreement in the first 3 singular terms of (7.29). We will get one further term to improve the accuracy when implemented into numerical calculations. Therefore we will perform this once more and we find that our second moment in λ is asymptotically given by

$$\mathcal{G}_2(\lambda) \sim \frac{1}{72\,(2-\lambda)^2} + \frac{(18\pi)^{1/3}}{360\,(2-\lambda)^{\frac{4}{3}}} - \frac{13\,\pi^{2/3}2^{2/3}3^{1/3}}{33600\,(2-\lambda)^{\frac{2}{3}}}. \quad (7.32)$$

We are able to make this brute force coordinate matching method more systematic by using computer algebra in Maple. If we are to take $a \to 0$ the corresponding limit is to take $\lambda \to 2$. We calculate the series of $\lambda(a)$ for small a and find

$$\lambda(a) \sim 2 - \frac{4\,\sqrt{2}a^3}{3\,\sqrt{\pi}} - \frac{6\,\sqrt{2}a^5}{5\,\sqrt{\pi}} + \frac{16\,a^6}{9\,\pi} - \frac{17\,\sqrt{2}a^7}{14\,\sqrt{\pi}} + \frac{16\,a^8}{5\,\pi} + \mathcal{O}(a^9). \quad (7.33)$$

We use recursion with the first order contribution being given by

$$a(\lambda) \sim \left(\frac{3\sqrt{\pi}(2-\lambda)}{4\sqrt{2}}\right)^{\frac{1}{3}}, \quad (7.34)$$

choosing the positive root as we require $a > 0$. Upon several recursions we generate the series

$$\begin{aligned} a(\lambda) \sim \frac{\sqrt[3]{3}\sqrt[3]{\sqrt{2}\sqrt{\pi}}}{2}\sqrt[3]{2-\lambda} - \frac{9\sqrt{2}\sqrt{\pi}\,(2-\lambda)}{80} + \frac{\sqrt[3]{3}\sqrt[6]{2}\sqrt[6]{\pi}}{12}(2-\lambda)^{\frac{4}{3}} \\ + \frac{237\,\pi^{5/6}3^{2/3}2^{5/6}}{44800}(2-\lambda)^{\frac{5}{3}} \\ - \frac{9\sqrt{2}\sqrt{\pi}\,(2-\lambda)^2}{160} + \frac{\sqrt[6]{\pi}\,(5097\,\pi+44800)\,\sqrt[3]{3}\sqrt[6]{2}}{1612800}(2-\lambda)^{\frac{7}{3}} + O\left((2-\lambda)^{\frac{8}{3}}\right) \end{aligned} \tag{7.35}$$

which we substitute into (7.21) and then expand in powers of $(2-\lambda)$. This substitution will generate singular terms and then non-singular terms. We may split $\mathcal{G}_2(\lambda)$ into singular and integrable parts

$$\mathcal{G}_2(\lambda) = \mathcal{G}_2^{sing}(\lambda) + \bar{\mathcal{G}}_2(\lambda). \tag{7.36}$$

The singularities are all contained within $\mathcal{G}_2^{sing}(\lambda)$ so when we substitute (7.35) into (7.21) we will have a lengthy expression which we can simplify by taking only the singular part and then group the rest into $\bar{\mathcal{G}}_2$

$$\mathcal{G}_2^{sing}(\lambda) \sim \frac{1}{72\,(2-\lambda)^2} + \frac{(18\pi)^{\frac{1}{3}}}{360\,(2-\lambda)^{\frac{4}{3}}} + \mathcal{O}\left((2-\lambda)^{-2/3}\right). \tag{7.37}$$

Clearly agreeing to the results obtained using the method of matching constants. The benefit of the brute force method is that provided the expansion is simple, one is able to guess and then verify the power law of the λ contributions. However it could be challenging to be able to produce the subleading terms in λ that would generate the correct powers in a.

We compare this calculation of the second moment in this regime to the numerically calculated equivalent to gauge how well the asymptotic expansion matches the data produced from the code. Clearly Fig. 7.3 demonstrates that the approximation begins poorly but quickly approaches a percentage difference below 1% as we approach the relevant limit in λ.

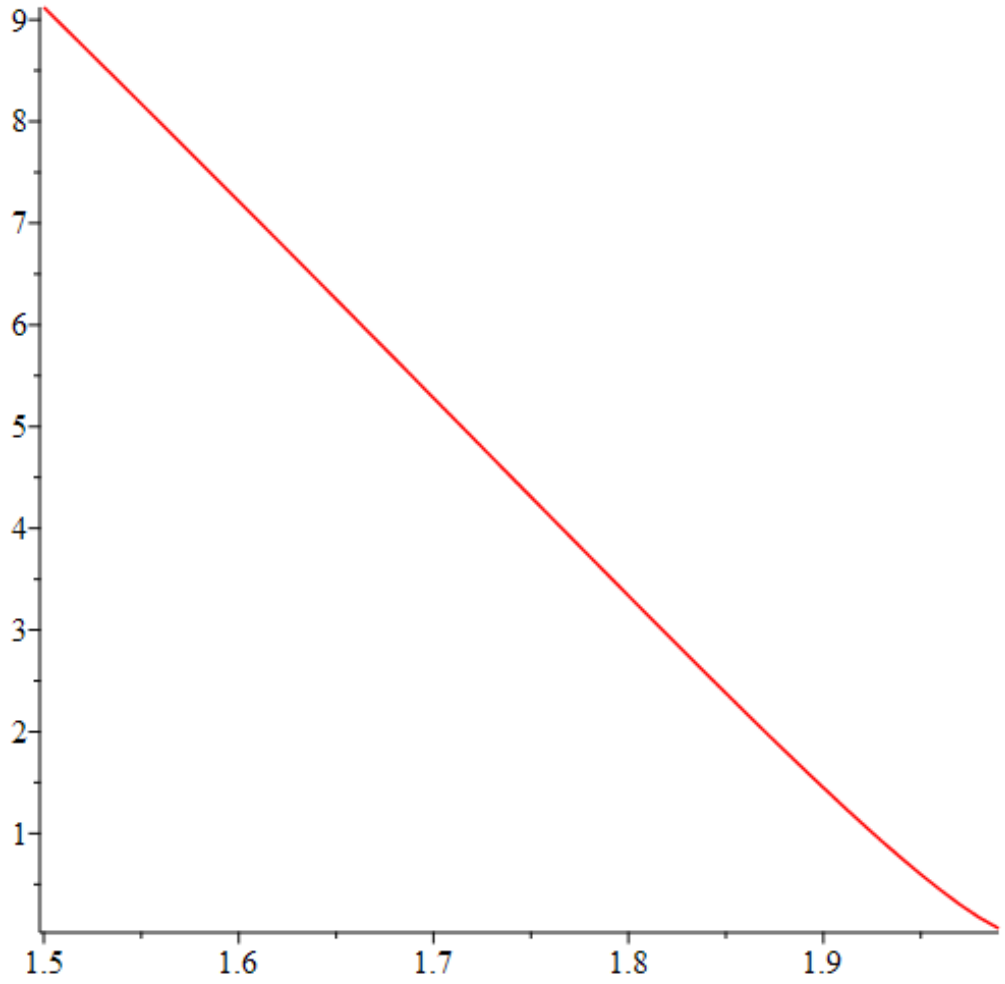

Figure 7.3: Percentage difference between the second moment asymptotics (7.37) and the numerical data for $\lambda \in (1.5, 1.99)$.

7.3.1 The second moment in a large a regime

Similarly to the small a regime, for the large a regime we begin with $1/\lambda(a)^2$

$$\frac{1}{\lambda(a)^2} \sim \frac{2}{\pi a^6} e^{-a^2} + \mathcal{O}\left(\frac{e^{-a^2}}{a^8}\right) \tag{7.38}$$

and notice once more that the dominant term of our expansion in this region of $\lambda(a)$ will be dominated by $1/\lambda(a)^2$. By enforcing the agreement of the dominant term in (7.27) by simply dividing by 24 and exchanging our square of λ to concur with the asymptotics for $a \to 0$ we find

$$\frac{1}{24(2-\lambda(a))^2} \sim \left(\frac{1}{12\pi a^6} - \frac{1}{6\pi a^8} + \frac{17}{12\pi a^{10}}\right) e^{-a^2} + \mathcal{O}\left(\frac{e^{-a^2}}{a^{12}}\right). \tag{7.39}$$

Somewhat remarkably, simply by enforcing that the constants match on the initial term of (7.27), the second term agrees perfectly as well.

Other analysis suggested that the subsequent term contained a factor proportional to $1/((2-\lambda(a))^2 \log{(2-\lambda(a))^2})$. By generating an asymptotic series for this term as $a \to \infty$ one finds

$$\frac{1}{(2-\lambda(a))^2 \log{(2-\lambda(a))^2}} \sim \frac{8}{\pi a^{10}} e^{-a^2} + \mathcal{O}\left(\frac{e^{-a^2}}{a^{12}}\right). \tag{7.40}$$

Due to the fact that the lowest order contribution from (7.40) in a is unrelated completely to the lowest order terms in (7.27), we can subtract the logarithmic term after correcting the constant to generate

$$\begin{aligned} &\frac{1}{24(2-\lambda)^2} - \frac{1}{16(2-\lambda(a))^2 \log{(2-\lambda(a))^2}} \sim \\ &\left(\frac{1}{12\pi a^6} - \frac{1}{6\pi a^8} + \frac{11}{12\pi a^{10}}\right) e^{-a^2} + \mathcal{O}\left(\frac{e^{-a^2}}{a^{12}}\right), \end{aligned} \tag{7.41}$$

giving exactly the correct expansion up to the relevant order.

From this brute force manipulation of the λ terms we have found the second moment in the λ coordinate for the large a limit which corresponds to the large negative λ limit

$$\mathcal{G}_2(\lambda) \sim \frac{1}{24(2-\lambda)^2} - \frac{1}{16(2-\lambda)^2 \log{(2-\lambda)^2}} + \mathcal{O}\left(\frac{1}{\lambda^2 \log{(\lambda)^3}}\right). \tag{7.42}$$

7.4 CALCULATION OF THE CONNECTED MOMENT GENERATING FUNCTION

After calculating $\mathcal{G}_2(\lambda(a))$ in their relevant asymptotic regimes, (7.37), (7.42) we are able to now begin the calculation of the connected moment generating function. This will allow us to calculate asymptotic information about the Laplace transform of the probability distribution.

The method for calculating the connected moment generating function in both cases is similar. We have previously separated the second moments calculated into their singular regions as well as the non-singular parts.

This method of separation into singular and non-singular contributions from the second moment means that we are able to control and understand the singular behaviour and then numerically calculate the remainder.

We begin with the connected moment generating function

$$W(\mu) = \int_0^\mu (\mu - \lambda)\, \mathcal{G}_2(\lambda) d\lambda \tag{7.43}$$

and split our second moment into the singular and sub-leading terms

$$\mathcal{G}_2(\lambda) = \mathcal{G}_2^{sing}(\lambda) + \bar{\mathcal{G}}_2(\lambda). \tag{7.44}$$

This is then substituted into (7.43)

$$W(\mu) = \int_0^\mu (\mu - \lambda)\, \mathcal{G}_2^{sing}(\lambda) + \int_0^\mu (\mu - \lambda) \bar{\mathcal{G}}_2(\lambda) d\lambda \tag{7.45}$$

and we have generated $W(\mu)$ which will be in part resolved analytically where possible. The remaining parts of $W(\mu)$ are resolved numerically and will be a potential source of error.

7.4.1 Resolution of the connected moment generating function in the $\lambda \to 2$ limit

With the general framework outlined, we find that substitution of the leading terms from (7.37) into (7.45) gives

$$W(\mu) = \int_0^\mu (\mu - \lambda) \left(\frac{1}{72(2-\lambda)^2} + \frac{(18\pi)^{\frac{1}{3}}}{360(2-\lambda)^{\frac{4}{3}}} \right) d\lambda + \int_0^\mu (\mu - \lambda) \bar{\mathcal{G}}_2(\lambda) d\lambda. \tag{7.46}$$

At this point we will separate out the integral for the barred term and find

$$W(\mu) = \int_0^\mu (\mu - \lambda) \left(\frac{1}{72(2-\lambda)^2} + \frac{(18\pi)^{\frac{1}{3}}}{360(2-\lambda)^{\frac{4}{3}}} \right) d\lambda + \int_0^2 (\mu - \lambda)\, \bar{\mathcal{G}}_2(\lambda) d\lambda - \int_\mu^2 (\mu - \lambda)\, \bar{\mathcal{G}}_2(\lambda) d\lambda + \mathcal{O}\left((2-\lambda)^{\frac{4}{3}} \right). \tag{7.47}$$

One should note that the $\mathcal{O}\left((2-\lambda)^{-2/3}\right)$ terms from (7.37) have been grouped into the barred term. The error term in (7.47) is found because the most singular part of $\bar{\mathcal{G}}_2$ is given by $(2-\lambda)^{-2/3}$ and is multiplied in the integral by a linear contribution proportional to λ.

By separating the subdominant integral we are able to resolve the second additive term fully in all cases. Provided we are performing analysis in the region $\mu \to 2$, the third term will tend to zero.

Computation of the first term can be done analytically and then the subdominant terms are computed numerically, one linear in μ and one constant. Combining terms we find

$$W_2(\mu) \sim -\sigma_2 \mu + K_2 + \frac{1}{72} \log\left(\frac{2}{2-\mu} \right) - \frac{(18\pi)^{\frac{1}{3}} (2-\mu)^{\frac{2}{3}}}{80} + \mathcal{O}\left((2-\mu)^{\frac{4}{3}} \right) \tag{7.48}$$

where the two constants σ_2 and K_2 are calculated numerically and are given by

- $\sigma_2 \approx 0.04794083416$
- $K_2 \approx 0.10032095454$

to the numercial accuracy employed.

To verify the accuracy of the connected moment generating function in this limit we compare our expansion to the numerically calculated equivalent. We can see in Fig. 7.4 the percentage difference between the two values which demonstrates that approaching the limit $\mu \to 2$ the difference is shrinking.

One would be justified to ask why we wish to calculate the asymptotics of the connected moment generating function if we are going to simply calculate a large part of the distribution numerically. The answer to this is that while in the bulk of the range, the numerical calculation is stable. The code is unable to control the large values of $W(\mu)$ as $\mu \to 2$ and is unable to symbolically investigate the large negative independent variable as it approaches infinity.

As one can see from Fig. 7.4 the asymptotic approximation begins fairly poorly being almost 30% away from the numerically calculated value at $\mu = 1.5$ but it tends towards the percentage value of 0 as the independent variable approaches 2. To ensure viability of the approximation, the same analysis is performed closer to the region of validity and generates the plot Fig. 7.5.

Clearly as we enter into a region past $\mu = 1.99$ the approximation becomes far better. A percentage error of far less than one percent and still decreasing as the variable approaches 2 means that this asymptotic expansion can be used with confidence provided that μ is in a small region near 2.

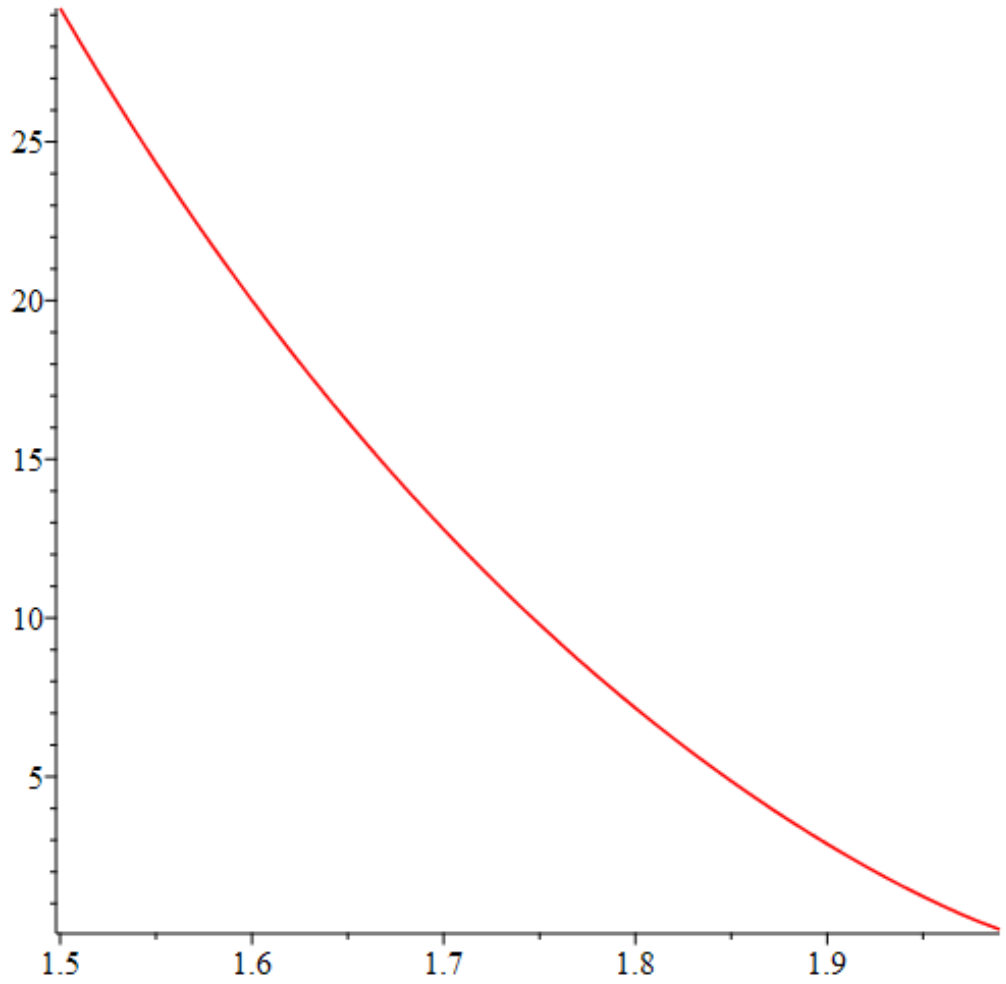

Figure 7.4: Percentage difference between the asymptotic expansion (7.48) and the numerically calculated value of W in the $\mu \to 2$ regime for $\mu \in (1.5, 1.99)$.

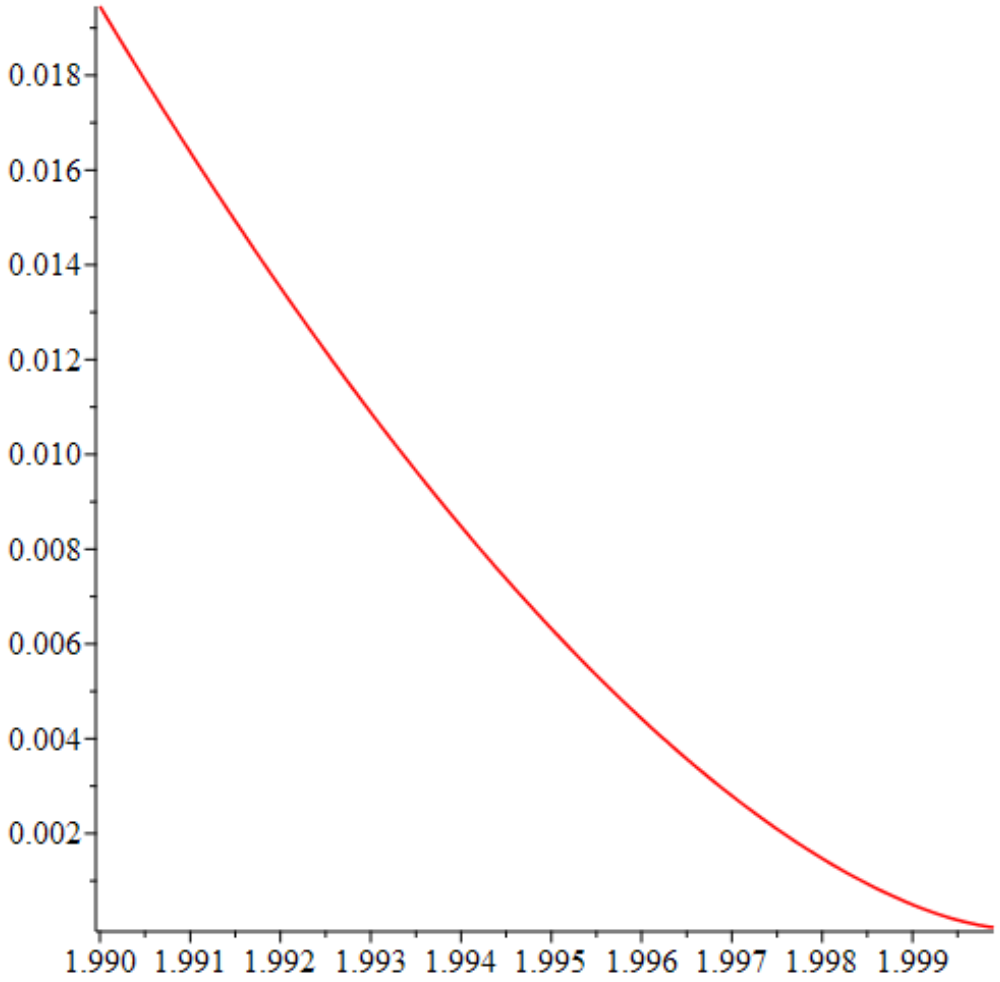

Figure 7.5: Percentage difference between the asymptotic expansion (7.48) and the numerically calculated value of W in the $\mu \to 2$ regime for $\mu \in (1.99, 1.9999)$.

7.4.2 Resolution of the connected moment generating function in the $\lambda \to -\infty$ limit

Calculation of the connected moment generating function is done in a similar way for the $\lambda \to -\infty$ as in the case $\lambda \to 2$. We begin by separating once more the second moment into its dominant and subdominant parts. When this is done we generate an integral that can be resolved numerically and another which converges to zero as $\lambda \to -\infty$

$$W(\mu) = \int_0^\mu (\mu - \lambda) \left(\mathcal{G}_2(\lambda) - \frac{1}{24(2-\lambda)^2} \right) d\lambda + \int_0^\mu (\mu - \lambda) \frac{1}{24(2-\lambda)^2} d\lambda. \tag{7.49}$$

The sub-leading singular term in this is calculated numerically, analogously to the case of $\lambda \to 2$ and once more we are able to calculate a term linear in μ and another which is just a constant.

Substituting our integrand into the singular contribution of the second moment, we find

$$W(\mu) = \frac{1}{24} \log \left(\frac{2}{2-\mu} \right) - \frac{\mu}{48} + \int_{-\infty}^\mu (\mu - \lambda) \left(\mathcal{G}_2 - \frac{1}{24(2-\lambda)^2} \right) d\lambda - \int_{-\infty}^0 (\mu - \lambda) \left(\mathcal{G}_2 - \frac{1}{24(2-\lambda)^2} \right) d\lambda. \tag{7.50}$$

Once more the first term in the first integral is calculated from $1/\lambda^2$ and generates the logarithmic term as in the other limiting case.

Calculation of the second integral gives the connected moment generating function

$$W(\mu) \sim \frac{1}{24} \log \left(\frac{2}{2-\mu} \right) - \frac{\mu}{48} + \frac{(\mu - 2)\,\mathrm{Ei}\,(1, \ln(2-\mu))}{16} - D\mu + C \tag{7.51}$$

with constants D and C given by

- $D = 0.035222497541$

- $C = -0.03324548778$

and

$$\mathrm{Ei}\,(a, z) = z^{a-1}\Gamma(1 - a, z). \tag{7.52}$$

The exponential integral term can be asymptotically represented in the regime $\mu \to -\infty$ giving a more comparable expansion to the case $\mu \to 2$

$$\begin{aligned} W(\mu) \sim -\sigma_\infty \mu + K_\infty + \frac{1}{24}\log\left(\frac{2}{2-\mu}\right) - \frac{1}{16\log(2-\mu)} + \\ \mathcal{O}\left(\int_0^\mu \frac{1}{16(2-\lambda)\log(2-\lambda)^2} d\lambda\right), \end{aligned} \tag{7.53}$$

with the constants σ_∞ and K_∞ given by

- $\sigma_\infty = 0.05605583087$
- $K_\infty = -0.03324548783$.

7.5 CALCULATION OF THE MOMENT GENERATING FUNCTION

Recall that the moment generating function M is related to the connected moment generating function W by $M = \exp(W)$.

This is done in both asymptotic cases to allow us to then move onto calculation of the probability distribution contributions from each end of the distributions.

For comparison, recall that the connected moment generating function for a shifted Gamma distribution is

$$W(\mu) = \alpha \log\left(\frac{\beta}{\beta - \mu}\right) - \sigma\mu \tag{7.54}$$

and then upon exponentiation to calculate the moment generating function one finds

$$M(\mu) = \frac{e^{-\mu\sigma}}{(1 - \mu/\beta)^\alpha} \tag{7.55}$$

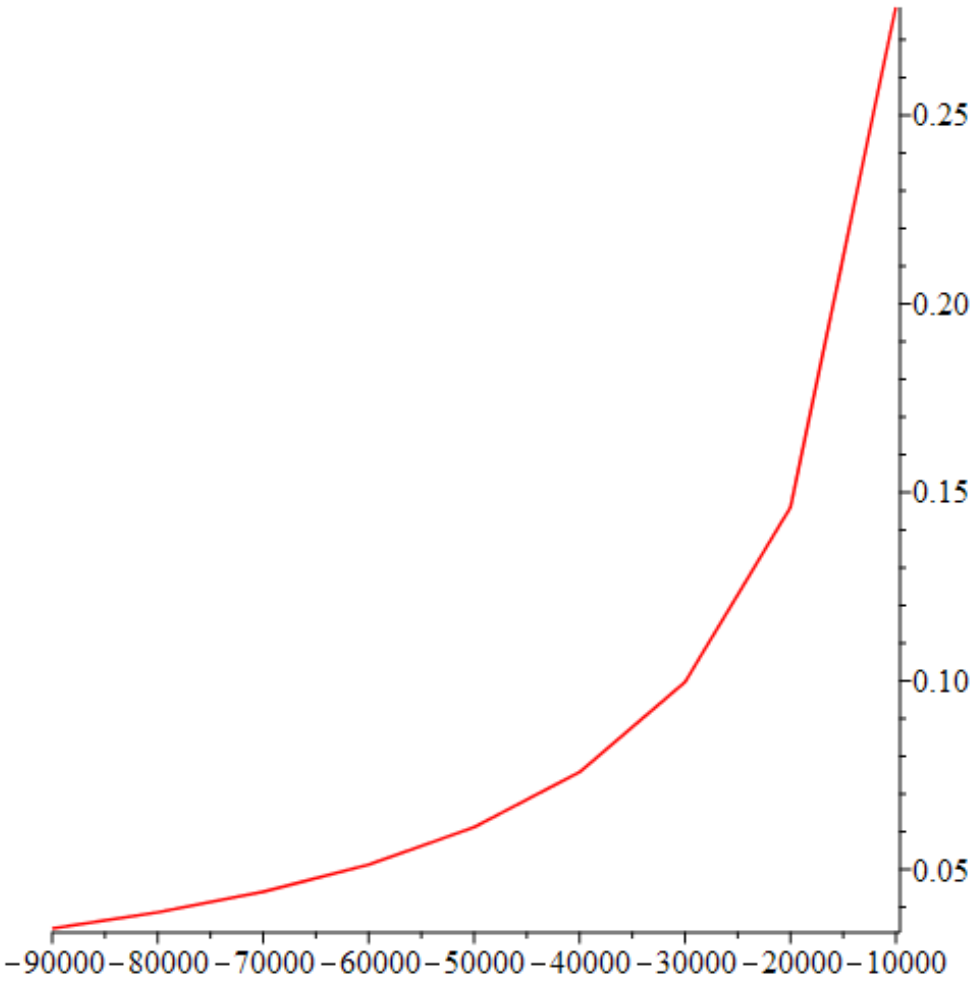

Figure 7.6: Percentage difference between the asymptotic equation (7.53) and the numerically calculated value of W for $\mu \in (-90000, -10000)$.

for parameters α and β. This moment generating function would then correspond to the probability distribution

$$dv_f(\lambda) := \vartheta(\lambda+\sigma)\frac{\beta^\alpha(\lambda+\sigma)^{\alpha-1}}{\Gamma(\alpha)}\exp(-\beta(\lambda+\sigma))\mathrm{d}\lambda. \tag{7.56}$$

7.5.1 Calculation in the $\lambda \to 2$ case

In the case of the limit approaching 2 we have the connected moment generating function given by 7.48. Exponentiating this function and ignoring higher order contributions for now gives the asymptotic moment generating function

$$\begin{aligned} M(\mu) &\sim \exp\left(-\sigma_2\mu + K_2 + \frac{1}{72}\log\left(\frac{2}{2-\mu}\right) - \right. \\ &\left. \frac{(18\pi)^{\frac{1}{3}}(2-\mu)^{\frac{2}{3}}}{80} + \mathcal{O}\left((2-\lambda)^{\frac{4}{3}}\right)\right) \\ &\sim \left(\frac{2}{2-\mu}\right)^{\frac{1}{72}}\exp\left(-\sigma_2\mu + K_2 - \frac{(18\pi)^{\frac{1}{3}}(2-\mu)^{\frac{2}{3}}}{80}\right)\left(1+\mathcal{O}\left((2-\lambda)^{\frac{4}{3}}\right)\right). \end{aligned} \tag{7.57}$$

Clearly there are strong comparisons between this and the moment generating function (7.55), demonstrating that the dominant behaviour of the Gauss-Lorentz test function's associated probability distribution is given by a shifted Gamma distribution at each end. This is valid as $\mu \to 2$ which means we will gain information about the tail end of the probability distribution but not much more.

This also shows that in the regime close to $\mu \to 2$ that the Gauss-Lorentz test function's associated probability does indeed deviate from the shifted Gamma probability distribution exhibited by every other known positive test function. It does however demonstrate that while this test function deviates from the shifted Gamma it is still dominated by it.

7.5.2 Calculation in the $\lambda \to -\infty$ case

Similarly to the case $\lambda \to 2$ we begin with the connected moment generating function for the relevant asymptotic limit (7.53)

$$\begin{aligned} M(\mu) &\sim \exp\left(-\sigma_\infty \mu + K_\infty + \frac{1}{24}\log\left(\frac{2}{2-\mu}\right)\right. \\ &\quad \left. -\frac{1}{16\log(2-\mu)} + \mathcal{O}\left(\log(2-\mu)^{-2}\right)\right) \\ &\sim \left(\frac{2}{2-\mu}\right)^{\frac{1}{24}} \exp\left(-\sigma_\infty \mu + K_\infty - \frac{1}{16\log(2-\mu)}\right)\left(1 + \mathcal{O}\left(\log(2-\mu)^{-2}\right)\right). \end{aligned} \tag{7.58}$$

This demonstrates agreement with the shifted Gamma distribution in the first order of the expansion but then deviation in the next order. The region of validity for this is $\mu \to -\infty$ which means that this will determine the singular behaviour of the probability distribution but not much more.

Both ends of the moment generating function have exhibited behaviour that would be similar to the shifted Gamma distribution but have also both shown that they deviate from the shifted Gamma in the next order of the expansion.

7.6 ASYMPTOTIC CALCULATION OF THE PROBABILITY DISTRIBUTION

Plotting the analytic distribution as in Fig. 7.7 for both the Gauss and Lorentz contributions to the test function demonstrates how in each regime the numerical calculation appears to tend towards the shifted Gamma distributions while disagreeing in the bulk.

7.6.1 Deviation from shifted Gamma

We have demonstrated that the Gaussian-Lorentzian test function smeared against the energy density (to first order in the second moment expansion) obeys the shifted Gamma distribution. However due to there being different parameters at each end, the overall distribution cannot be exactly described

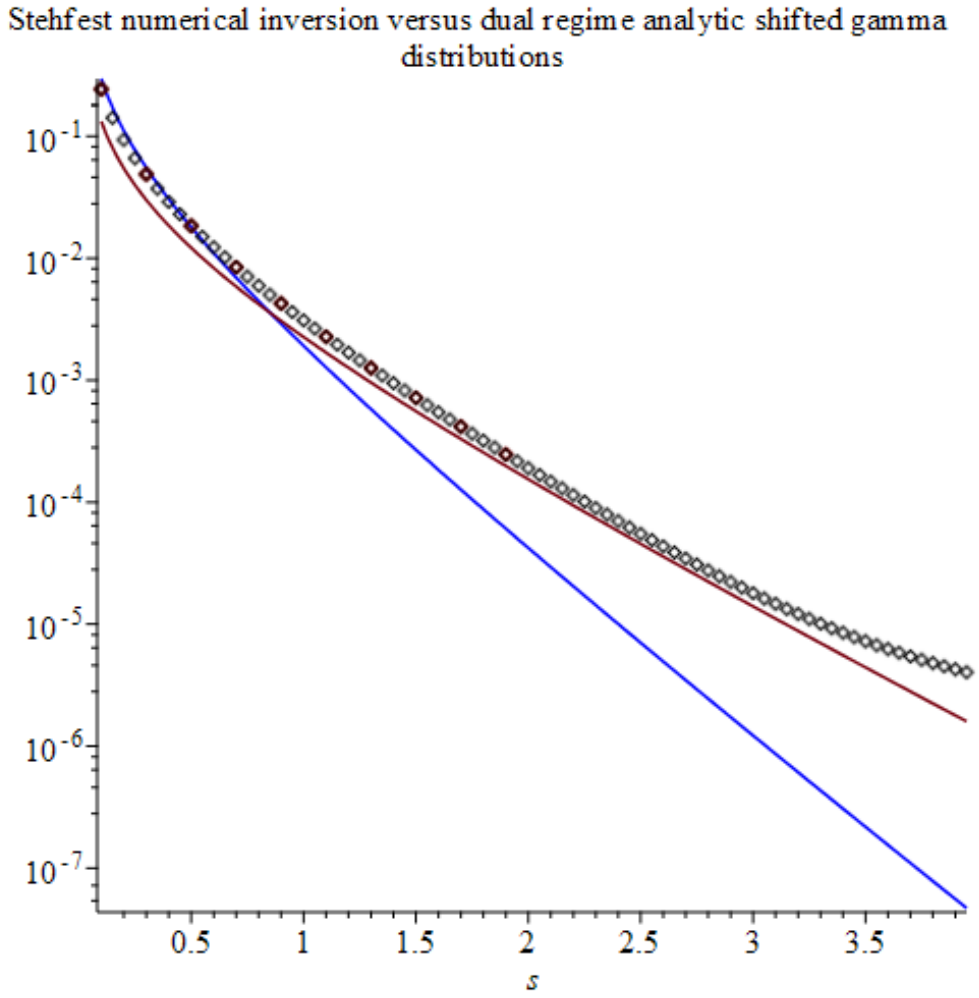

Figure 7.7: Plot showing the numerically calculated (squares) probability distribution for the Gauss-Lorentz test function compared to the first order asymptotic shifted gamma distribtions, (1.3) with Gaussian (blue) and Lorentzian (red) parameters. This plot demonstrates the agreement between the relevant shifted gamma distributions in both the large and small s regimes.

by the shifted Gamma probability density function. We will use a self-referential and uncontrolled analysis to attempt to invert these moment generating functions to calculate a more explicit effect on the probability distribution.

7.6.2 Laplace inversion of the moment generating function as $\mu \to 2$

We wish to calculate the probability distribution associated to the moment generating function (7.57). We begin by substituting

- $\chi = 1/72$
- $\omega = (18\pi)^{\frac{1}{3}}/80$

and re-write M

$$M(s) = \left(\frac{2}{2-s}\right)^{\chi} \exp\left(-\omega(2-s)^{2/3} - \sigma_2 s + K_2\right), \tag{7.59}$$

ignoring higher order terms for now. Recalling that

$$M(s) = \frac{e^{-\sigma s}}{(\beta - s)^{\alpha}} \to P(t) = \vartheta(t+\sigma)\frac{(t+\sigma)^{\alpha-1}}{\Gamma(\alpha)}e^{-\beta(t+\sigma)}, \tag{7.60}$$

we expand the exponent in (7.59) to find

$$M(s) = 2^{\chi} e^{K_2} e^{-\sigma_2 s}\left(\frac{1}{(2-s)^{\chi}} - \frac{\omega}{(2-s)^{\chi-\frac{2}{3}}} + \mathcal{O}((2-s)^{\frac{4}{3}-\chi})\right). \tag{7.61}$$

At this stage we can now proceed to perform a term by term transformation using (7.60) in each case to find the probability distribution $A_\infty(t)$

$$A_\infty(t) = 2^{\chi} e^{K_2}\vartheta(t+\sigma_2)e^{-2(t+\sigma_2)}\left(\frac{(t+\sigma_2)^{\chi-1}}{\Gamma(\chi)} - \frac{\omega\,(t+\sigma_2)^{\chi-\frac{5}{3}}}{\Gamma(\chi-\frac{2}{3})}\right). \tag{7.62}$$

In the first order of A_∞ we have found the prescribed shifted Gamma distribution and then a correcting term by the higher order.

7.6.3 The higher order Laplace inversion of moment generating function as $\mu \to -\infty$

We aim to calculate the probability density function as an inverse Laplace transform

$$p(t) = \lim_{T\to\infty} \frac{1}{2\pi i} \int_{\gamma-iT}^{\gamma+iT} e^{st} e^{W(-s)} ds, \tag{7.63}$$

integrating along the vertical line $Re(s) = \gamma$. We use the Bromwich inversion of the asymptotics of our connected moment generating function W. The formula (7.63) is exact but we are replacing W with our asymptotic approximations and attempt to compute the integral. We can recall W (7.53)

$$W(s) = \alpha \log\left(\frac{\beta}{\beta - s}\right) + k - s\sigma - \frac{1}{16\log(\beta - s)}, \tag{7.64}$$

where the constants α, β, σ and k are all given in the original formula. We substitute this into (7.63) and find

$$p(t) = \lim_{T\to\infty} \frac{1}{2\pi i} \int_{-iT}^{iT} \exp\left(st + \alpha \log\left(\frac{\beta}{\beta + s}\right) + k + s\sigma\right) \exp\left(\frac{-1}{16\log(\beta + s)}\right) ds, \tag{7.65}$$

having chosen $\gamma = 0$ due to this not passing through any singular points. We argue that provided we do not cross any singularities we are free to choose γ as we wish. If we choose γ near $-\beta$, the $1/\log(\beta + s)$ term is small which would allow us to accurately expand the exponential term. We then argue that this choice does not change the closed path integral value, nor does it change the value of the branch cut integrals as we take $T \to \infty$. Therefore we argue that this expansion will hold reasonably for $\gamma = 0$. Doing this we find

$$\begin{aligned} p(t) = \lim_{T\to\infty} \frac{1}{2\pi i} \int_{-iT}^{iT} \exp\left(st + \alpha \log\left(\frac{\beta}{\beta + s}\right) + k + s\sigma\right) (1 \\ - \frac{1}{16\log(\beta + s)} + \mathcal{O}\left(\left(\frac{-1}{16\log(\beta + s)}\right)^2\right)\Bigg) ds \end{aligned} \tag{7.66}$$

which gives us 2 integrals. The first term is identically the inverse Laplace transform of M which corresponds to a shifted Gamma distribution. The

second term is calculated to give an indication as to the deviation from the shifted Gamma.

Our aim is to calculate the following integral

$$p_1(t) = -\lim_{T\to\infty}\int_{-iT}^{iT}\frac{\exp\left(st+\alpha\log\left(\frac{\beta}{\beta+s}\right)+k+s\sigma\right)}{16\log\left(\beta+s\right)}ds \tag{7.67}$$

via the method of contour integration. A sketch of the contour we will be using is given by Fig 7.8. We therefore have to calculate

$$\frac{1}{2\pi i}\oint_C\frac{\exp\left(st+\alpha\log\left(\frac{\beta}{\beta+s}\right)+k+s\sigma\right)}{16\log\left(\beta+s\right)}ds =$$
$$\lim_{T\to\infty}\frac{1}{2\pi i}\left(\int_\Gamma+\int_{R_1}+\int_{R_2}+\int_{B_1}+\int_{B_2}+\int_J\right)\frac{\exp\left(st+\alpha\log\left(\frac{\beta}{\beta+s}\right)+k+s\sigma\right)}{16\log\left(\beta+s\right)}ds \tag{7.68}$$

where the 6 curves are defined as follows

- Γ The vertical curve we wish to calculate running from $-iT$ to iT
- R_1 Arc running from $\pi/2$ to $\pi-\delta$
- R_2 Arc running from $\pi+\delta$ to $3\pi/2$
- B_1 Branch cut above the negative real line
- B_2 Branch cut below negative real line
- J Semicircle centered at -2, joining the branch cut curves.

We will also use the notation $I_X(t)$ where we denote each individual contribution by the subscript X describing the curve. For example, we denote $I_\Gamma(t)$ when discussing the integral (7.67).

We have a pole at $s=-1$ which allows us to calculate the integral using the residue theorem by computing the residue at the enclosed pole. We also

expect the integrals along the 3 radial parametrisations to vanish when we take the large or small limits in each case. This will leave us to compute

$$I_\Gamma(t) = \frac{1}{2\pi i}\oint_C \frac{\exp\left(st + \alpha\log\left(\frac{\beta}{\beta+s}\right) + k + s\sigma\right)}{16\log(\beta+s)}ds - I_{B_1}(t) + I_{B_2}(t) \quad (7.69)$$

to calculate (7.67).

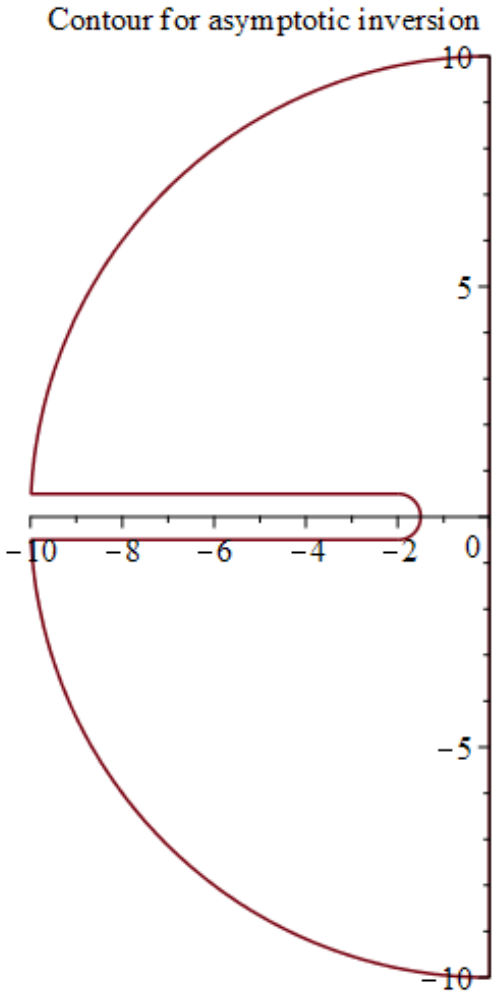

Figure 7.8: Scaled down contour demonstrating key ideas of path integral (7.68).

Beginning with proving the radial contributions vanish we choose $s = Te^{i\theta}$

with $\theta \in (\pi/2, \pi - \delta)$ giving

$$I_{R_1}(t) = \frac{e^k}{2\pi i} \int_{\frac{\pi}{2}}^{\pi-\delta} iTe^{i\theta} \frac{\exp\left(Te^{i\theta}(t+\sigma) + \frac{c}{24}\log\left(\frac{2}{2+Te^{i\theta}}\right)\right)}{16\log\left(2+Te^{i\theta}\right)} d\theta \tag{7.70}$$

where we have substituted $\beta = 2$ and replaced α with $c/24$ with c the central charge of the theory. We bring the logarithm down from the exponent and analyse how the integrand behaves when we take the limit $T \to \infty$. Expanding also the complex exponential we have

$$I_{R_1}(t) = \frac{e^k}{2\pi i} \int_{\frac{\pi}{2}}^{\pi-\delta} iTe^{i\theta} \left(\frac{2}{2+Te^{i\theta}}\right)^{\frac{c}{24}} \frac{\exp\left(T(\cos\theta + i\sin\theta)(t+\sigma)\right)}{16\log\left(2+Te^{i\theta}\right)} d\theta, \tag{7.71}$$

noticing that the real part in the exponent is negative in the range $\theta \in (\pi/2, 3\pi/2)$. The exponential term will dominate this integrand and converge to 0 when we take the limit $T \to \infty$. This fact is only true if we have $t > -\sigma$, otherwies we face divergence from the exponential. Due to the parametrisation of the other radial contribution R_2 we can argue the same fact and find that both contributions vanish as we take the limit $T \to \infty$.

We now calculate the branch cut contributions

$$I_{B_1}(t) + I_{B_2}(t) = \frac{e^k}{2\pi i}\left(\int_{B_1} + \int_{B_2}\right) \frac{\exp\left(st + \alpha\log\left(\frac{\beta}{\beta+s}\right) + k + s\sigma\right)}{16\log\left(\beta+s\right)} ds, \tag{7.72}$$

with parameters as follows (ignoring the effect of the 2 on the $T \to \infty$)

- B_1, $s \in (-T + i\delta, -2 + i\delta)$
- B_2, $s \in (-2 - i\delta, -T - i\delta)$.

In both cases we will change parameters via $s = -2 - p$ and write the integrand used for both integrals as

$$I(-2-p) = \left(-\frac{p}{2}\right)^{-\frac{c}{24}} \frac{\exp\left(-2-p\right)(t+\sigma)}{16\log\left(-p\right)} \tag{7.73}$$

which transforms our boundary conditions to

- B_1, $p \in (T + i\delta, i\delta)$
- B_2, $p \in (-i\delta, T - i\delta)$.

We can take care of the slight shift away from the real axis by setting $-p = |p|e^{i(\pi-\epsilon)}$ for the first integral and $-p = |p|e^{-i(\pi-\epsilon)}$ for the second, giving us the following integrals. First we look at I_{B_1}

$$I_{B_1}(t) = -\frac{e^k}{2\pi i}\int_T^0 \left(\frac{|p|}{2}\right)^{-\frac{c}{24}} e^{-\frac{ic\pi}{24}} \frac{\exp\left((-2-p)(t+\sigma)\right)}{16\log\left(|p|\right)+16i\pi}dp, \tag{7.74}$$

noticing that we have picked up a minus from the metric after coordinate transform. We have taken the limit $\epsilon \to 0$ carefully and if we restrict our p to the positive real axis we can re-write this as

$$I_{B_1}(t) = \frac{e^k}{2\pi i}\int_0^T \left(\frac{p}{2}\right)^{-\frac{c}{24}} e^{\frac{ic\pi}{24}} \frac{\exp\left((-2-p)(t+\sigma)\right)}{16\log\left(p\right)+16i\pi}dp. \tag{7.75}$$

Performing a similar analysis for I_{B_2} we find

$$I_{B_2}(t) = -\frac{e^k}{2\pi i}\int_0^T \left(\frac{|p|}{2}\right)^{-\frac{c}{24}} e^{-\frac{ic\pi}{24}} \frac{\exp\left((-2-p)(t+\sigma)\right)}{16\log\left(|p|\right)-16i\pi}dp. \tag{7.76}$$

Simplifying the latter integral and performing the addition required of the two integrals and grouping terms we find

$$I_{B_1}(t) + I_{B_2}(t) =$$
$$\frac{e^k}{2\pi i}\int_0^T \left(\left(\frac{p}{2}\right)^{-\frac{c}{24}} \exp\left((-2-p)(t+\sigma)\right)\left(\frac{e^{-\frac{ic\pi}{24}}}{16\log\left(p\right)+16i\pi} - \frac{e^{\frac{ic\pi}{24}}}{16\log\left(p\right)-16i\pi}\right)\right)dp. \tag{7.77}$$

Simplifying this to trigonometric terms we have

$$I_{B_1}(t) + I_{B_2}(t) =$$
$$\frac{e^k}{2\pi i}\int_0^T \left(\left(\frac{p}{2}\right)^{-\frac{c}{24}} \exp\left((-2-p)(t+\sigma)\right)\left(-\frac{2i\log\left(p\right)\sin\left(\frac{c\pi}{24}\right) - 2i\pi\cos\left(\frac{c\pi}{24}\right)}{16\pi^2+16\log\left(p\right)^2}\right)\right)dp \tag{7.78}$$

which we cancel and it becomes purely real. This is encouraging because we require the probability to be real and this is a part of a correction to our

probability asymptotics

$$I_{B_1}(t) + I_{B_2}(t) =$$
$$-\frac{e^k}{\pi}\int_0^T \left(\left(\frac{p}{2}\right)^{-\frac{c}{24}} \exp\left((-2-p)(t+\sigma)\right)\left(\frac{\log(p)\sin\left(\frac{c\pi}{24}\right)+\pi\cos\left(\frac{c\pi}{24}\right)}{16\pi^2+16\log(p)^2}\right)\right)dp. \tag{7.79}$$

This leaves us to find $2\pi i$ multiplied by the residue which can be found to be

$$\frac{1}{2\pi i}\oint_C \frac{\exp\left(st+\alpha\log\left(\frac{\beta}{\beta+s}\right)+k+s\sigma\right)}{16\log(\beta+s)}ds = \frac{2^{\frac{c}{24}}}{16}\exp(k-t-\sigma). \tag{7.80}$$

We have already cancelled the factor of $2\pi i$ appearing in the Bromwich inversion formula and the residue formula for evaluating contour integrals. Combining this we find

$$\lim_{T\to\infty}\frac{1}{2\pi i}\int_{-iT}^{iT}\frac{\exp\left(st+\frac{c}{24}\log\left(\frac{2}{2+s}\right)+k+s\sigma\right)}{16\log(2+s)}ds =$$
$$\frac{2^{\frac{c}{24}}}{16}\exp(k-t-\sigma)+$$
$$\frac{e^k}{\pi}\int_0^\infty \left(\left(\frac{p}{2}\right)^{-\frac{c}{24}} \exp\left((-2-p)(t+\sigma)\right)\left(\frac{\log(p)\sin\left(\frac{c\pi}{24}\right)+\pi\cos\left(\frac{c\pi}{24}\right)}{16\pi^2+16\log(p)^2}\right)\right)dp \tag{7.81}$$

which is a formula that should allow one to find numerical information about the Laplace transform of the higher order asymptotic contribution. However, we need to be careful here due to the convergence of $I_{B_1}(t) + I_{B_2}(t)$. We wish to take the inverse transform for some

$$G(s) = \left(\frac{2+s}{s}\right)F(s), \tag{7.82}$$

with

$$F(s) = \left(\frac{2+s}{2}\right)^{-1-\frac{c}{24}}\frac{e^{k+s\sigma}}{16\log(2+s)}. \tag{7.83}$$

We use standard properties of Laplace transforms to find that this relationship gives us

$$2g(t) = f'(t) + 2f(t), \quad f(0) = 0 \tag{7.84}$$

defining g as the inverse transform of G and

$$f(t) = \frac{d}{dt}\left(e^{2t}\lim_{T\to\infty}\frac{1}{2\pi i}\int_{-iT}^{iT}\frac{\exp\left(st+\frac{c}{24}\log\left(\frac{2}{2+s}\right)+k+s\sigma\right)}{16\log\left(2+s\right)}ds\right) \quad (7.85)$$

as the inverse of F.

We rearrange this formula to find

$$g(t) = \frac{1}{2}e^{-2t}\frac{d\left(e^{2t}f(t)\right)}{dt} \quad (7.86)$$

and we can now to move directly from (7.81) to calculating $g(t)$ by replacing $c = c + 24$ and performing the operations prescribed by the transform laws. Multiplying by the exponential of twice the transform variable gives

$$e^{2t}f(t) = \frac{2^{1+\frac{c}{24}}}{16}\exp\left(k+t-\sigma\right)+$$
$$\frac{e^k}{\pi}\int_0^\infty\left(\left(\frac{p}{2}\right)^{-1-\frac{c}{24}}\exp\left(-pt-2\sigma-p\sigma\right)\left(\frac{-\log\left(p\right)\sin\left(\frac{c\pi}{24}\right)-\pi\cos\left(\frac{c\pi}{24}\right)}{16\pi^2+16\log\left(p\right)^2}\right)\right)dp, \quad (7.87)$$

where the change in central charge caused the negative trigonometric terms. We simplify and differentiate this with respect to t to find

$$\frac{d}{dt}\left(e^{2t}f(t)\right) = \frac{2^{1+\frac{c}{24}}}{16}\exp\left(k+t-\sigma\right)+$$
$$\frac{e^k}{\pi}\int_0^\infty\left(\left(\frac{p}{2}\right)^{-1-\frac{c}{24}}\exp\left(-pt-2\sigma-p\sigma\right)\left(\frac{-\log\left(p\right)\sin\left(\frac{c\pi}{24}\right)-\pi\cos\left(\frac{c\pi}{24}\right)}{16\pi^2+16\log\left(p\right)^2}\right)\right)dp, \quad (7.88)$$

noticing that the negatives in the integrand now cancel as well as one factor of p leaving us with

$$\frac{d}{dt}\left(e^{2t}f(t)\right) = \frac{2^{1+\frac{c}{24}}}{16}\exp\left(k+t-\sigma\right)+$$
$$2\frac{e^k}{\pi}\int_0^\infty\left(\left(\frac{p}{2}\right)^{-\frac{c}{24}}\exp\left(-pt-2\sigma-p\sigma\right)\left(\frac{\log\left(p\right)\sin\left(\frac{c\pi}{24}\right)+\pi\cos\left(\frac{c\pi}{24}\right)}{16\pi^2+16\log\left(p\right)^2}\right)\right)dp. \quad (7.89)$$

Finally we multiply out the exponential contribution and then halve the remainder giving us

$$g(t) = \frac{2^{\frac{c}{24}}}{16} \exp(k - t - \sigma) + \frac{e^k}{\pi} \int_0^\infty \left(\left(\frac{p}{2}\right)^{-\frac{c}{24}} \exp(-2t - pt - 2\sigma - p\sigma) \left(\frac{\log(p) \sin\left(\frac{c\pi}{24}\right) + \pi \cos\left(\frac{c\pi}{24}\right)}{16\pi^2 + 16 \log(p)^2} \right) \right) dp. \tag{7.90}$$

This higher order correction to the asymptotic probability distribution allows us to improve the asymptotic agreement of the probability and increase the region of validity of the asymptotic formula.

The integral in the second term of the correction (7.90) is resolved numerically but is stable for all values of t which we are interested in computing.

The total probability distribution in this regime is given by

$$A_0(t) = \frac{\beta^\alpha}{\Gamma(\alpha)} (t + \sigma)^{\alpha - 1} e^{-\beta(t+\sigma)} - g(t) \tag{7.91}$$

which to first order obeys the shifted Gamma distribution just as in the case (7.62).

To understand the benefits that the higher order asymptotic expansions (7.62) and (7.91) have given, we compare these two formulae to the numerically calculated probability distribution. In Fig. 7.9 we have set the vertical axis onto a logarithmic scale to allow for a clearer comparison between the data and the asymptotic probability formulae. It is clear that the higher order (7.62) behaves far better than the first order shifted Gamma approximation made. This improvement gives evidence to the deviation from the shifted Gamma in this regime.

We also wish to see the improvement made by (7.91) towards the singularity of the probability distribution. This can be seen in Fig. 7.10 which compares the behaviour of (7.91) to the first order shifted Gamma distribution and the numerically calculated probability distribution in this regime.

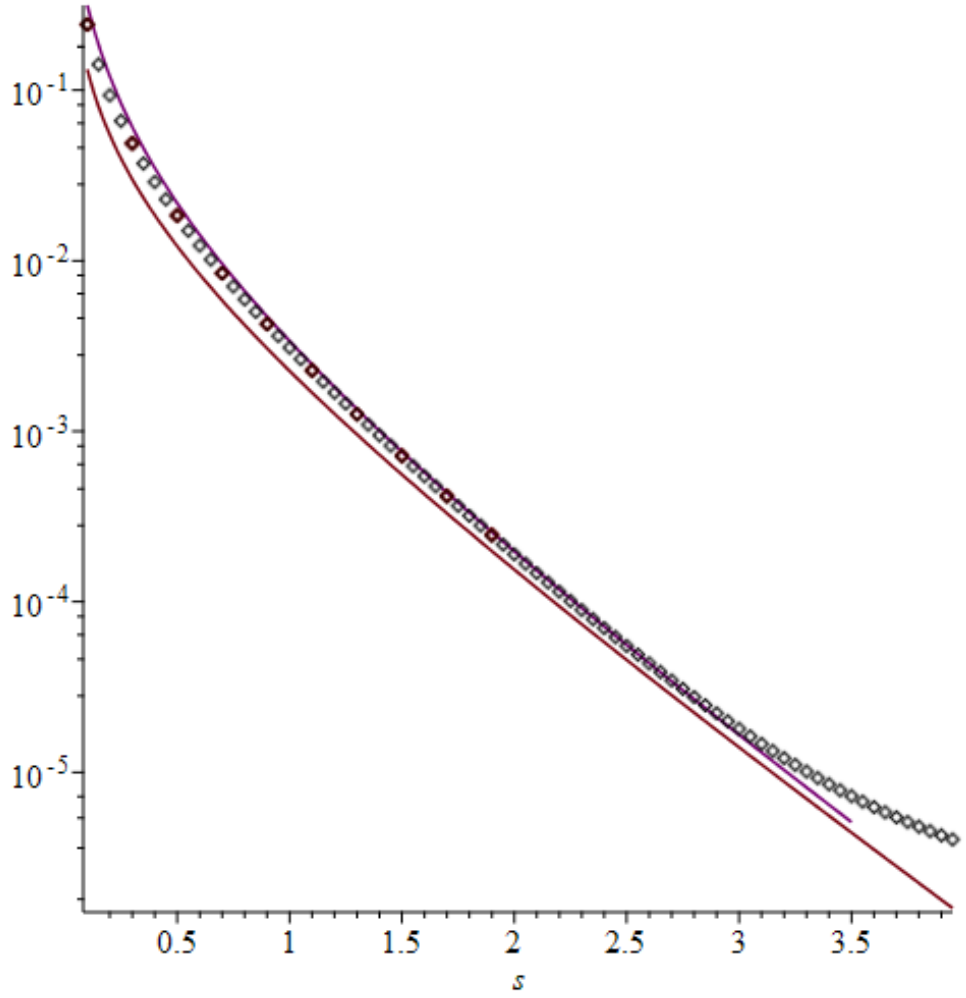

Figure 7.9: Plot comparing the numerically calculated probability distribution (points) against the shifted Gamma distribution for Lorentzian parameters (red) and the plot containing all terms of (7.62).

Once more there is a clear improvement to the agreement of the probability distribution by including the higher order contribution. However, what is not shown on this plot is the very poor agreement by (7.91) as one moves away from the singularity. This is unsurprising because asymptotics often fail when too far from their region of validity.

Having used the method of moments to calculate asymptotics of the

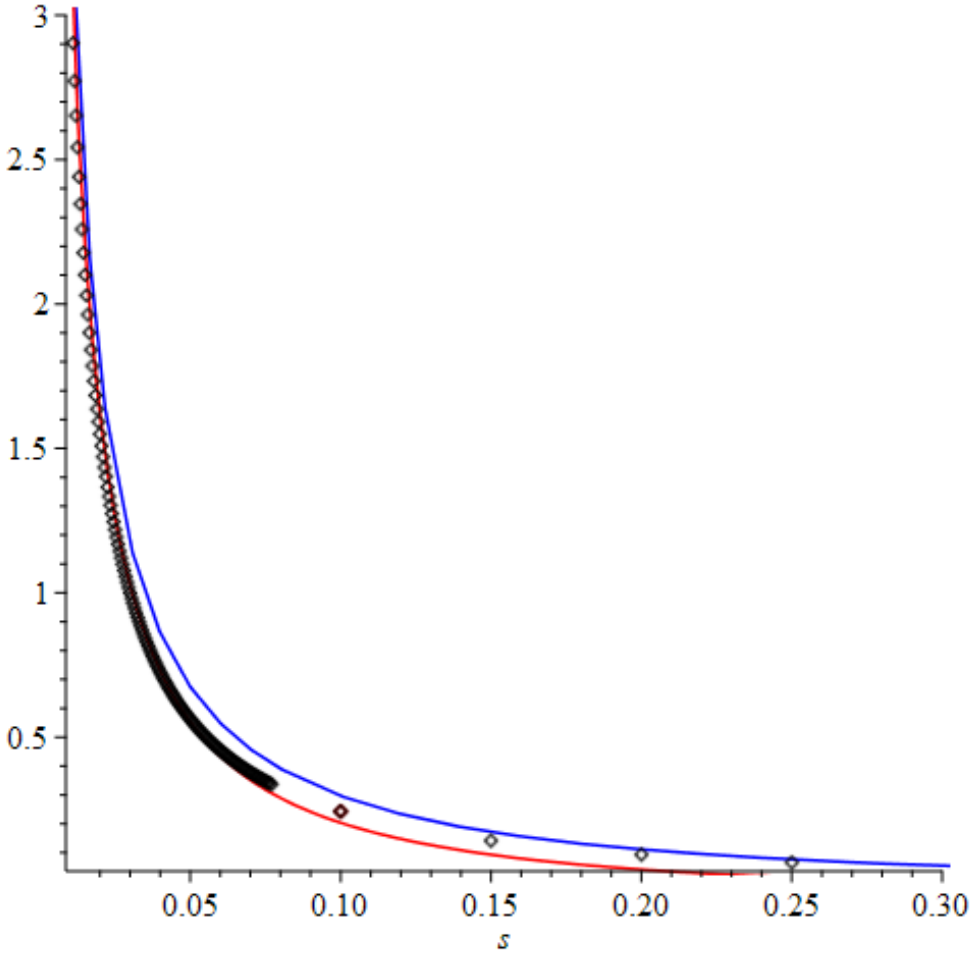

Figure 7.10: Plot comparing the numerically calculated probability distribution (points) against the shifted Gamma distribution for Gaussian parameters (red) and the plot containing all terms of (7.91).

probability distribution in the relevant regimes, we have shown an argument for deviation from shifted Gamma in each end of the probability distribution. We had already shown that the Gauss-Lorentz test function was not purely governed by a shifted Gamma distribution. By inverting the Laplace transforms we have shown that this deviation is still apparent and we have given an asymptotic description as to how it deviates. In comparing the bulk numerical Laplace inversion to the asymptotics at each end of

the distribution (7.62), (7.91), we found that these asymptotics perform well against the numerical results. The numerical calculation will fail if it approaches the singularity or for too large a value of t. This failure for larger values of t can be seen beginning in Fig. 7.7 and is more visible in Fig. 7.9. It is at this point we will have to trust that the asymptotics accurately describe the behaviour in their respective limits.

— 8 —

Verification of the asymptotic moments method & conformal welding

We have discussed two methods for the calculation of the probability distribution of the smeared energy density depending upon the test function used to smear the observable. Recall that $p(t)$ is the probability density function for individual measurements t of $T(f)$ in the vacuum state. We wish to compare the two methods in the case of the Gauss-Lorentz test function. The welding method calculates the Fourier transform of the probability distribution which we will compare to the Fourier transform of the distribution calculated from the moments method using a mixture of numerical and asymptotic techniques. We compute $p(t)$ by different methods in different regimes which may be expressed as a piecewise defined function from the moments method

$$p(t) = \begin{cases} A_0(t)\vartheta(t+\sigma) & t < \delta \\ N(t) & \delta \leq t < \Delta \\ A_\infty(t) & t \geq \Delta \end{cases}, \tag{8.1}$$

defining the asymptotic contributions by the character A and the numerically calculated region by N. One should note we are using the definitions A_0 as in (7.91) and A_∞ as in (7.62). Strictly speaking $p(t)$ is an approximation to the true probability distribution because we have only computed the first few terms of the asymptotics. We wish to calculate

$$\mathcal{F}(p)(\omega) = \tilde{p}(\omega) = \int_{\mathbb{R}} p(t) e^{i\omega t} dt \tag{8.2}$$

which can be split into 3 integrals, one numeric and two analytic. This simplifies to

$$\tilde{p}(\omega) = \int_{-\sigma}^{\delta} A_0(t)e^{i\omega t}dt + \int_{\delta}^{\Delta} N(t)e^{i\omega t}dt + \int_{\Delta}^{\infty} A_\infty(t)e^{i\omega t}dt, \tag{8.3}$$

choosing values for (δ, Δ) such that the asymptotic calculations of the probabilities A_0 and A_∞ provide good approximation of the probability. We define $\tilde{A}_0$ and $\tilde{A}_\infty$ as the integrals

$$\tilde{A}_0 = \int_{-\sigma}^{\delta} A_0(t)e^{i\omega t}dt, \tag{8.4}$$

$$\tilde{A}_\infty = \int_{\Delta}^{\infty} A_\infty(t)e^{i\omega t}dt. \tag{8.5}$$

Separating (8.3) into 3 distinct parts we begin with the region near the singularity related to the quantum energy inequality

$$\int_{-\sigma}^{\delta} A_0(t)e^{i\omega t}dt = \int_{-\sigma}^{\delta} \frac{\beta^\alpha}{\Gamma(\alpha)} (t+\sigma)^{\alpha-1} e^{-\beta(t+\sigma)} e^{i\omega t}dt - \int_{-\sigma}^{\delta} g(t)e^{i\omega t}dt, \tag{8.6}$$

simplifying the higher order asymptotic contribution to the function $g(t)$ defined by (7.90).

8.1 FIRST ORDER FOURIER CONTRIBUTIONS FROM THE ASYMPTOTIC PROBABILITY DENSITY

We further separate the integral, first analysing the effect of the dominant term in the asymptotic series. We use the following expressions for the Gamma function and upper incomplete Gamma function

$$\int_0^\infty x^{a-1}e^{-bx}dx = \frac{\Gamma(a)}{b^a} \tag{8.7}$$

$$\int_L^\infty x^{a-1}e^{-bx}dx = \frac{\Gamma(a,bL)}{b^a}, \tag{8.8}$$

$$\int_0^L x^{a-1}e^{-bx}dx = \frac{\Gamma(a)}{b^a} - \frac{\Gamma(a,bL)}{b^a}. \tag{8.9}$$

Taking complex arguments into (8.9) allows us to calculate

$$\begin{gathered}\int_{-\sigma}^{\delta} \frac{\beta^\alpha}{\Gamma(\alpha)} (t+\sigma)^{\alpha-1} e^{-\beta(t+\sigma)} e^{i\omega t}dt = \\ \frac{\beta^\alpha}{(\beta-i\omega)^\alpha} \frac{e^{-i\omega\sigma}}{\Gamma(\alpha)} \left(\Gamma(\alpha) - \Gamma(\alpha, (\beta-i\omega)(\delta+\sigma))\right).\end{gathered} \tag{8.10}$$

At this stage we have only calculated the first order contributions to $\tilde{A}_0$ and we progress to calculating $\tilde{A}_\infty$.

Ultimately we aim to calculate

$$\begin{gathered}\int_\Delta^\infty A_\infty(t)e^{i\omega t}dt = \\ \int_\Delta^\infty 2^\chi e^{\eta-2t-2\zeta+i\omega t}\frac{(t+\zeta)^{\chi-1}}{\Gamma(\chi)}dt- \\ \int_\Delta^\infty 2^\chi e^{\eta-2t-2\zeta+i\omega t}\frac{\Omega\,(t+\zeta)^{\chi-\frac{5}{3}}}{\Gamma(\chi-\frac{2}{3})}dt,\end{gathered} \tag{8.11}$$

for χ, η, and ζ the same constants as in (7.62) and $\Omega = (18\pi)^{\frac{1}{3}}/80$. For now we are only interested in calculating the effect of the dominant part of A_∞.

We use the identity (8.8) with complex arguments to calculate

$$\int_\Delta^\infty 2^\chi e^{\eta-2t-2\zeta+i\omega t}\frac{(t+\zeta)^{\chi-1}}{\Gamma(\chi)}dt = \frac{2^\chi e^{\eta-i\omega\zeta}}{\Gamma(\chi)}\frac{\Gamma(\chi,(2-i\omega)(\Delta+\zeta))}{(2-i\omega)^\chi}. \tag{8.12}$$

This gives us a first order approximation to $\tilde{p}$ from (8.3) using (8.10) and (8.12)

$$\begin{gathered}\tilde{p}(\omega) = \frac{\beta^\alpha}{(\beta-i\omega)^\alpha}\frac{e^{-i\omega\sigma}}{\Gamma(\alpha)}\left(\Gamma(a)-\Gamma(\alpha,(\beta-i\omega)\,(\delta+\sigma))\right)+ \\ \int_\delta^\Delta N(t)e^{i\omega t}dt+ \\ \frac{2^\chi e^{\eta-i\omega\zeta}}{\Gamma(\chi)}\frac{\Gamma(\chi,(2-i\omega)(\Delta+\zeta))}{(2-i\omega)^\chi}.\end{gathered} \tag{8.13}$$

We need to calculate $\tilde{p}$ analytically near the singularity in A_0. This is because numerically, one is unable to accurately calculate the contribution to the distribution resulting from this region. The value of the Fourier transform at 0 gives the total integrated value of the probability distribution. This means that one would hope to generate a value very near or equal to 1. If one neglects to include the contribution $\tilde{A}_0$ then the value at 0 is calculated to be approximately 0.43. The inclusion of $\tilde{A}_0$ increases this value to 0.9961145947 meaning we are capturing well over 50% more of the distribution compared

to neglecting A_0. We also wish to demonstrate a comparison between $\tilde{p}$ and the corresponding curve generated using the welding method which is shown in Fig. 8.1. To understand this more quantitatively we consider

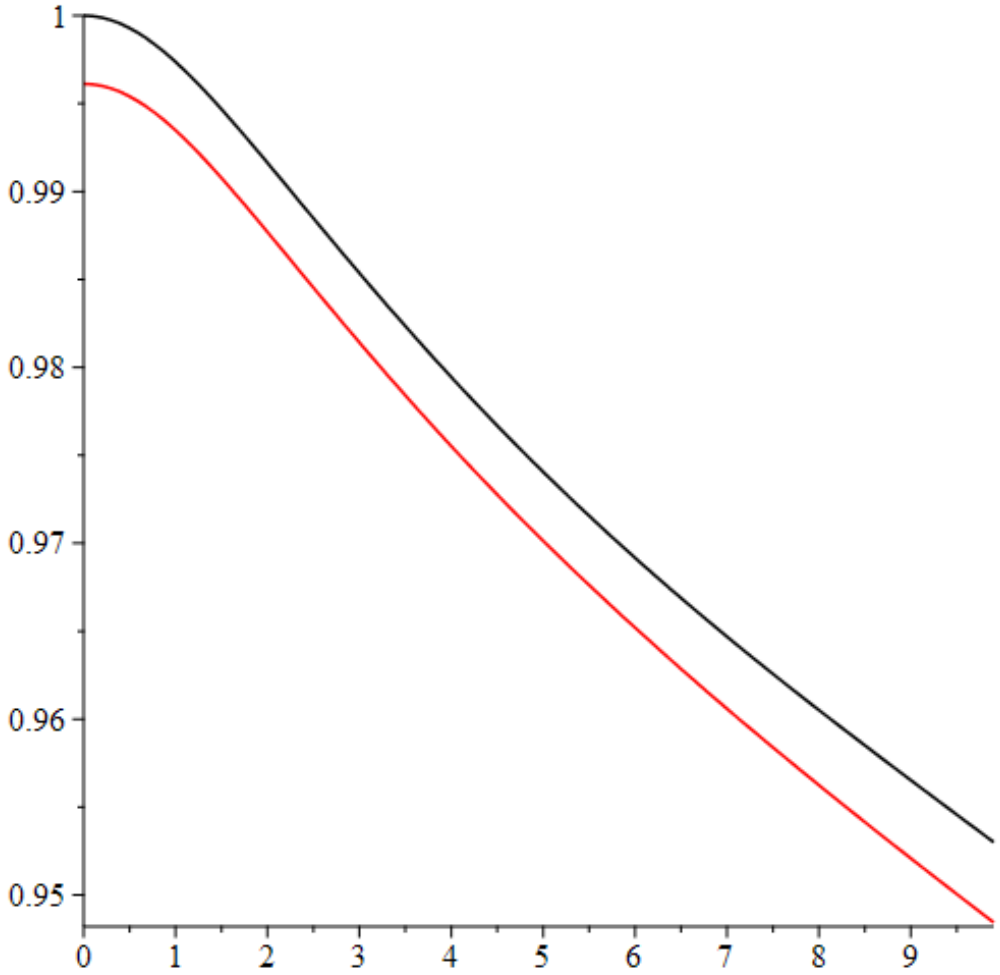

Figure 8.1: Numerical plot of the real parts of the Fourier distribution calculated using the welding method (black) (same as in Fig. 6.5) associated to a Gauss-Lorentz test function) and (8.13) calculated from the moments method.

the percentage difference of the two in the range as demonstrated by Fig. 8.1.

As discussed previously, the welding method ensures that the character-

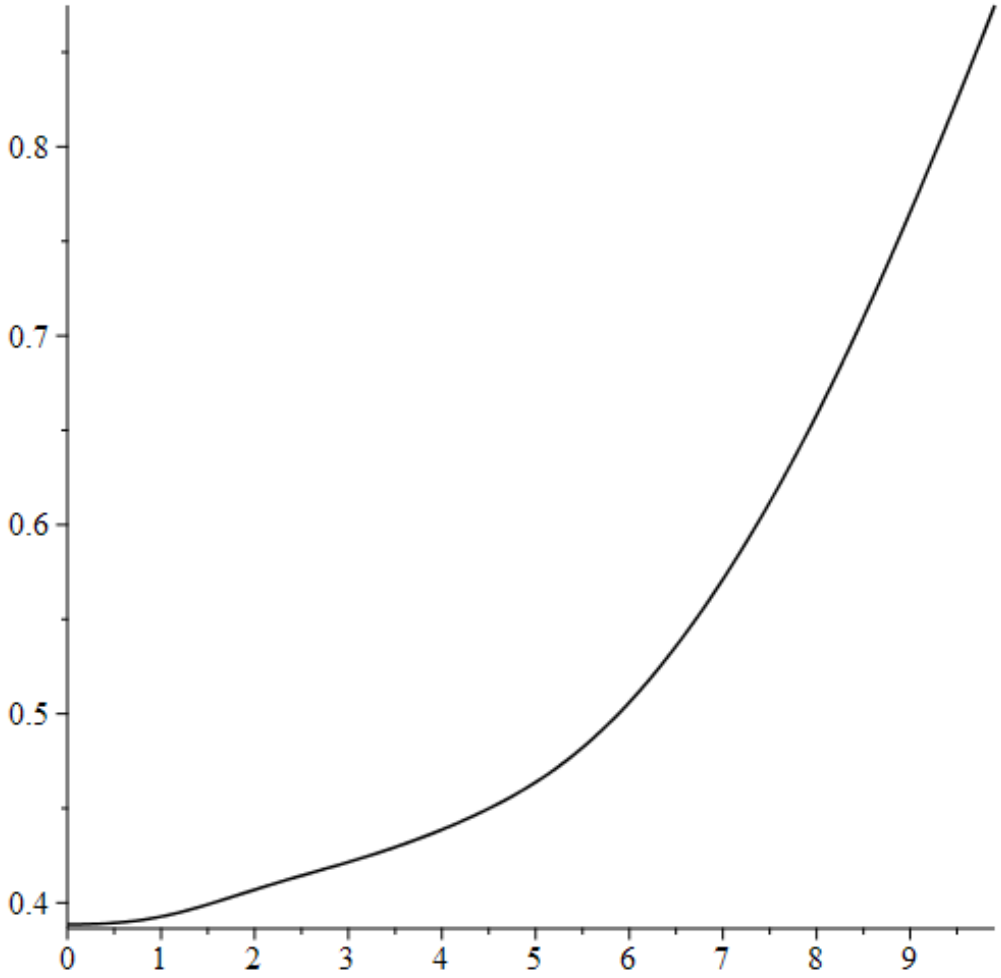

Figure 8.2: Plot of the percentage difference of the points within 8.1.

istic function of the probability distribution begins at 1. This can clearly be seen in (2.22) where if we integrate to $t = 0$ the exponent vanishes generating a value of 1 for the characteristic function. The asymptotic moments method does not benefit from this and the fact that the method of moments is able to closely approach a value of 1 is a consistency check on the calculation performed.

8.2 HIGHER ORDER CORRECTIONS TO $\tilde{p}$

We now include the higher order asypmtotic contributions for A_0 and A_∞. We begin by calculating the fourier transform of A_∞ as defined by (7.62), using (8.8)

$$\begin{gathered}\int_\Delta^\infty 2^\chi e^{\eta-2t-2\zeta+i\omega t}\frac{\Omega\,(t+\zeta)^{\chi-\frac{5}{3}}}{\Gamma(\chi-\frac{2}{3})}dt = \\ -\frac{2^\chi\Omega e^{\eta-i\omega\zeta}}{\Gamma(\chi-\frac{2}{3})}\frac{\Gamma(\chi-\frac{2}{3},(2-i\omega)(\Delta+\zeta))}{(2-i\omega)^{(\chi-\frac{2}{3})}}.\end{gathered} \tag{8.14}$$

This means that we have found $\tilde{A}_\infty$

$$\begin{gathered}\tilde{A}_\infty(\omega)=\int_\Delta^\infty A_\infty(t)e^{i\omega t}dt = \\ 2^\chi e^{\eta-i\omega\zeta}\left(\frac{\Gamma(\chi,(2-i\omega)(\Delta+\zeta))}{\Gamma(\chi)(2-i\omega)^\chi}-\frac{\Omega\Gamma(\chi-\frac{2}{3},(2-i\omega)(\Delta+\zeta))}{\Gamma(\chi-\frac{2}{3})(2-i\omega)^{(\chi-\frac{2}{3})}}\right),\end{gathered} \tag{8.15}$$

leaving us only to calculate the contribution from the singular region of the probability density.

We have already calculated the Fourier transform of the shifted Gamma in the singular region so we need only to transform (7.90)

$$\begin{gathered}\tilde{g}(\omega)=\int_{-\sigma}^{\delta}e^{i\omega t}\left(\frac{2^{\frac{c}{24}}}{16}\exp\left(k-t-\sigma\right)+\right. \\ \left.\frac{e^k}{\pi}\int_0^\infty\left(\left(\frac{p}{2}\right)^{-\frac{c}{24}}\exp\left(-2t-pt-2\sigma-p\sigma\right)F(p)\right)dp\right)dt.\end{gathered} \tag{8.16}$$

We exchange the order of integration which allows us to integrate over t and then once more we are left with an integral over the p domain

$$\begin{gathered}\frac{2^{\frac{c}{24}}}{16}\frac{e^{k-\sigma}}{i\omega-1}\left(e^{\delta(i\omega-1)}-e^{-\sigma(i\omega-1)}\right)+ \\ \frac{e^k}{\pi}\int_0^\infty\left(\frac{p}{2}\right)^{-\frac{c}{24}}\frac{F(p)e^{-2(p+\sigma)}}{i\omega-2-p}\left(e^{\delta(i\omega-2-p)}-e^{-\sigma(i\omega-2-p)}\right)dp.\end{gathered} \tag{8.17}$$

This gives the higher order approximation to the Fourier transform as

$$\begin{aligned}\tilde{p}(\omega) = &\frac{\beta^{\alpha}}{(\beta - i\omega)^{\alpha}} \frac{e^{-i\omega\sigma}}{\Gamma(\alpha)} \left(\Gamma(\alpha) - \Gamma(\alpha, (\beta - i\omega)(\delta + \sigma))\right) - \\ &\frac{2^{\frac{c}{24}}}{16} \frac{e^{k-\sigma}}{i\omega - 1} \left(e^{\delta(i\omega-1)} - e^{-\sigma(i\omega-1)}\right) - \\ &\frac{e^{k}}{\pi} \int_0^{\infty} \left(\frac{p}{2}\right)^{-\frac{c}{24}} \frac{F(p)e^{-2(p+\sigma)}}{i\omega - 2 - p} \left(e^{\delta(i\omega-2-p)} - e^{-\sigma(i\omega-2-p)}\right) dp + \\ &\int_{\delta}^{\Delta} N(t) e^{i\omega t} dt + \\ &\frac{2^{\chi} e^{\eta - i\omega\zeta}}{\Gamma(\chi)} \frac{\Gamma(\chi, (2 - i\omega)(\Delta + \zeta))}{(2 - i\omega)^{\chi}} - \\ &\frac{2^{\chi} \Omega e^{\eta - i\omega\zeta}}{\Gamma(\chi - \frac{2}{3})} \frac{\Gamma(\chi - \frac{2}{3}, (2 - i\omega)(\Delta + \zeta))}{(2 - i\omega)^{\left(\chi - \frac{2}{3}\right)}}.\end{aligned} \tag{8.18}$$

With this formula we can draw a comparison between the welding method and the higher order moments method in Fourier space by choosing $\delta = 0.01$ and $\Delta = 2.44$. This comparison can be seen in Fig. 8.3. Both curves were calculated numerically but clearly there is no real improvement compared to Fig. 8.1. We can compare the percentage differences between the welding method and the higher order correction by generating Fig. 8.4. This plot can then be compared to Fig. 8.1 and it is clear that the percentage difference plots both follow the same general path of increase but using the higher order corrections to the asymptotics there are regions where the new method performs worse and others where it performs better.

It is unfortunate that in the Fourier domain the higher order corrections to the probability asymptotics do not give an obviously better match to the welding results when compared to the first order calculation. This underwhelming improvement of the higher order method and periodic regions of worse performance means that the improvements in the probability asymptotics did not carry over to the Fourier domain when transformed as well as we would have hoped.

We have seen that the asymptotic and numerical results can be transformed into the Fourier domain as a verification of moment method generated

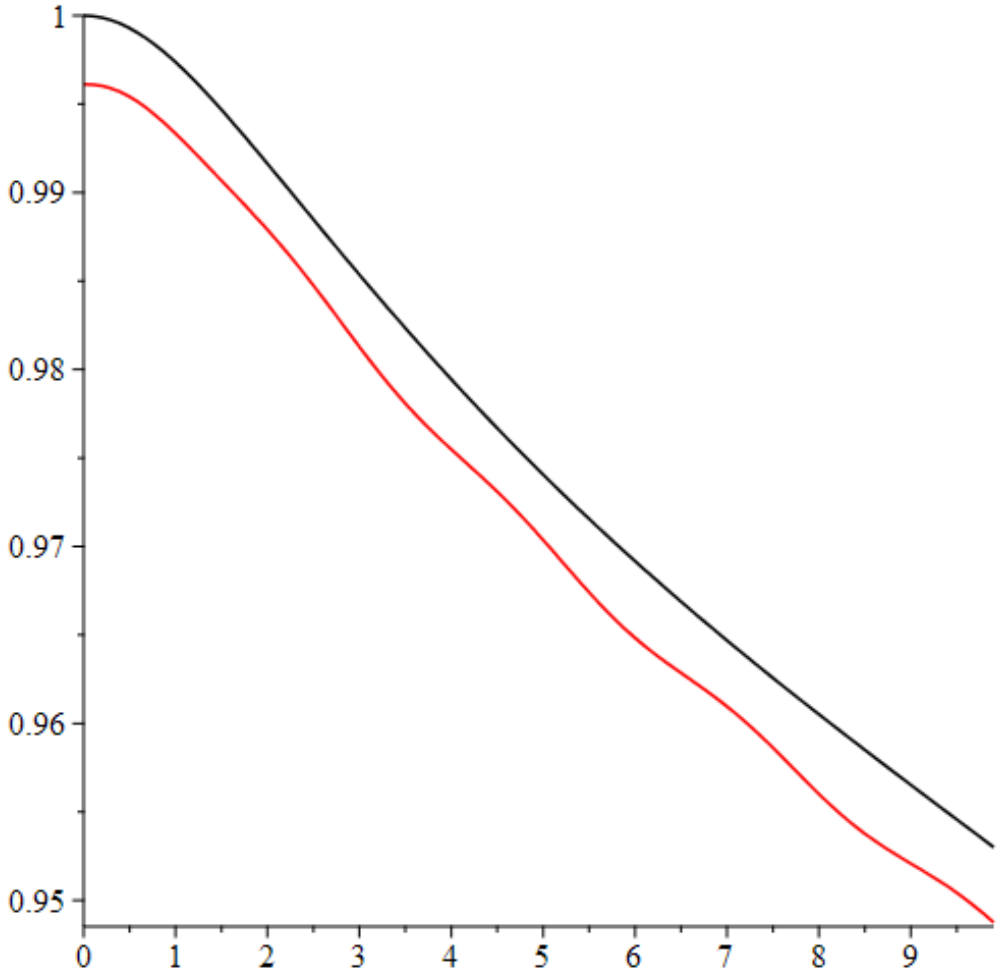

Figure 8.3: Numerical plot of the real parts of the Fourier distribution calculated using the welding method (black) associated to a Gauss-Lorentz test function) and (8.18) calculated from the moments method.

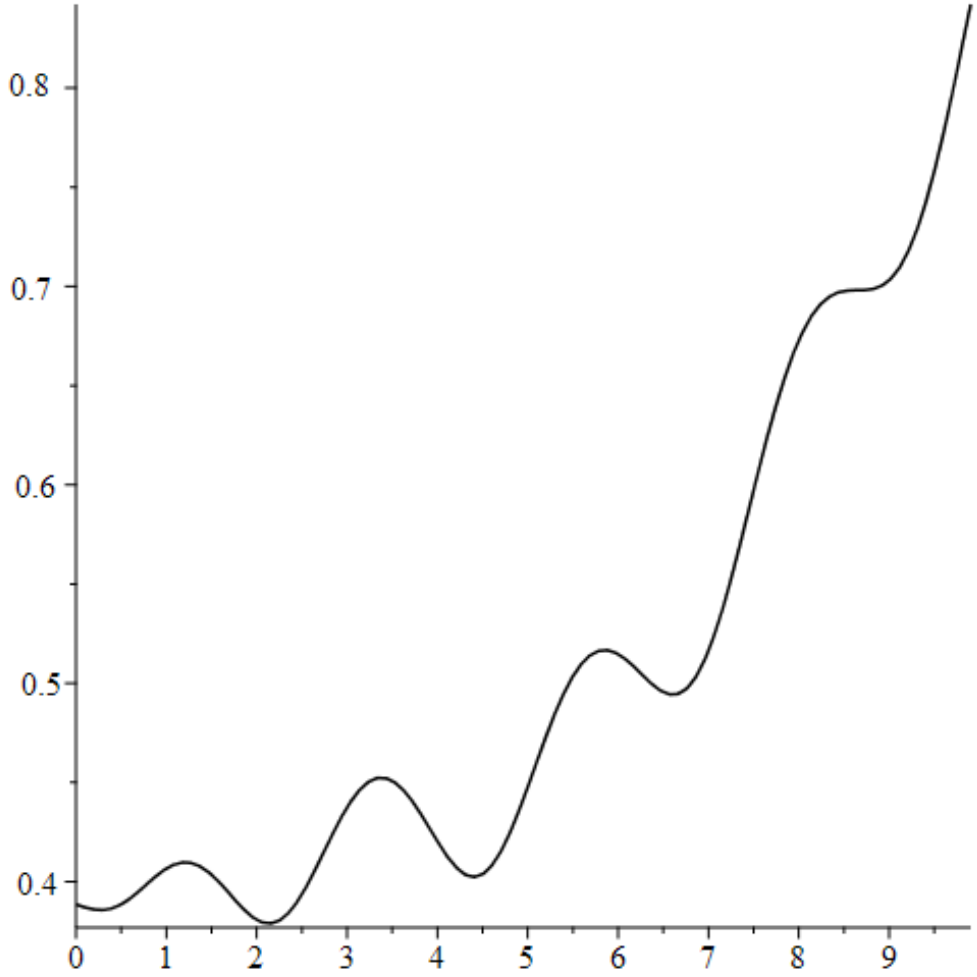

Figure 8.4: Plot of the percentage difference of the points within Fig. 8.3.

probability asymptotics when compared to the characteristic function calculated by the welding method. In the lower and higher order cases we can see that the moments method in the Fourier domain does get close to the calculation generated by the moment method. This is impressive considering the fact that we have to perform a partially analytic and partially numeric Fourier transform of the piecewise moment probability function (8.1) which itself is based on asymptotic results.

— 9 —

Conclusions

This project has been concerned with the probability distributions exhibited from the choice of smearing function in a (1+1)d conformal quantum field theory. The project began with an exploratory numerical study into the method of conformal welding to identify and explore these probability distributions. We have implemented the method proposed in [12] that uses conformal welding to generate the probability distribution for $T(f)$ in the vacuum.

This method was implemented numerically and found to be able to produce the probability distributions associated with the test function used. The code was verified by achieving high levels of agreement to the known analytic results provided. It was also found that travelling to large Fourier transform parameters incurred large numerical errors. These errors were mitigated by a myriad of techniques designed specifically to ameliorate the issues incurred during large Fourier transform parameter investigations and would be of use to anyone interested in the calculation of these distributions.

It was found that Fourier inversion of the numerically calculated welding data behaved poorly unless one was able to calculate to a large enough value in the transform parameter. Due to this issue the welding method with this implementation is better used to compare different probability distributions to observe how the Fourier transform of the probability distribution is af-

fected by certain changes to the test functions used. This was demonstrated in the plateau case.

If one were able to better control these calculation issues presented by the numerical implementation of the welding method then it would become a very powerful method of discovering how the effects of different test function behaviours will affect the probability distribution of the associated observable.

The methods of calculation of the Schwarzian derivative were novel and of use to anyone intending to calculate the Schwarzian derivative in a welding context. As discussed, the third derivative in a numerical environment presents inevitably large errors compared to lower order derivatives but using the analytic methods presented these errors were well controlled allowing for far better and smoother data calculated from this step.

The plateau results were a success of the implemented welding method and these confirmed that there is a dependence on the probability distribution associated to the plateau length and switch on times of the function averaging the stress-energy tensor. This dependence was unreachable using analytic techniques and highlights the benefit of a stable numerical method.

It would also be interesting to apply the welding method to the context of moving mirrors as outlined in [13, 16] to understand the impact this would have on the probability distribution as well as studying the impact of accelerated trajectories.

Prior to this project, all known examples of probability distributions with nonnegative sampling functions gave shifted Gamma distributions. We have shown that a the Gauss-Lorentz test function breaks this rule by producing a probability distribution which is not purely governed by a shifted Gamma distribution.

The Gauss-Lorentz test function exhibits instead a probability distribution which transfers from one distribution in the relevant limit and then tends towards the shifted Gamma distribution associated with the other and deviates non-trivially from each shifted Gamma distribution in between. This behaviour of the constituent parts of the constructed test function still affecting the probability distribution is interesting. Perhaps taking a combination of three test functions could be analysed to understand better this effect. The challenge of this would be seeing the impacts of all 3. In the case of the Gauss-Lorentz test function it was only through the asymptotics of the distribution were we able to notice the effects of the original test functions. Perhaps the inclusion of a third would either dominate in one of the two ends or be invisible in terms of the asymptotic analysis.

The method of moments demonstrated in [12, 2] gives a clear analytic method in which one begins with a test function and then calculates in a tractable way the second moment which is then used to calculate the probability distribution. This summary does not demonstrate the difficulty one can find when trying to analytically solve the flow equation (3.22). This vital step prevents this method from being useable in a completely general case. Even in the case of Gauss-Lorentz, where individually results are known for the Gaussian and Lorentzian cases, a non-trivial formula was found to solve the flow equation.

Despite this key issue with the method of moments. This analysis has proved that if one is able to solve (3.22) then information can be found regarding the probability distribution, even if just asymptotically as in the case of Gauss-Lorentz.

References

[1] I. Affleck. "Boundary condition changing operators in conformal field theory and condensed matter physics". In: vol. 58. Advanced quantum field theory (La Londe les Maures, 1996). 1997, pp. 35–41.

[2] M. C. Anthony and C. J. Fewster. "Explicit examples of probability distributions for the energy density in two-dimensional conformal field theory". In: *Phys. Rev. D* 101.2 (2020), pp. 025010, 6. ISSN: 2470-0010.

[3] P. Billingsley. *Probability and measure*. Wiley Series in Probability and Statistics. Anniversary edition [of MR1324786], With a foreword by Steve Lalley and a brief biography of Billingsley by Steve Koppes. John Wiley & Sons, Inc., Hoboken, NJ, 2012, pp. xviii+624. ISBN: 978-1-118-12237-2.

[4] R. Blumenhagen and E. Plauschinn. *Introduction to conformal field theory*. Vol. 779. Lecture Notes in Physics. With applications to string theory. Springer, Dordrecht, 2009, pp. xii+265. ISBN: 978-3-642-00449-0.

[5] J. Cardy. "Conformal field theory and statistical mechanics". In: *Exact methods in low-dimensional statistical physics and quantum computing*. Oxford Univ. Press, Oxford, 2010, pp. 65–98.

[6] C. M. Caves. "Quantum-mechanical noise in an interferometer". In: *Phys. Rev. D* 23 (8 1981), pp. 1693–1708.

[7] D. N. Coumbe. *A note on conformal symmetry*. 2018.

[8] P. Di Francesco, P. Mathieu, and D. Sénéchal. *Conformal field theory*. Graduate Texts in Contemporary Physics. Springer-Verlag, New York, 1997, pp. xxii+890. ISBN: 0-387-94785-X.

[9] H. Epstein, V. Glaser, and A. Jaffe. "Nonpositivity of the energy density in quantized field theories". In: *Nuovo Cimento (10)* 36 (1965), pp. 1016–1022. ISSN: 0029-6341.

[10] C. J. Fewster. "Energy inequalities in quantum field theory". In: *XIVth International Congress on Mathematical Physics*. World Sci. Publ., Hackensack, NJ, 2005, pp. 559–568.

[11] C. J. Fewster, L. H. Ford, and T. A. Roman. "Probability distributions of smeared quantum stress tensors". In: *Physical Review D* 81.12 (2010). ISSN: 1550-2368.

[12] C. J. Fewster and S. Hollands. "Probability distributions for the stress tensor in conformal field theories". In: *Lett. Math. Phys.* 109.4 (2019), pp. 747–780. ISSN: 0377-9017.

[13] C. J. Fewster and S. Hollands. "Quantum energy inequalities in two-dimensional conformal field theory". In: *Rev. Math. Phys.* 17.5 (2005), pp. 577–612. ISSN: 0129-055X.

[14] L. H. Ford and C.-H. Wu. "Quantum stress tensor fluctuations and their physical effects". In: *Recent developments in gravitation and cosmology*. Vol. 977. AIP Conf. Proc. Amer. Inst. Phys., Melville, NY, 2008, pp. 145–159.

[15] E. S. Fradkin and M. Y. Pal chik. "Exactly solvable models of conformal-invariant quantum field theory in D-dimensional space". In: *J. Geom. Phys.* 5.4 (1988), 601–629 (1989). ISSN: 0393-0440.

[16] S. A. Fulling and P. C. W. Davies. "Radiation from a moving mirror in two dimensional space-time: conformal anomaly". In: *Proc. Roy. Soc. London Ser. A* 348.1654 (1976), pp. 393–414. ISSN: 0962-8444.

[17] P. Furlan, G. M. Sotkov, and I. T. Todorov. "Two-dimensional conformal quantum field theory". In: *Riv. Nuovo Cimento (3)* 12.6 (1989), pp. 1–202. ISSN: 0393-697X.

[18] M. R. Gaberdiel and A. Recknagel. "Conformal boundary states for free bosons and fermions". In: *J. High Energy Phys.* 11 (2001), Paper 16, 31. ISSN: 1126-6708.

[19] K. Gawędzki and K. K. Kozł owski. "Full counting statistics of energy transfers in inhomogeneous nonequilibrium states of $(1+1)D$ CFT". In: *Comm. Math. Phys.* 377.2 (2020), pp. 1227–1309. ISSN: 0010-3616.

[20] P. Ginsparg. "Applied conformal field theory". In: *Champs, cordes et phénomènes critiques (Les Houches, 1988)*. North-Holland, Amsterdam, 1990, pp. 1–168.

[21] E. Grong, P. Gumenyuk, and A. Vasil ev. "Matching univalent functions and conformal welding". In: *Ann. Acad. Sci. Fenn. Math.* 34.1 (2009), pp. 303–314. ISSN: 1239-629X.

[22] B. C. Hall. *Quantum theory for mathematicians*. Vol. 267. Graduate Texts in Mathematics. Springer, New York, 2013, pp. xvi+554. ISBN: 978-1-4614-7115-8; 978-1-4614-7116-5.

[23] S. W. Hawking and G. F. R. Ellis. *The large scale structure of space-time*. Cambridge Monographs on Mathematical Physics, No. 1. Cambridge University Press, London-New York, 1973, pp. xi+391.

[24] L. H. Howell. "Numerical conformal mapping of circular arc polygons". In: *J. Comput. Appl. Math.* 46.1-2 (1993). Computational complex analysis, pp. 7–28. ISSN: 0377-0427.

[25] B. L. Hu and E. Verdaguer. "Stochastic Gravity: Theory and Applications". In: *Living Reviews in Relativity* 7.1 (2004).

[26] T. Itoh. "Discretization of the Schwarzian derivative". In: *AIP Conference Proceedings* 1776.1 (2016), p. 090025. eprint: `https://aip.scitation.org/doi/pdf/10.1063/1.4965389`.

[27] C.-I. Kuo and L. H. Ford. "Semiclassical gravity theory and quantum fluctuations". In: *Phys. Rev. D* 47 (10 1993), pp. 4510–4519.

[28] A. Kuznetsov. "On the convergence of the Gaver-Stehfest algorithm". In: *SIAM J. Numer. Anal.* 51.6 (2013), pp. 2984–2998. ISSN: 0036-1429.

[29] F. S. N. Lobo, ed. *Wormholes, warp drives and energy conditions*. Vol. 189. Fundamental Theories of Physics. Springer, Cham, 2017, pp. xiv+303. ISBN: 978-3-319-55181-4; 978-3-319-55182-1.

[30] G. Mack. "Introduction to conformal invariant quantum field theory in two and more dimensions". In: *Nonperturbative quantum field theory (Cargèse, 1987)*. Vol. 185. NATO Adv. Sci. Inst. Ser. B: Phys. Plenum, New York, 1988, pp. 353–383.

[31] D. Mumford and E. Sharon. "2D-Shape Analysis Using Conformal Mapping". In: *International Journal of Computer Vision* 70 (Jan. 2006), pp. 55–75.

[32] W. Nahm. "Quantum field theories in one and two dimensions". In: *Duke Math. J.* 54.2 (1987), pp. 579–613. ISSN: 0012-7094.

[33] Z. Nehari. *Conformal mapping*. Reprinting of the 1952 edition. Dover Publications, Inc., New York, 1975, pp. vii+396.

[34] V. Ovsienko and S. Tabachnikov. "What is ... the Schwarzian derivative?" In: *Notices Amer. Math. Soc.* 56.1 (2009), pp. 34–36. ISSN: 0002-9920.

[35] J. Polchinski. *String theory. Vol. I*. Cambridge Monographs on Mathematical Physics. An introduction to the bosonic string, Reprint of the 2003 edition. Cambridge University Press, Cambridge, 2005, pp. xx+402. ISBN: 0-521-63303-6; 978-0-521-67227-6; 0-521-67227-9.

[36] J. D. Qualls. "Lectures on Conformal Field Theory". In: *arXiv e-prints*, arXiv:1511.04074 (2015), arXiv:1511.04074. arXiv: 1511.04074 [hep-th].

[37] M. N. O. Sadiku and C. N. Obiozor. "A Simple Introduction to the Method of Lines". In: *The International Journal of Electrical Engineering & Education* 37.3 (2000), pp. 282–296. eprint: https://doi.org/10.7227/IJEEE.37.3.8.

[38] M. Schottenloher. *A mathematical introduction to conformal field theory*. Second. Vol. 759. Lecture Notes in Physics. Springer-Verlag, Berlin, 2008, pp. xvi+249. ISBN: 978-3-540-68625-5.

[39] C. Schweigert, J. Fuchs, and J. Walcher. "Conformal Field Theory, Boundary Conditions and Applications to String Theory". In: *Non-Perturbative QFT Methods and Their Applications*. World Scientific, 2001.

[40] T. P. Singh and T. Padmanabhan. "Notes on semiclassical gravity". In: *Ann. Physics* 196.2 (1989), pp. 296–344. ISSN: 0003-4916.

[41] R. F. Streater and A. S. Wightman. *PCT, spin and statistics, and all that*. Princeton Landmarks in Physics. Corrected third printing of the 1978 edition. Princeton University Press, Princeton, NJ, 2000, pp. x+207. ISBN: 0-691-07062-8.

[42] R. M. Wald. *Quantum field theory in curved spacetime and black hole thermodynamics*. Chicago Lectures in Physics. University of Chicago Press, Chicago, IL, 1994, pp. xiv+205. ISBN: 0-226-87025-1; 0-226-87027-8.